8-2022

Computational Characterization of Nonwoven Fibrous Materials: Transport and Wetting Properties

Fang Wang
fwang8@clemson.edu

Recommended Citation

Wang, Fang, "Computational Characterization of Nonwoven Fibrous Materials: Transport and Wetting Properties" (2022). *All Dissertations*. 3078.
https://tigerprints.clemson.edu/all_dissertations/3078

COMPUTATIONAL CHARACTERIZATION OF NONWOVEN FIBROUS MATERIALS: TRANSPORT AND WETTING PROPERTIES

A Dissertation
Presented to
the Graduate School of
Clemson University

In Partial Fulfillment
of the Requirements for the Degree
Doctor of Philosophy
Materials Science and Engineering

---

by
Fang Wang
August 2022

Accepted by:
Dr. Konstantin G. Kornev, Committee Chair
Dr. Olga Kuksenok
Dr. Philip J. Brown
Dr. Igor Luzinov

ABSTRACT

Nonwoven fibrous materials represent a platform of flexible material substrates. Nonwovens are widely used in the production of napkins, paper, filters, wound covers and face masks. In addition, for many applications, nonwoven materials interact with fluids. For example, in filtration applications, nonwoven materials are used to clean fluids containing solid particles or emulsified droplets. The filtration performance is affected not only by the geometrical arrangement of fibers in non-woven materials but also wettability of fibers. Understanding the transport properties of nonwoven materials and interactions between the dispersed droplets and solid substrate is crucial for the design and optimization of filter media. The present work is focused on: (1) obtaining pore space information from 3D structure in nonwoven media and 2) predicting the liquid transport properties in fibrous materials, including permeability and tortuosity (3) investigating droplet morphology on fibers.

Chapters 1-3 provide the basis of fiber-liquid interactions and introduce the lattice Boltzmann method (LBM). Chapter 4 deals with characterization of microstructures generated from 3D reconstructed plywood and random oriented fibrous media. An algorithm based on watershed segmentation is utilized to extract pore network information including: pore diameter, throat diameter and connectivity. The effect of fiber overlapping arrangements, fiber radius and porosity on the pore space morphology was explored by statistical pore-network analysis. A thorough analysis of the correlation between effective geometrical properties and mean pore size, demonstrated that randomness on microscopic level can have a significant effect on the macroscopic properties of the fibrous media.

In Chapter 5, simulations on pore-scale single phase fluid flow through fibrous media using the lattice Boltzmann method were performed. From the simulated flow field, permeability and tortuosity of nonwoven fibrous materials can be evaluated over a wide range of porosity $0.1 < \phi < 0.9$. The validity of Darcy's law which describes the flow behavior through a porous medium was confirmed in the studied porosity regime. The simulation results were used to test the accuracy of semi-empirical scaling relations, that enabled predictions in trans-plane permeability and tortuosity based on porosity and specific surface area.

Chapter 6 deals with the wetting and capillarity effects of droplets deposited on a single fiber. A multicomponent pseudopotential lattice Boltzmann model was applied to study the interface dynamics of droplets and wetting/dewetting behavior. By adopting different initial droplet configurations, we studied the stability of barrel-shaped and clam-shell droplets on a single fiber for contact angles ranging from 10° to 68°. The simulated barrel drop profile was validated with experimental results. The morphology diagram established from simulations showed that both barrel and clam-shell configurations are stable in coexistence.

Dr. Ulf Schiller introduced me to the LBM, and guided my research described in Chapter 3-5. These chapters are based on publications [1, 2, 3], but significantly modified to include additional materials that has never been published. Chapter 6 has been developed to explain recent experimental results obtained in Dr. Kornev's group. The developed simulation protocol revealed new physics related to the classical problem of fiber-drop interactions and a new diagram of morphological transitions of droplets on fibers was determined. The numerical simulations and data analysis were carried out on Palmetto high-performance computing (HPC) cluster.

ACKNOWLEDGEMENTS

First and foremost, I would like to express my deepest gratitude and special appreciation to my advisor Prof. Konstantin Kornev. It would not have been possible to write this dissertation without the help and support from him. I feel extremely lucky to be able to join his group and finish my dissertation with his guidance. His unsurpassed knowledge of surface science and complex fluid flow has guided me to explore this fundamental field, and encouraged me to continue exploring the potential of computational fluid dynamics. His excellent original ideas and precise research manner has inspired me to grow as an independent researcher. I could not be more grateful to him for showing faith in me.

I would also like to thank Dr. Ulf Schiller for introducing me to lattice Boltzmann method. Clemson University's Palmetto cluster is acknowledged for generous allotment of compute time and memory needs. My sincere appreciation also goes to my committee members, Dr. Olga Kuksenok, Dr. Philip J. Brown and Dr. Igor Luzinov. They have shown me their kindly help, encouragement, valuable comments and I feel honored to have them on my dissertation committee.

I would like to acknowledge Suman Kumari and Yueming Sun for the collaboration and help with the data analysis. I would also like to take this opportunity to thank my group members and friends for their help with my research and friendship. Last but not least, I deeply thank my parents for their unconditional love.

TABLE OF CONTENTS

CHAPTER

List of Figures

List of Tables

CHAPTER 1

INTRODUCTION

1.1 Background

Due to the significance of predicting the macroscopic transport properties of porous media in nature and technical applications, many attempts have been devoted to characterize the porous materials in this respect. For example, in fuel cell engineering, a considerable research has been conducted to study the permeation of gas phases and produced liquid water transport in porous gas diffusion layers(GDL), leading to the critical questions about water transport mechanism and measurement of relative permeabilities, which play an important role on maintaining the high performance of fuel cells [4, 5, 6]. For liquid filters, separation of finely dispersed water droplet in diesel fuel is an important step to avoid corrosion of engine components and suppress microbial growth. The various structure parameters, such as filter thickness, porosity, fiber radius, fiber orientation, and pore size have been shown to affect the capture mechanism of water droplets on the fibers and the coalescence of drops .

In addition to the geometrical features of fiber webs, the surface wettability of fibers is also an important parameter that determines the overall separation efficiency of filters. The droplet capture mechanism strongly depends on wettability of the fiber materials. Formation of liquid film on the front/rear face of fibrous filters due to accumulated droplets may cause filter clogging and notable rise of pressure drop. The background information about pore structure, transport properties and wetting phenomena are discussed in the flowing subsections.

1.1.1 Characteristics of porous materials and pore network

Porous materials are defined as a type of two-phase ordered/disordered materials, which are occupied by solid matrix and void space. For example, one type of natural inorganic materials, such as soil, rock, sediments and cemented sandstone, are highly heterogeneous and made up of particle aggregates. The other type of manufactured porous media, such as paper, organic tissue, and filters, are homogeneous and made up of fibers[7]. In these materials, the pores are interconnected and hence allow a fluid to flow from one side of the sample to the other side. The unique feature of these porous materials is the three-dimensional pore network which can be modeled by a bundle of capillary tubes with varied shape, diameter and orientation. Despite the centuries-long effort in characterizing the pore structure and transport processes in porous materials using both experiments and modeling approach, it remains a complex task to include the features of 3D structures at micro-level description in these attempts. The fibrous materials are usually highly porous and the pores are continuous, leading to the challenge in separating pores from throats in the network.

At the macroscopic level, the most import parameter of porous media is the porosity ϕ, defined as the ratio of volume of voids of a sample to the volume of a sample, $\phi = V_{\text{void}}/V_{\text{sample}}$. Porosity can be easily evaluated by using the incremental weight method when the sample is weighted before and after saturation with a wetting fluid. Characterization of the pore structure and surface area is a more difficult task. Owing to the rapid development of imaging techniques, image-based network models are gaining its popularity. The 3D representation of a porous material can be built-up from a series of 2D cross-sectional micro-CT images. Once the 3D reconstructed geometry is obtained, the image analysis techniques are employed to acquire the real pore space topology which contains the major information of network elements including: pore shape, pore and throat diameter, pore size distribution, connectivity and specific surface area. These parameters are affected by the solid structure properties, such as granular particle size, particle size distribution, fiber shape, fiber diameter and orientation.

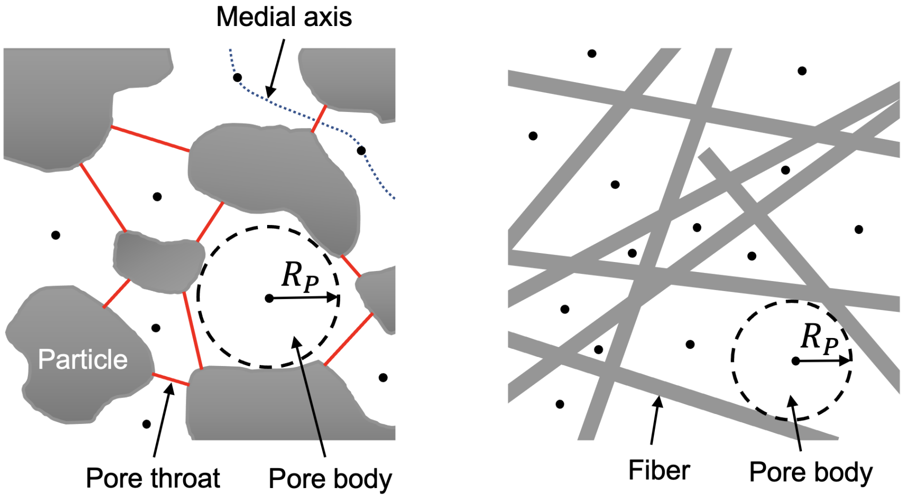

Figure 1.1: 2D schematic illustration of a pore body, pore-throat, pore radius R_p in granular (left) and fibrous (right) porous media.

To extract the networks from pore space images, the standard process includes: 1) removing noise and ring artifacts during the acquisition by filtering, 2) image segmentation based on thresholding algorithm, 3) separate the continuous pore space into discrete network elements which represent pore-throats region. In the fibrous medium, the flow is assumed perpendicular to the page. Observe that the pore throats are not defined in this core. Therefore, it is clear that the pore network is non-unique and depends on the features of porous media and investigator subjectivity. The pore bodies are the larger voids in the porous media and connected by narrow pathways called throats [8]. Connectivity is defined as coordinate number, which is the number of neighboring pores adjacent to one single pore. Fig. 1.1 is a 2D schematic illustration of pores and throats identified in granular and fibrous porous media. There are several approaches that have been employed to determine the size of pores and throats. One is based on erosion and dilation operation that can be used to find the central skeleton or medial axis as shown in Fig. 1.1 which connects the center of pores and throats [8, 9]. The branching points of the medial axis are identified as centers of pore bodies. Another approach is based on maximal ball algorithm [10]. The balls centered on void voxels are grown until they are inscribed with the solid surface and pore diameter is determined by the maximal ball diameter.

1.1.2 Transport properties of porous media

With the advancement of computing power, modeling of fluid flow through porous media at pore-scale level becomes possible. This approach allows us to capture the inherent pore heterogeneity and density, pressure and velocity of fluid inside pores. However, to transform the microscopic modeling with limited domain size into a macroscopic description, one needs to select the appropriate size of representative elementary volume (REV), such that the porous medium domain can be regarded as a continuum and the average over REV can represent the properties of a macroscopic material.

The fundamental equation governing the motion of fluid in a porous medium is described by the mass balance equation and momentum balance equation. For the incompressible, Newtonian fluid , the governing equations can be written as:

$$\nabla \cdot \mathbf{u} = 0, \tag{1.1a}$$

$$\rho(\frac{\partial \mathbf{u}}{\partial t} + \mathbf{u} \cdot \nabla \mathbf{u}) = -\nabla p + \eta \nabla^2 \mathbf{u} + \rho \mathbf{g}, \tag{1.1b}$$

where $\mathbf{u}$ is velocity vector, ρ the fluid density, η the dynamic viscosity, $\mathbf{g}$ the acceleration due to gravity, and t is time. When inertial forces in a conduit of characteristic side L, are much weaker than the viscous forces, so that the Reynolds number is small $\mathrm{Re} = \frac{\rho u L}{\mu} \ll 1$, the inertial term can be neglected and the Navier-Stokes equation (1.1b) reduces to the

Stokes equation:

$$-\nabla p + \eta \nabla^2 \mathbf{u} + \rho \mathbf{g} = \mathbf{0}, \tag{1.2}$$

Considering porous material at the scales much greater than the pore size, one can think about it as of a continuum. In such a case, the details of flow through the pores can be ignored and one can talk about average velocity $\vec{u}$. The average flow velocity $\vec{u}$ is related to flux $\vec{q}$ by the porosity ϕ and can be expressed as $\vec{u} = \vec{q}/\phi$. Assuming the viscous resistance force is linear with the velocity, we can introduce Darcy's law as:

$$\mathbf{q} = -\frac{\kappa}{\eta}(\nabla p - \rho \mathbf{g}), \tag{1.3}$$

where κ is permeability, and pressure p is introduced as an average pressure over REV. This constitutive equation governs the single phase fluid flow in a porous medium. Although Darcy's law is phenomenologically derived by Henry Darcy in 1856 [11] from analysis of seepage flow in the vertical sand column experiment, it can be derived from the Stokes equation (1.1a) and (1.2). The permeability κ describes the ability of a porous medium to allow fluid to pass through it and strongly depends on the geometrical parameters of pore space in solid matrix.

The pore space in a porous medium can be regarded as a bundle of capillary tubes. Consider the Hagen-Poiseuille flow that describes fully developed laminar flow through a long cylindrical tube of constant cross section. The mean velocity U of such a flow is:

$$U = \frac{D^2}{32\eta} \cdot \frac{\Delta p}{L}, \tag{1.4}$$

where D and L are the diameter and length of capillary tube. Comparing Eq. (1.4) with

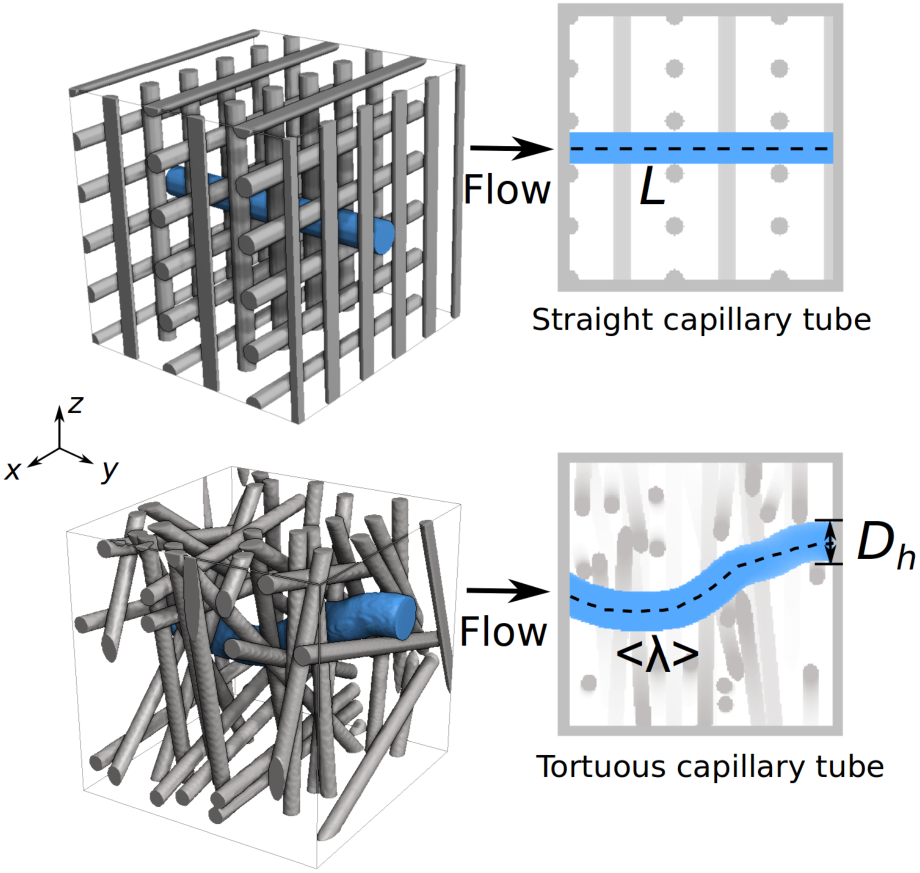

Figure 1.2: Capillary tubes in woven (top) and non-woven (bottom) fibrous media. D_h is the hydraulic diameter and $\langle\lambda\rangle$ is the average length of flow path.

(1.3) and taking into account $g = 0$, $\nabla p = \Delta p/L$, we find

$$\kappa = \phi\frac{D^2}{32}. \tag{1.5}$$

Fig. 1.2 illustrates the possible orientation of capillary tube in woven and non-woven fibrous materials. In reality, the flow path is tortuous due to the random orientation of fibers, and the stream tube cross section can be non-circular. Therefore, the concept of hydraulic radius R_h and tortuosity τ is introduced [12]. Hydraulic radius R_h is introduced through specific surface area S and porosity as:

$$S = \frac{A_{\mathrm{p}}}{V_{\mathrm{solid}}}, \tag{1.6}$$

$$R_h = \frac{V_p}{A_p} = \frac{\phi}{S(1-\phi)}, \tag{1.7}$$

where the specific surface area S is the ratio of total surface area of pores A_p and volume of solid matrix. Substituting the hydraulic radius (1.7) into Eq. (1.5), the semi-empirical Kozeny-Carman equation which predicts the permeability of porous materials using the specific surface area and porosity can be obtained [13, 14, 15],

$$\kappa = \frac{\phi^3}{C_k S^2 (1-\phi)^2}, \tag{1.8}$$

For the Hagen-Poiseuille model, Eq. (1.8) is applied with C_k=8. In the general case, the constant C_k is called the Kozeny constant. Tortuosity $\tau = \langle\lambda\rangle/L$ measures the length of average flow path $\langle\lambda\rangle$ relative to the distance L traveled in the direction of the pressure gradient. Carman pointed out that the average flow velocity U through the tortuous path should be corrected by $\frac{U}{\phi} \cdot \frac{\langle\lambda\rangle}{L}$ [14, 16]. Therefore, the Kozeny constant C_k is replaced by the Kozeny-Carman coefficient $C_{kc} = C_k\tau^2$. From the above equations, permeability of a porous medium shows a complex dependence on fiber arrangement and pore structure at the micro-scale characterized by specific surface area, porosity, fiber orientation and pore diameter.

1.1.3 Droplet wetting and spreading

The droplet spreading on and wetting of a solid substrate is of primary importance in everyday life. For example, the water absorption and diffusion in the void spaces of hair due to capillary effect, water droplet rolling over the superhydrophobic Lotus leaves, liquid retention in textiles. For explanation of these effects, the interaction at liquid/liquid and liquid/gas interfaces are important. Interfacial tension $\gamma_{\alpha\beta}$ between a pair of substances α and β is defined as the work required to increase their interface by a unit area. Therefore, $\gamma_{\alpha\beta}$ is measured in J/m^2, i.e. it is the energy density.

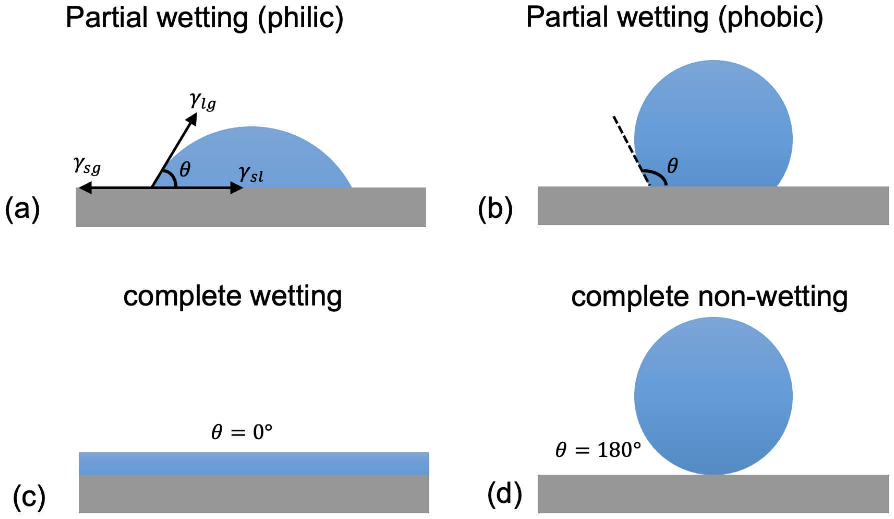

Figure 1.3: Illustration of different contact angles of droplet deposited on a flat surface: a) force balance yields the Young's equation. A contact angle is less than 90° , (b) contact angle is larger than 90° , (c) contact angle is 0°(complete wetting), (d) contact angle is 180°(complete non-wetting).

When two immiscible fluids are in contact with a solid, the equilibrium shape of liquid body is determined by the force density at the line of contact. In Fig. 1.3, we schematically show a drop sitting on a solid substrate. Due to interfacial tension between each two substances, three forces act at the three phase contact line, each being directed along the tangent to the interface between adjacent phases. The magnitude of each force, per unit length of the contact line, equals to the corresponding interfacial tension, γ_{sl}, γ_{sg} and γ_{lg}. The force balance along the contact line:

$$\gamma_{sg} = \gamma_{sl} + \gamma_{lg} \cos\theta, \tag{1.9}$$

defines the equilibrium contact angle θ. Eq. (1.9) is called the Young's equation. If $\gamma_{sg} > \gamma_{sl}$, the contact angles are smaller than 90° and the surface is defined as wettable. For an aqueous system, it is hydrophilic or high surface energy surface. In the opposite situation when $\gamma_{sg} < \gamma_{sl}$, the contact angles are greater than 90° and the surface is defined as non-wettable. For an aqueous system, it is hydrophobic or low surface energy surface. If $(\gamma_{sg} - \gamma_{sl})/\gamma_{lg} > 1$, the liquid will spontaneously spread into a thin film on the solid surface. The spreading coefficient S defined as $S = \gamma_{sg} - (\gamma_{sl} + \gamma_{lg})$ is positive in such a case[17]. Fig.1.3 illustrates four different wetting scenarios: completely wetting, partial wetting and completely non-wetting. For the liquid droplet deposited on curved surface, its equilibrium shape is determined by the force balance and described by the Laplace equation of capillarity:

$$p_c = p_\alpha - p_\beta = \gamma(\frac{1}{R_1} + \frac{1}{R_2}), \tag{1.10}$$

where subscripts α and β denote two immiscible phases, R_1 and R_2 are the two principal radii of curvature of the interface. The above equation relates the equilibrium pressure difference between the two fluids, capillary pressure p_c, to the principal radii of curvature of the interface.

1.2 Motivation for study

Fiber mats are a unique class of porous materials and are widely used in filtration and separation applications. The geometric properties of fibrous media and fiber wettability play a crucial role in designing fibrous filters with optimal performance. With the development of modern imaging techniques, numerous research has been conducted to predict the transport properties of materials using fully resolved 3D geometry at relevant scale. However, the available resolution and image quality often limit the accuracy of the pore space analysis, and random heterogeneities and connectivity information have rarely been accounted for in previous analyses. Therefore, the first part of this thesis is aimed at reducing the gap between experimental characterization methods and statistical analysis of pore network.

The second challenge we are addressing in this thesis is the effect of surface properties of fibrous media on droplet spreading behavior. Although there have been large amount of publications on droplet interaction with solid surface [18, 19, 20, 21, 22, 23, 24, 25], the effect of surface properties and geometrical structure of fibrous membrane on the dynamics of droplet spreading has not been thoroughly studied and needs to be explored in greater details.

Lattice Boltzmann method is a versatile alternative to traditional Computational Fluid Dynamics (CFD) approaches. Owing to its mesoscopic nature and implement of Bounce-back boundary conditions, LBM has the advantage of easy handling of complex geometries and capability of simulating multi-phase flow by using Shan-Chen model without tracking the interface [26]. The single phase flow in porous media has been well studied by using the LBM to verify the validity of the Kozeny-Carman model for the prediction of the permeability of fibrous media [27, 28]. By introducing surface tension and wettability characteristics, the features of multi-phase and multi-component flow can be simulated. Through a quantitative analysis of the shape transitions of liquid droplets on fibers, we hope to introduced a simulation protocol that allows one to study the morphological transition and provide an insight to design fiber materials for filtration and separation of liquids.

CHAPTER 2

LITERATURE REVIEW

2.1 Fibrous network and its engineering applications

As shown in Fig.2.1, fiber membranes has a long history of applications in a wide range of technologies including wastewater decontamination [29, 30], drug release [31], fuel cells [32, 33], medical textiles [34] and tissue engineering [35]. Water pollution are caused by complex contaminants, including heavy metals, suspended particles and organic components. The multifunctional nanofiber network is an efficient candidate to eliminate the above ingredients because it can show filtration, photocatalytic and antibacterial properties simultaneously with proper selection of materials fabrication processes [29]. One the other hand, the separation of water-in-oil emulsion by fibrous filter is a popular method in diesel engine operation [36]. Fibrous porous media stand out as soft porous materials with a large range of possible porosities, high surface-to-volume ratio, and tunable surface functionality.

Nonwoven fibrous membranes fabricated by melt-blowing processes are common materials for air and water filters. Fiber membranes produced by electrospinning [38, 36] have shown great potential for filtration owing to smaller fiber diameters and higher surface-to-volume ratios, promising improved efficiency for filtration [37]. Electrospun fiber membranes can be produced with large porosity beyond 80% and specific surface areas in the range of $10-500$ m^2/g. The interconnected pore space is fully accessible, enabling higher

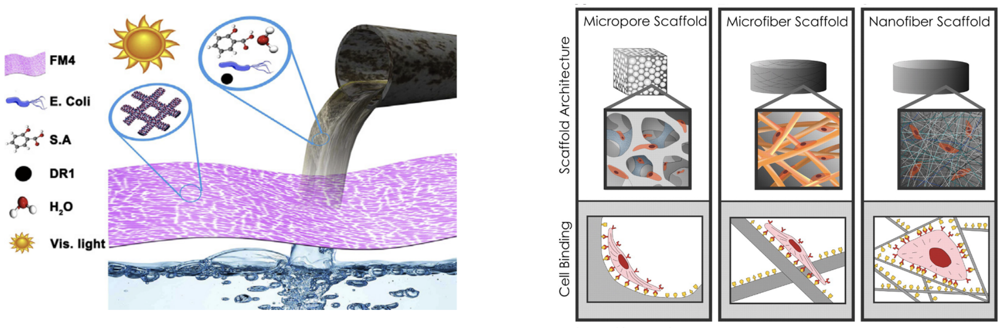

Wastewater treatment *Scaffold fabrication in tissue engineering*

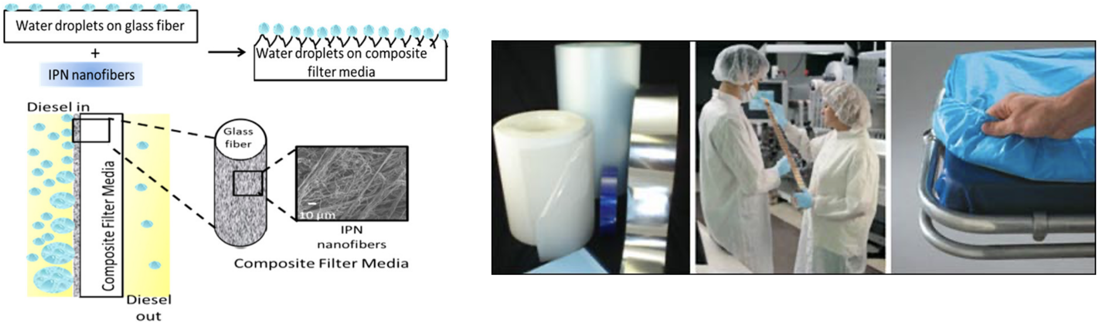

Coalescing filter media *Medical textiles*

Figure 2.1: Applications of fiber membranes in wastewater decontamination, tissue engineering, coalescence filtration of water-in-diesel (reproduced from Ref. [29, 35, 37] with permission), and medical textiles (from https://www.technicaltextile.net /articles/nonwovens-as-medical-textiles-3693).

flow rates while reducing the energy consumption during filtration. In addition, the electrospinning method can be used with advanced fiber materials such as ceramic scintillators to produce functional porous membranes for detection of ionizing radiation in flowing fluids [38].

Ever since the emergence of COVID-19 outbreak and subsequent global spread in 2019, the use of N95 respirators, which is composed of multilayers of polypropylene (PP) nonwoven fabrics, has become the best protective method to limit the spread of virus and protect humans from viral infection. The fiber diameter and pore size in the outer spunbonded PP layer are typically up to $20\mu m$ and $100\mu m$, respectively. While in the middle meltblown layer, the fiber diameter is in the range of 1-$10\mu m$ and the pore size is around $20\mu m$[39]. Prior studies haven been conducted to investigate the droplet transmission through and around a face mask [40], the re-usability of N95 respirator after different decontamination treatments[39, 41, 42, 43, 44], and the performance of home-made mask compared to commercial medical masks[45]. Dbouk et al. performed a fluid dynamics study on the transmission of respiratory droplet around face mask filters using the open-source computational fluid dynamics code OpenFOAM[40]. Their study included three types of interaction mode between droplets and filter surface: stick, splash/rebound and penetrate. The interaction mode as a function of critical droplet diameter and splash kinetic energy depends on the geometrical properties of fibrous filter, e.g.,fibrous porous microstructure, pore diameter, porosity and fiber orientation. Saini et al. investigated the impact of vaporized hydrogen peroxide (VHP) treatment on microscopic face mask integrity and droplet permeability through the filter [44]. The liquid permeation test results showed no significant influence on droplet permeability for N95 masks after multiple cycles VHP treatment. And there is no discernable changes observed for fiber morphological features in terms of fiber width.

Fluid flow and diffusion in fibrous media depend on the geometrical structure of the pore space, which provides unique solutions to filtration and separation applications [46, 47]. Therefore, the hydraulic response of fibrous media to an applied pressure gradient has been extensively studied in the past, going back to the seminal experimental work of Darcy [11].

The pressure-driven fluid flow through a fibrous material is determined by the permeability, a tensor quantity that measures the fluid conductivity of pore network. The permeability depends on the geometrical properties of the pore space, most notably, the pore size and porosity, i.e., the volume fraction of voids in the solid material. It has been a long-lasting challenge to predict the intrinsic permeability of porous media. For example, in proton exchange membrane fuel cells (PEMFC), the gas diffusion layer (GDL) where reactant gas transfer to catalyst layer and the product water is accumulated, is of primary interest to materials engineers. The current density is influenced by the mass transfer rate of reactant and product, making permeability of GDL a critical parameter for the evaluation of performance [48]. In spite of the extensive experimental research, no exact expressions for the permeability are available so far, and predictions of the fluid flow through different porous materials rely on phenomenological expressions such as the Kozeny-Carman formula [13, 14].

In contrast to long-standing research on granular porous media such as soil, rocks[49, 50, 51], and cement [52], the flow through fibrous porous media has only recently been studied more actively [53, 54, 55]. While progress has been made to determine the flow through fiber networks, the specific dependency of the permeability on the geometrical structure of the pore space remains poorly understood [54, 56]. The existing phenomenological expressions for permeability do not take into account the intrinsic disorder of fiber placement and local heterogeneity in real fibrous materials. These may significantly alter the flow characteristics including the tortuosity which measures the relative length of a flow path compared to the straight distance in the direction of the pressure gradient. The complex geometry of the pore space is the result of variations of fiber diameter, fiber orientation, and fiber overlapping during processing. Few attempts have been made to quantify the effect of random irregularities in size, shape, and connectivity of the pores. For consistent performance and quality control of filter materials, it is crucial to gain a better understanding how the random features of the pore space affect permeability of fibrous porous media.

Reconstructed porous geometries from experiments can be used for computational modeling of flow through porous media [56, 57, 58]. The simulations allow to predict permeability and determine the scaling exponents that appear in the empirical permeability expressions [14, 54, 59, 60, 61]. Early efforts based on the work of Fatt [62] employed pore-network models that represent the pore space as a network of idealized pores connected by capillary throats of varying diameter. The fluid flow is described by a discretized Laplace equation using the known permeability for the cylindrical capillaries. For fibrous porous media, however, the high porosity and irregular shape of the pore space make the identification of pores and throats more difficult [56]. The connectivity of the pores is thus ambiguous and limits the applicability of pore-network models to fibrous porous media.

Nowadays, the 3D microstructure resolved simulations of fluid flow in porous media are possible. The microstructure resolved simulations are suited to investigate the flow characteristics in porous media at the pore scale [63]. Roberts et al. [64] used reconstructed geometries of lithium-cobalt-oxide electrodes to perform finite-element simulations of coupled electrochemical-fluid transport in lithium ion batteries. They also performed an analysis of the representative spatial scale of heterogeneities in the sample. Gueven et al. [65] used a voxelized representation of sintered glass beads and performed lattice Boltzmann simulations to determine the permeability of different domains of the sample. The results showed that microstructure resolved simulations can reproduce the local variation in permeability with good accuracy, provided a representative sample size is used.

Numerical simulations relating to fibrous media have considered fluid flow through random arrays of parallel cylinders and regular 3D fiber membranes [66, 67, 68]. However, these idealized models do not include the local variation of pore space features that is present in real fiber membranes. Recently, Koponen et al. [56] have considered experimental samples of foam-deposited and water-deposited pulp sheets and analyzed X-ray tomographic images to determine the local thickness of the pore space. They further performed lattice Boltzmann simulations of fluid flow through the reconstructed porous sheets and determined an expression for the permeability that depends on the thickness distribution. Due to the small number of samples considered within a narrow range of porosity, it remains an open question whether this expression applies to fibrous porous media in general, in particular for denser membranes with overlapping fibers.

2.2 Pore network characteristics

Due to the significant influence of pore structure on final performance of filter, many researches have been performed to study pore structure and measure pore characteristics in nonwoven media[69, 70, 71]. The most common experiment techniques to evaluate the pore include bubble point, extrusion porosimetry and mercury intrusion porosimetry. The main pore characteristics of fibrous media include connectivity, pore diameter, pore size distribution, specific surface area, pore volume and pore shape. Connectivity is defined as coordinate number, which is the number of neighboring pores adjacent to one single pore. And the specific surface area is the ratio of the total surface area of pores and solid volume. Pores in nonwoven media with low porosity can be regarded as a network of many connected capillaries. While capillary network consists of many elements with the same diameters, the pores in fibrous media have irregular diameter. Due to the complexity of pore structure, the diameter of capillary is considered as the pore diameter in almost all available measurement approaches [69, 72]. Pore volume is defined as the voids volume of the porous materials. The measured pore volume varies using different techniques because pore size is not identical in each technique. For high porosity media, pore regions are more packed, overlapped and there are many voids within the structure.

Theoretical approaches are developed by assuming the 3D structure consisting of layers of fibers oriented in certain direction. Different parameters can affect pore structure in a fibrous materials. These parameters include porosity, fiber orientation and fiber diameter. Faure et al. developed a model to predict the pore size distribution based on Poissonian polyhedra model [73]. Fibers are considered as the Poisson line networks and the inter-fiber space consists of irregular polygons. The cumulative frequencies of pore diameter is obtained by inscribing spheres between polygons, which is given by,

$$F(d) = 1 - \left[\frac{1 + \chi(d/2 + R_f)}{1 + \chi R_f} \exp(-\chi d) \right]^{T_g/2R_f}, \tag{2.1}$$

where χ is the specific length, i.e., the total length of fiber lines per unit area, d is the diameter of inscribed circle in one layer of fibers, R_f the fiber radius, and T_g the thickness of a fibrous medium. Lombard et al. [74] derived a similar expression by taking the effective layer thickness to be twice the fiber diameter rather than the bare fiber diameter as in the Faure model. The cumulative frequencies of pore diameters are then given by

$$F(d) = 1 - \left[\left(\frac{\chi^2 d^2}{4} + \chi d + 1 \right) \exp(-\chi d) \right]^{T_g/(4R_f)}. \tag{2.2}$$

Another modification was introduced by Rawal [69] by considering a gamma distribution of the inscribed spheres that takes into account the fiber orientation distribution in the form of a directional parameter K_j. This leads to the cumulative frequency of pore diameters given by

$$F(d) = 1 - \left[\left(\frac{\omega^2 d^2}{2} + \omega d + 1 \right) \exp(-\omega d) \right]^{T_g/(4R_f)}, \tag{2.3}$$

where $\omega = \frac{2(1-\phi)K_j}{\pi R_f}$ is the coverage parameter that represents the dimension and shape of pores.

The image analysis techniques to characterize the pore structure is an important component of porous media research to obtain the structure information from the tomographic images. For example, computed tomography (CT) images provide microscale resolved representations of porous media that can be used to characterize the microscopic structure of the pore space. CT image stacks can be digitized and segmented to create a 3D registration that allows to analyze the distribution of pore and throat sizes and their topology. Gueven et al. [65] have conducted an analysis of XRCT images of sintered glass beads, and Huang et al. [54] have analyzed the local thickness distribution of sintered sheet of metallic fibers. Local thickness of pore space is an important metric of porous media. The crucial step in extracting the pore network from a three-dimensional representation is the identification of pores and throats based on the local thickness of the pore space.

The local thickness at a point $\vec{p}$ is defined as the maximum diameter of a sphere that contains $\vec{p}$ and is completely inside the pore space Ω

$$d(\vec{p}) = \max\{d \,|\, \vec{p} \in S_d(\vec{p}_0),\ S_d(\vec{p}_0) \in \Omega\}, \tag{2.4}$$

where $S_d(\vec{p}_0)$ is a sphere of diameter d centered at the point $\vec{p}_0$. In contrast to the surface-based methods, this definition of local thickness is independent of pore shape and orientation, and can be calculated for each voxel in the binary 3D representation. Algorithms for extracting the pore network from the local distance map are typically based on the maximal ball algorithm introduced by Silin and Patzek [10] and subsequently refined by Blunt et al. [75, 76].

To identify pores and their connectivity, watershed segmentation can be employed to find the basins around local peaks in the distance map [77, 78]. Fig. 2.2 is a 2D illustration of watershed segmentation algorithm. Firstly, the binary image matrix is obtained from the input image where the solid pixel is represented by 0 and the void pixel by 1, as shown in Fig. 2.2 (a). Next, the distance transform operator is applied to replace the void region by their Euclidean distance to the nearest pixel with zero intensity. After the corresponding distance transform matrix is obtained, the local minima in the inverted distance map yield catchment basins and are passed as markers in the watershed function as shown in Fig. 2.2 (c). Finally, the flooding of basins from such markers separates the image into several regions along the watershed lines. Watersheds are the elevated areas that divide the different catchment basins as shown in Fig. 2.2 (d) [79, 80].

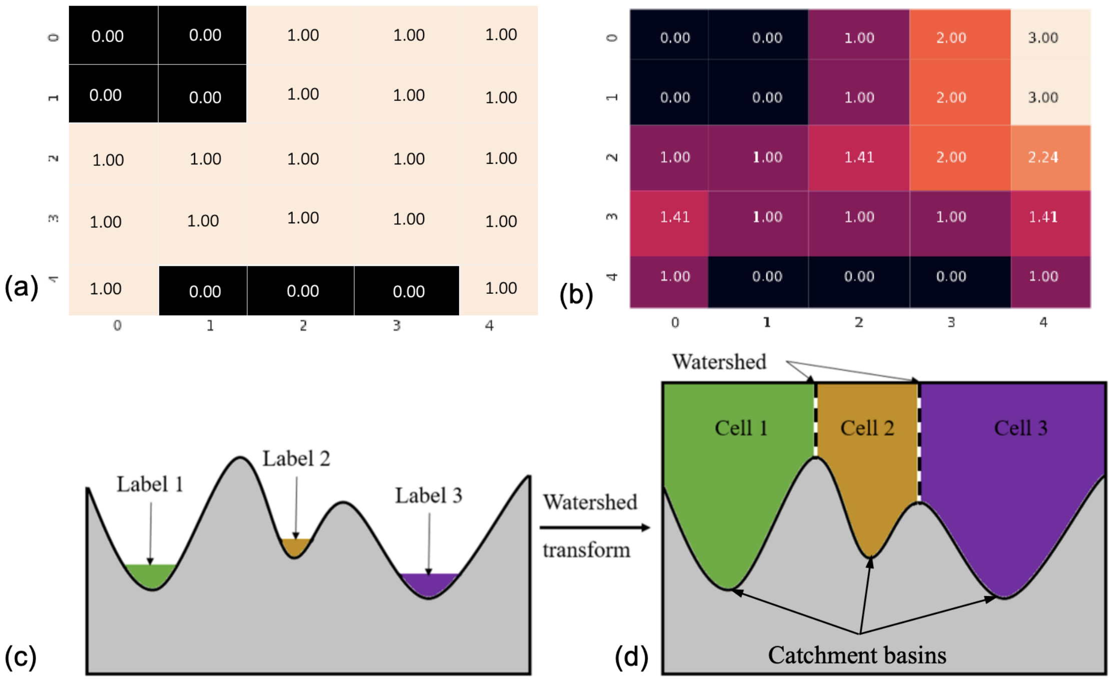

(a)

	0	1	2	3	4
0	0.00	0.00	1.00	1.00	1.00
1	0.00	0.00	1.00	1.00	1.00
2	1.00	1.00	1.00	1.00	1.00
3	1.00	1.00	1.00	1.00	1.00
4	1.00	0.00	0.00	0.00	1.00

(b)

	0	1	2	3	4
0	0.00	0.00	1.00	2.00	3.00
1	0.00	0.00	1.00	2.00	3.00
2	1.00	1.00	1.41	2.00	2.24
3	1.41	1.00	1.00	1.00	1.41
4	1.00	0.00	0.00	0.00	1.00

Figure 2.2: 2D illustration of watershed segmentation algorithm: (a) binary map matrix of input image, (b) distance transform matrix, (c) find catchment basins for the topographical representation of the image, (d) find watershed lines which are the boundaries between the partitions. Adapted from Ref. [80] with permission.

In fibrous porous media, the pore space has a relatively homogeneous distance map with spurious peaks leading to an oversegmented watershed, which makes the identification of pores and throats ambiguous. An improved algorithm for watershed segmentation was proposed by Gostick [81] to generate pore networks for high-porosity media. The algorithm can be summarized in the following steps: 1) Compute the distance transform of the binary image, which is the distance from every voxel to the nearest nonzero-value voxel; 2) Apply a maximum filter with spherical structure of radius R to find where the value in the filtered image are equal to the distance map. The maximum filter replaces each voxel value of the image with the maximum value of its neighbor voxels window (i.e., the value of the brightest voxel). The center of spheres are the local brightness peaks and are passed as makers in maker-based watershed algorithm, then find the basin of distance map.

So the segmented image with each voxel labeled according to the pores it belongs to can be obtained; 3) The information of pores, throats and connectivity can be obtained from the image by finding the region that the pore is adjacent to. The connectivity can be found by scanning the labels of neighboring pores for each individual pore. By dilating the pore regions, the throat size can be determined from the cross section of the overlapping region between dilated pore with its neighbors.

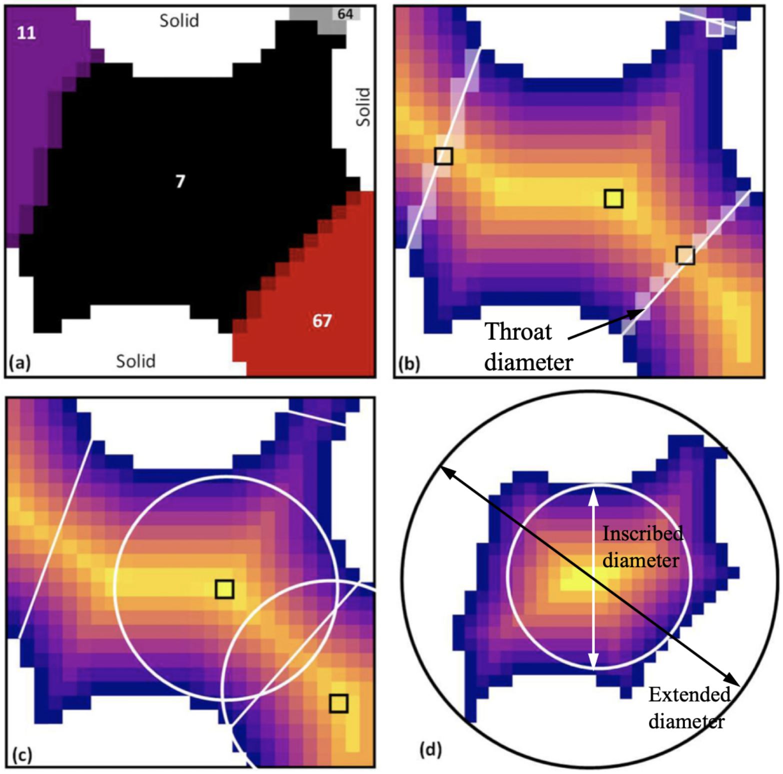

Figure 2.3: 2D illustration of connectivity, pore and throat size. (a) Labeled pore regions. (b) Peaks in the distance map is indicated by black box. (c) Overlapping of neighboring pores using global distance map. (d) Inscribed and extended pore diameter are determined from local distance map and global distance map, respectively. Adapted from Ref. [81] with permission of APS.

Fig. 2.3 illustrates the calculation of pore size, throat size and connectivity for the pore of interest. Pore 7 is adjacent to pores 11, 67, and 64, hence the connectivity is 3. The pore diameter can be defined by the inscribed diameter or the extended diameter.

As shown in Fig. 2.3 (d), the inscribed diameter is the maximum value of local distance map obtained within the pore, where the pore body is confined entirely inside the pore region. While the extended diameter is defined based on the global distance map. Throat diameter is determined from maxima of global distance transform. Gostick eliminates the spurious peaks that lies on the saddles and plateaus of the distance map by identifying and analyzing them individually with an iterative procedure, producing a subnetwork of the oversegmented watershed (SNOW). The algorithm is simple, efficient and can extract reliable networks from both high- and low-porosity fibrous media. The removal of spurious peaks prior to the segmentation will eliminate thin regions and join bisected pores, thus leading to a more representative size distribution of the pore space.

The digital processing of experimental images is non-trivial and requires sophisticated filtering and segmentation techniques. The available resolution and image quality limit the accuracy of pore space analysis. Local heterogeneity and connectivity information have not been accounted for in previous analyses. In addition, the experimental procedures for sample preparation and image acquisition are costly and time consuming, thus typically limiting the statistical analysis to a small number of samples. An ability to generate a lager number of realistic samples is thus desirable to improve the statistical analysis of random pore structures. In particular, it would enable analysis of local heterogeneity and connectivity information that have not been accounted for in previous analyses.

2.3 Wetting of substrate with complex geometries

2.3.1 Curved surface

Wetting and spreading of droplet on curved surface are of key importance in many new or existing industrial applications. A broad body of literature has been published on the wetting phenomena on curved surfaces including cylindrical fibers [82, 83, 84, 85, 86, 87,

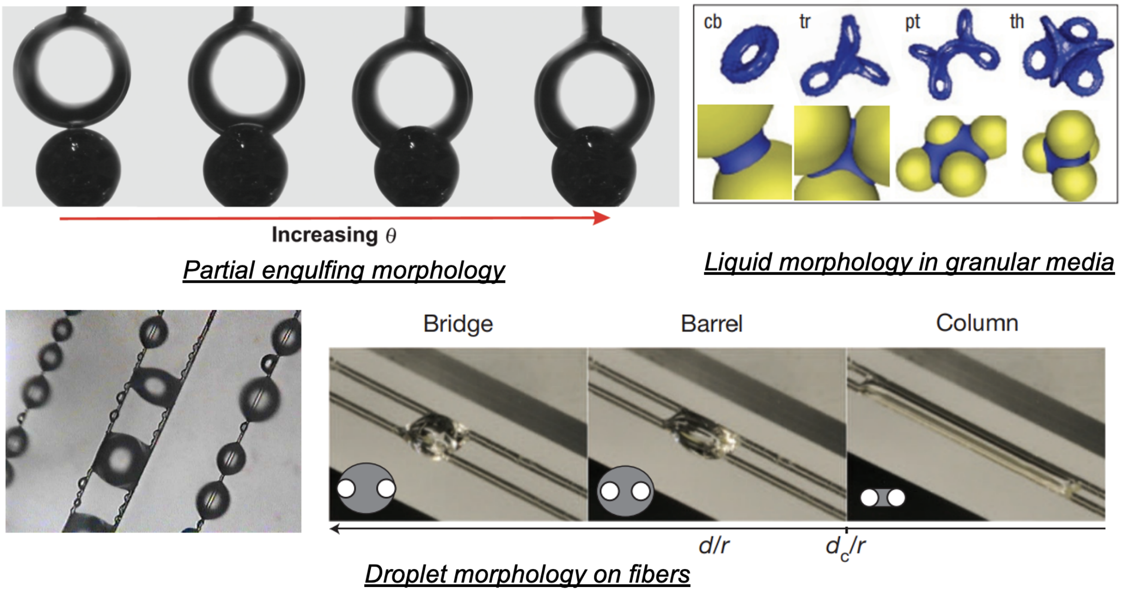

Figure 2.4: Droplet morphologies on spherical particles and fiber rails. Reproduced from Ref. [90, 95, 85, 100] with permission.

88, 89, 90], ribbon-like fibers[91, 92], and spherical beads [93, 94, 95, 96, 97, 90, 98, 99]. The equilibrium configuration of droplet on curved surface is not only affected by the wettability of solid substrate but also its curvature. Example of droplet configuration on spheres and cylindrical fibers are shown in Fig. 2.4.

Droplet wetting of spherical particles is often encountered in industrial process and nature, such as spray coating of nanoparticles[101], fluid catalytic cracking process[99], and raindrops on spherical fruit surface. Eral et al. studied the equilibrium morphology of droplet on a stainless steel particle coated with a dielectric layer [90]. The water contact angle of the particle was controlled by electric field. They calculated the effective interfacial energy difference between “completely engulfing” and “partial engulfing” morphology analytically, and compared the calculation results with experiment data. Their calculation showed that the “partial engulfing” is energetically favorable as the absolute effective interfacial energy of the completely engulfing morphology is greater. Interfacial energies of the two morphology are only identical for vanishing contact angle.

The mixture of certain amount of water with a granular material such as dry sand and soil leads to sufficient increase of stiffness and mechanical stability of the materials, which allows to sculpture sand castles. The underlying principle of this phenomena is the capillary adhesion. The water forms a network of capillary bridges that spans between the grains, which causes strong cohesive force to allow the sand resist deformation due to gravity [93]. The morphology of liquid interface in a granular media is of extraordinary complexity and affected by the liquid volume. Scheel et al. carried out X-ray microtomography experiments to study the liquid distribution in grain packing geometry using spherical glass beads [93]. Their results showed that the mechanical parameters including tensile strength and yield stress are independent of liquid fraction. When the liquid fraction is over a critical value, the neighboring capillary bridges on the same sphere tends to coalesce and form a trimer , which levels off the Laplace pressure.

The wetting morphological transition on fibers controls a broad range of natural and engineering phenomena: film coating of fibers, shape and manipulation of liquid in microfluidic channel and clogging of filters during coalescence filtration. In the textile industry, the wicking of finish liquid into the interfiber space leads to filament cohesion and affect the mechanical properties of yarn surface. For the typical coalescence filter used in water-in-diesel fuel filtration, the increase of pressure drop during steady operation is attributed to the liquid droplets trapped on the surface of a filter [102].

The capillary effect of cylindrical filament remained an active field of research since the pioneering work by Princen [103], who has investigated the equilibrium configuration of small amount of liquid on two horizontal fibers and developed analytical model to investigate the conditions of equilibrium of a long liquid column . Carroll [104] described a method for determining the accurate contact angle on fibers from a barrel drop profile . Due to the challenges of measuring Laplace excess pressure of small volume drop, the fundamental understanding of morphological transition between barrel-shaped drop and clamshell like drop configuration still remains an open question.

With appearance of Brakke's Evolver, a solver for Laplace equation of capillarity based on Finite Element Method for minimization of surface area at fixed volume, this research moved forward. Several attempts to study drop configurations on fiber rails include publications by Wu et al. [105, 88] who used Surface Evolver to calculate the droplet surface energy with varying drop volume. The experimental work by Protiere [86] reports the morphology diagram for deroplet on fiber rails in the parameter space of droplet volume and inter-fiber distance. The recent work by Aziz et al. focuses on the force balance analysis of droplet-bridge on two parallel fibers by both experiment and Surface Evolver simulation [82]. Their results shows an asymmetric shape of liquid bridge when the fiber spacing is small, leading to the droplet morphology transition.

From the previous experiment work, we know that small amount of liquid can spread into long column between parallel fibers when the inter-fiber distance is below a critical value [103, 86]. The drop tends to stay barrel shape to completely wrap up fibers when the drop volume is large. The critical inter-fiber distance is calculated analytically for a broad range of contact angles and validated in the experiments for perfectly wetting. An interesting phenomena observed in the experiments is the hysteresis of transition from the barrel shaped drop to a long column as the fibers are bringing together. The hysteresis loop is affected by the drop volume and contact angle. Using Surface Evolver, Wu et al.[88] showed a third configuration of droplet-bridge that partial wrap the two fibers . However, the droplet bridge configuration is not considered in experiments due to the difficulty in visualizing the difference between micro-structure of barrel-shaped drop and liquid bridge. The comparison between the surface energy of barrel-shaped droplet and droplet bridge determined the more stable morphology for a given drop volume.

The bistability of small liquid drops wetting solid surface has been widely studied for many years. The absolute stability and metastability of asymmetric clam-shell conformation of droplet on single fiber has been studied by McHale et al. [106]. The Surface Evolver results illustrate the absolute stability condition for barrel-shaped drop denoted by the lower surface energy compared to clam-shell drop. The existence of the free energy barrier between unduloid and long column configuration was first put forward by Princen [103]. Experiments conducted by Protiere [86] further confirmed this assumption.

Despite the extensive researches on analysis of equilibrium shapes of droplets, the dynamics of wetting on fibers has not been explored in details. Specifically, the free energy landscape corresponding to morphological transition of liquid bodies has not been studied in these works.

2.3.2 Structured surface

The exploration of morphological transition of droplet on topographically structured surface has attracted great attention: striped surface [107, 108], micropost arrays[109, 110, 111, 112, 113], wedge geometry[114, 115], and triangular grooves [116, 117] were studied due to the potential application in microfluid devices.

In particular, morphological transition of droplets in rectangular domain has been well studied experimentally and numerically. The experimental work by Gau et al. showed that the droplets on hydrophilic stripes undergo a transition to the state with a single bulge when the liquid volume exceeds a critical amount. Ferraro et al. [118] reported the discontinuous morphological transition of water confined to the hydrophilic top of long rectangular posts, where the droplet shape is calculated numerically using Surface Evolver software. They determined the stability boundaries by energy minimization. Sartori et al. [119] constructed an energy landscape of a drop on the rectangular post, and showed that there exists a saddle point between two local minima, corresponding to the smallest work that is needed to transform one morphology to another.

The complex structured surfaces have drawn considerable interest because of their abil-

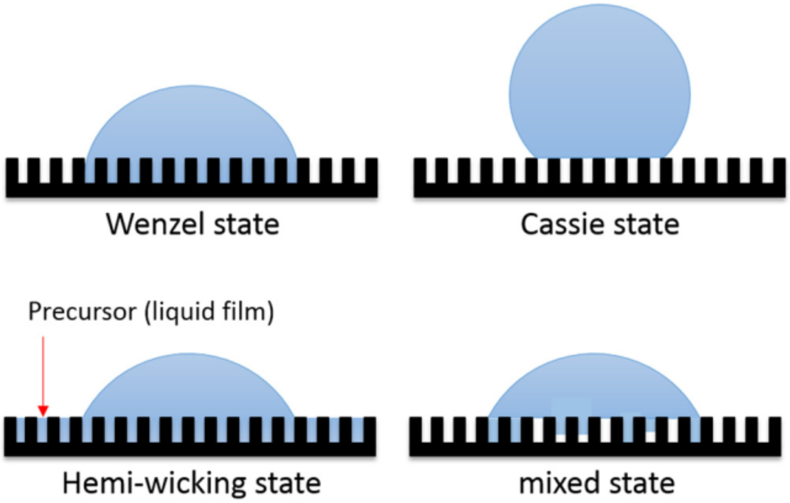

Figure 2.5: Wetting state of droplet on micro-textured surfaces. Reproduced from Ref. [120] with permission of AIP.

ity to achieve more effective and flexible control of wetting properties. The nanoscale surface roughness/texture due to micropillar arrays can be utilized to achieve superhydrophobicity (contact angle greater than 150°) of the solid surface.

The wetting transition between Cassie and Wenzel state is commonly invoked to explain the superhydrophobicity of the textured surface. Cassie-Baxter state (CB) state is known as a wetting state that shows superhydrophobicity by allowing air to be trapped under the droplet and the substrate surface, resulting in much larger contact angle than the smooth surface. The Wenzel state stands for the state where no trapped air remains and the drop directly contacts the substrate surface. Fig. 2.5 shows the various wetting state of a water droplet deposited on a textured surface.

Considerable efforts have been directed towards understanding of the critical condition for the Cassie-Wenzel transition [110, 120, 121, 122, 123, 124]. Yu et al. employed the high spatial resolution synchrotron X-ray radiography to visualize and define the wetting state for a droplet placed on micro-textured surfaces where the surface condition is clearly quantified by roughness ratio, diameter of micro-pillars, and spacing between micro-pillars

[120]. An analytical model with intrinsic contact angle and surface roughness ratio was developed to estimate the wetting state and tested against the experimental results. Zheng et al. [121] numerically simulated the Cassie-Wenzel transition for a periodic structure with irregular pillar cross section, and determined the critical hydraulic pressure that drives the transition. Fang et al. [124] performed a water droplet squeeze test by bringing two plates together to compress a droplet and drive the droplet in Cassie wetting state transit into a full Wenzel state. The force-displacement curve is obtained in the experiments and used to calculate the critical pressure of the Cassie-Wenzel transition. Han et al. [122] demonstrated the possibility of controlling the transition between Cassie state and Wenzel state on a nanostructured surface composed by arrays of carbon nanotubes by utilizing eletrowetting technique. The contact angle decreases as the applied potential increases. At the critical contact angle ($\theta_V \approx 142°$), the Cassie-to-Wenzel transition was observed, corresponding to a much faster response of the contact angle to the applied potential due to the larger capacitance of Wenzel state. Ren et al. [123] used the string method to numerically simulate the Cassie-Wenzel transition on a hydrophobic textured surface consisted of square pillar arrays. From the numerical simulation, the transition can be observed to initiate with infiltration of liquid in a single cavity, and followed by lateral propagation of liquid to the neighboring cavity layer by layer. They calculated the energy barriers and minimum energy path during the wetting transition, which reveals the mechanism of the wetting process.

2.4 Modeling of wetting on solid substrates

Computational modeling is an effective way to determine the static droplet shape on solid substrate. The equilibrium contact angle θ between a liquid interface and a solid substrate is controlled by three surface tensions, solid-liquid γ_{sl}, solid-gas γ_{sg}, and liquid-gas γ_{lg}. The three surface tension and interfacial area determine the overall surface free energy E as:

$$E = \gamma_{lg} A_{lg} + \left(\gamma_{sl} - \gamma_{sg}\right) A_{sl}, \tag{2.5}$$

where A_{lg} and A_{sl} are the liquid-gas and solid-liquid interfacial areas. To determine the equilibrium morphology, the surface energy has to be minimized subject to given constraints such as constant liquid volume and substrate geometry, e.g., fiber surfaces. Explicit solutions are only available for simple situations such as a spherical droplet on a flat surface, an axisymmetric droplet on a fiber [104], or liquid column on a fiber rail [86]. In general, the solutions to the nonlinear problem require numerical procedures.

A host of numerical approaches have been used to describe the wetting phenomena and dynamics of droplet on solid substrates, such as finite element method for Laplace equation with Surface Evolver [106, 88, 82], molecular dynamics [125, 126], phase field method [127], and mesoscopic lattice Boltzmann method [128, 129, 130, 114]. Finite element based method is an discretization approach to find the numerical solution of Young-Laplace equation and solve for the stable liquid configuration by minimization of the surface energy. In a stable configuration, the excess Laplace pressure is constant everywhere across the droplet surface. Such a configuration is metastable if its surface energy is higher than another stable morphology with the same volume. A morphological transition is thus associated with an energy barrier that is needed to move equilibrium droplet from one configuration to the other. Since measuring excess pressure for small liquid volumes is challenging, the connection between the surface energy landscape and capillary pressure in the context of morphological transitions has not been investigated in detail in the previous works.

Several authors have presented numerical solution of the Laplace equation for liquid bridges between two fibers to predict the capillary forces as a function of fiber distance

[131, 88, 105, 82]. Virozub et al. employed the Surface Evolver package to minimize numerically the surface free energy per unit length of each liquid body. They used an analytical expression to calculate the resultant forces, energies, and torques exerted by the liquid bridge on the fibers. The results suggest that stable symmetric bridges are favored at small fiber distance, whereas larger contact angles lead to coexistence of stable asymmetric and unstable symmetric configurations. The region of stability and transitions between these shapes were not further discussed.

Aziz and Tafreshi [82] reported experiments and numerical calculations of the mechanical forces between two fibers connected by a liquid bridge. The dependence of the force on fiber spacing was studied for parallel and orthogonal fiber configurations, and the detachment force of a pendant bridge was determined as a function of liquid volume. The numerical simulations always started with a cuboid-shaped droplet and the column to droplet transition was thus not observed in this setup.

Wu et al. [88] and Bedarkar et al. [105] extended the surface energy formulation by McHale and coworkers to the case fiber rails and also employed the Surface Evolver package to investigate the wetting morphology of droplet for varying liquid volume, fiber spacing, and contact angle. The results indicate that the dependence of the wetting length on the contact angle is strongly affected by the droplet morphology. Wu at al. [88] considered an additional bridge state, where the droplet shape does not engulf the fibers but only partially wraps the outside surfaces. The critical droplet volume and the surface energy of an engulfing barrel shape and the partially wrapping droplet bridge were determined using Surface Evolver. The numerical minimization of the surface energy allows to express the critical condition for absolute stability as a family of characteristic wetting curves in the volume-distance parameter space. The partially wrapping bridge state, which can exist for larger fiber distances, is different from the liquid column observed in experiments [132, 86]. Therefore, the wetting curves obtained by energy minimization do not necessarily capture the absolute minimum morphology. The transitions between different liquid configurations and the associated hysteresis thus remain incompletely understood.

CHAPTER 3

LATTICE BOLTZMANN METHOD

3.1 Lattice Boltzmann equation

Compared to the conventional CFD approach which solve the continuity equation and the Navier-Stokes equation using discrete schemes, lattice Boltzmann method stands out as a simplified mesoscopic description of fluid behavior by solving the linear lattice Boltzmann equation. The physics is more general in LBM without the need of complex physical model in traditional CFD. Owing to the mescoscale nature, LBM still contains the essential micro-physics and can achieve the desired macroscopic fluid flow behavior. In LBM, the fluid is described by a collection of particles which is represented by a distribution function. And the fluid motion can be tracked in the collision and streaming of these particles. Therefore, LBM can be regarded as an implicit solver for Navier-Stokes equation. The computation in LBM is local and can be adapted to fully parallel computing. Another advantage of LBM relies on the relative easy treatment of boundary condition of complex objects with arbitrary geometries. It has been widely applied to the simulation of mass-conserving flow in porous media since it is developed in the late 1980s[133]. A wide range of multiphase/multicomponent models has been proposed in LBM. These models belong to the class of diffuse interface methods, where the interfacial layer between immiscible fluid components has a finite width and the concentration of fluid components varies continuously at the interface. The width of the interface introduces a length scale that can take over the role of the slip length, making it well suited to handling moving boundaries problems.

3.1.1 Kinetic theory

The physics of fluid at the microscopic scale is essentially relied on the interaction between individual molecules, while for the macroscopic approach, the fluid is described in terms of measurable quantities in an arbitrary volume like density ρ, fluid velocity $\mathbf{u}$, pressure p and temperature T. Kinetic theory is an intermediate scale that considers the statistic distribution of gas particles. The distribution function $f(\mathbf{x}, \xi, t)$ of particles is introduced to represent the probability of finding a particle at a given position $\mathbf{x}$ and time t with the microscopic velocity ξ within REV. The macroscopic variables are connected to the distribution function by its moments as

$$\rho(\mathbf{x},t) = \int f(\mathbf{x}, \xi, t) d^3\xi, \tag{3.1}$$

$$\rho(\mathbf{x},t)\mathbf{u}(\mathbf{x},t) = \int \xi f(\mathbf{x}, \xi, t) d^3\xi, \tag{3.2}$$

$$\rho(\mathbf{x},t)E(\mathbf{x},t) = \frac{1}{2}\int |\xi|^2 f(\mathbf{x}, \xi, t) d^3\xi, \tag{3.3}$$

where E is the total energy density including the internal energy due to thermal motion and the kinetic energy due to the bulk motion. When the gas particles are left alone for sufficient time and can be considered to reach an equilibrium distribution, velocity of particles tends to vary around the mean velocity $\mathbf{u}$. The equilibrium distribution function follows Maxwell–Boltzmann distribution function

$$f^{\mathrm{eq}}(\mathbf{x}, \mathbf{v}, t) = \frac{\rho}{(2\pi RT)^{3/2}} e^{-\frac{\mathbf{v}^2}{2RT}}, \tag{3.4}$$

where $\mathbf{v}$ is the relative velocity, $\mathbf{v}(\mathbf{x},t) = \xi(\mathbf{x},t) - \mathbf{u}(\mathbf{x},t)$, R is the gas constant. Ludwig Boltzmann introduced the Boltzmann equation to describe the evolution of distribution function in time df/dt. The number of particles at the control volume $d\mathbf{x}$ and velocity range $d\xi$ may change due to the collision of particles. Therefore, we obtain the following Boltzmann equation by using the common collision operator $\Omega(f) = df/dt$ as a source term

$$\frac{\partial f}{\partial t} + \xi_\alpha \frac{\partial f}{\partial x_\alpha} + \frac{F_\alpha}{\rho} \frac{\partial f}{\partial \xi_\alpha} = \Omega(f), \tag{3.5}$$

where $F_\alpha/\rho = d\xi_\alpha/dt$ is the acceleration due to external force. The first two terms of the above equation are the advection of particles with a velocity ξ. The most commonly used BGK collision operator is put forward by Bhatnagar, Gross and Krook [134] as a simple approximation to the collision operator

$$\Omega(f) = -\frac{1}{\tau}(f - f^{\text{eq}}). \tag{3.6}$$

The collision of particles leads to the relaxation of the distribution function f towards local equilibrium f^{eq}. And the relaxation time τ is a constant that controls the speed to reach equilibrium. It is directly connected to the viscosity and thermal diffusivity in the transport phenomena.

3.1.2 From Boltzmann Kinetics to Navier-Stokes Equations

We can get the governing equations of continuum mechanics by taking moments of the Boltzmann Equation (3.5). Mass conservation equation can be obtained from the zeroth moment of Boltzmann Equation by directly integrating Eq. (3.5) over the velocity space $d^3\xi$:

$$\frac{\partial}{\partial t}\int f d^3\xi + \frac{\partial}{\partial x_\alpha}\int \xi_\alpha f d^3\xi + \frac{F_\alpha}{\rho}\int \frac{\partial f}{\partial \xi_\alpha} d^3\xi = \int \Omega(f) d^3\xi. \tag{3.7}$$

The RHS vanishes because the collision operator conserves the quantities of mass and momentum. The force term also vanishes assuming that the REV is much smaller than the volume of flowing fluid and at the REV scale, $f \to 0$ as $\xi \to \pm\infty$. Therefore, the above equation reduces to continuity equation according to the moments in Eq. (3.1) and (3.2):

$$\frac{\partial \rho}{\partial t} + \frac{\partial(\rho u_\alpha)}{\partial x_\alpha} = 0. \tag{3.8}$$

Similarly, we can take the first moment of Boltzmann equation by multiplying it by ξ_β and integrating over velocity space,

$$\frac{\partial}{\partial t}\int \xi_\beta f d^3\xi + \frac{\partial}{\partial x_\alpha}\int \xi_\alpha \xi_\beta f d^3\xi + \frac{F_\alpha}{\rho}\int \xi_\beta \frac{\partial f}{\partial \xi_\alpha} d^3\xi = \int \xi_\beta \Omega(f) d^3\xi. \tag{3.9}$$

The first term can be resolved according to Eq. (3.2). By splitting the particle velocity $\xi = \mathbf{u} + \mathbf{v}$, the second term can be decomposed to

$$\frac{\partial}{\partial x_\alpha}\int \xi_\alpha \xi_\beta f d^3\xi = \rho u_\alpha u_\beta + \int v_\alpha v_\beta f d^3\xi. \tag{3.10}$$

The force term can be evaluated by making use of $\xi_\beta \frac{\partial f}{\partial \xi_\alpha} = \frac{\partial(\xi_\alpha f)}{\partial \xi_\beta} - f$ and the fact that $\xi_\alpha f \to 0$ as $\xi_\alpha \to \pm\infty$. Thus, Eq. (3.9) simplifies to the Cauchy momentum equation:

$$\frac{\partial(\rho u_\beta)}{\partial t} + \frac{\partial(\rho u_\alpha u_\beta)}{\partial x_\alpha} = \frac{\partial \sigma_{\alpha\beta}}{\partial x_\alpha} + F_\alpha, \tag{3.11}$$

where $\sigma_{\alpha\beta} = -\int v_\alpha v_\beta f d^3\xi$ is a stress tensor. If the stress tensor takes the form of constitutive equation of Newtonian fluid, then Navier–Stokes momentum equation can be derived from Eq. (3.11).

3.1.3 Lattice Boltzmann equation

Although it is known that the lattice Boltzmann method is evolved from the lattice gas model proposed by Hardy, Pomeau, and de Pazzis in 1973 [135], here in this section, we discuss the derivation of lattice Boltzmann equation following the discretization of Boltzmann-BGK equation in velocity space, time and physical space. The main objective is to simplify the equilibrium distribution function and show that a finite discrete velocity set is sufficient to obtain the correct mass, momentum and energy conservation law. The equilibrium distribution function in Eq. (3.4) can be rewritten in the non-dimensional form as

$$f^{\mathrm{eq}}(\rho, \mathbf{u}, \theta, \xi) = \frac{\rho}{(2\pi\theta)^{3/2}} e^{-\frac{(\xi-\mathbf{u})^2}{2\theta}}, \tag{3.12}$$

where $\theta = c_s^2 = RT$ is the non-dimensional temperature, and c_s is the speed of sound in the gas. T is the temperature and R is the gas constant. For the case $|\xi|$, $|\mathbf{u}| \ll \sqrt{\theta}$, the equilibrium distribution function can be expanded in Taylor series approximately up to the second order as

$$f^{\mathrm{eq}}(\rho, \mathbf{u}, \theta, \xi) = \frac{\rho}{(2\pi\theta)^{3/2}} \exp\left(-\frac{\xi^2}{2\theta}\right)\left[1 + \frac{\xi \cdot \mathbf{u}}{\theta} + \frac{(\xi \cdot \mathbf{u})^2}{2\theta^2} - \frac{\mathbf{u}^2}{2\theta}\right] + O(Ma^3). \tag{3.13}$$

The associated hydrodynamic moments Ψ is calculated by the summation of all the distribution functions,

$$\Psi = \int \psi(\xi) f^{\mathrm{eq}} d\xi, \tag{3.14}$$

where $\psi(\xi)$ is the microscopic variable. The microscopic velocity and mean velocity is now rescaled by the thermal velocity $\mathbf{c}$ by $\xi = \sqrt{2\theta}\mathbf{c}$ and $\mathbf{u} = \sqrt{2\theta}\mathbf{u}^*$. Using the Gaussian-Hermite quadrature for approximating the integrals in Eq. (3.14) and combining with Eq. (3.13) yields

$$\Psi \approx \sum_{i=1}^{n} w_i \psi(c_i) \frac{\sqrt{2\theta}}{(2\pi\theta)^{3/2}} \left[1 + 2\mathbf{c}_i \cdot \mathbf{u}^* + (\mathbf{c}_i \cdot \mathbf{u}^*)^2 - \mathbf{u}^{*2}\right], \tag{3.15}$$

where w_i is the weight coefficient of the quadrature, and n is the number of discrete velocity.

It can be seen from the above equation that the continuous velocity ξ has been replaced by a set of discrete velocity $\mathbf{c}_i$. The discrete equilibrium distribution function is written as:

$$f_i^{\mathrm{eq}} = w_i\rho\left(1 + \frac{\mathbf{c}_i \cdot \mathbf{u}}{c_s^2} + \frac{(\mathbf{c}_i \cdot \mathbf{u})^2}{2c_s^4} - \frac{\mathbf{u}^2}{2c_s^2}\right). \tag{3.16}$$

The choice of discrete velocity set in LBM is not unique, but needs to be sufficiently well-resolved to obtain consistent solutions for Navier-Stokes equation, and also maintain a reasonable numerical computation cost [136]. The most often used velocity sets are D2Q9 (9 discrete velocities in 2D) and D3Q19 (19 discrete velocities in 3D). Here we take D3Q19 velocity set as an example. Fig. 3.1 show the discrete velocity set in D3Q19 lattice model. It has one rest velocity $\mathbf{c}_0 = 0$, 6 nearest velocity with length $|\mathbf{c}_{1-6}| = 1$, and 12 next nearest velocity with length $|\mathbf{c}_{7-18}| = \sqrt{2}$. The velocity set $\mathbf{c}_i$ is

$$\mathbf{c}_i = \begin{cases} (0,0,0) & i = 0 \\ (\pm1,0,0),(0,\pm1,0),(0,0,\pm1) & i = 1-6 \\ (\pm1,\pm1,0),(\pm1,0,\pm1),(0,\pm1,\pm1) & i = 7-18 \end{cases} \tag{3.17}$$

The weight w_i of the velocity set should satisfy two requirements. First one is to obey the mass and momentum conservation, and the second one is that the lattice velocity moments should be isotropic up to the fifth order. Therefore, the weight coefficient for D3Q19 lattice can be derived as [137]:

$$\mathbf{w}_i = \begin{cases} 1/3 & i = 0 \\ 1/18 & i = 1-6 \\ 1/36 & i = 7-18 \end{cases} \tag{3.18}$$

The equilibrium macroscopic moments can be obtained from the finite sum of Eq. (3.16)

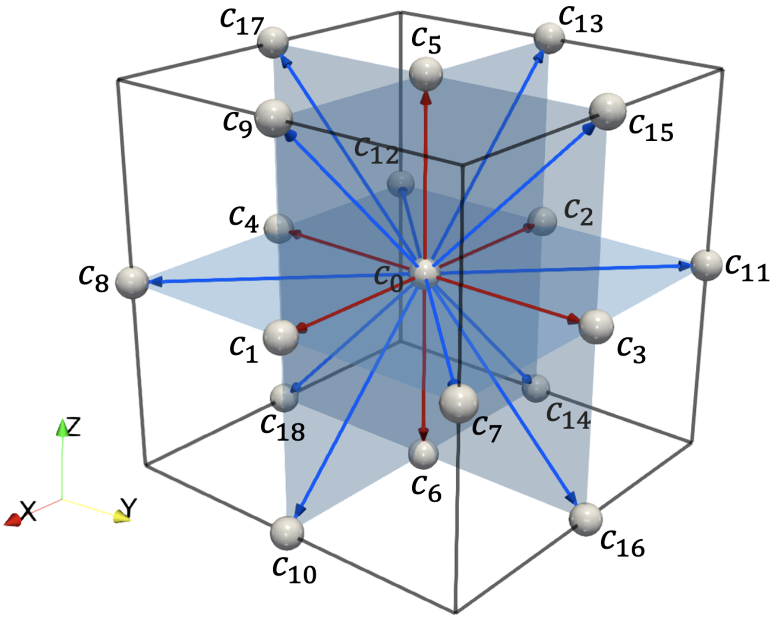

Figure 3.1: D3Q19 lattice model

and the isotropic condition of weight coefficient as

$$\rho = \sum_i f_i(\mathbf{x}, t) = \sum_i f_i^{\mathrm{eq}}(\mathbf{x}, t), \tag{3.19}$$

$$\rho\mathbf{u} = \sum_i \mathbf{c}_i f_i(\mathbf{x}, t) = \sum_i \mathbf{c}_i f_i^{\mathrm{eq}}(\mathbf{x}, t), \tag{3.20}$$

$$\rho\mathbf{uu} + p\mathbf{I} = \sum_i \mathbf{c}_i\mathbf{c}_i f_i(\mathbf{x}, t) = \sum_i \mathbf{c}_i\mathbf{c}_i f_i^{\mathrm{eq}}(\mathbf{x}, t), \tag{3.21}$$

where the equation of state in LBM is $p = \rho c_s^2$, and $\mathbf{I}$ is the identity matrix. We noticed that so far only velocity space is discretized in the above discussion. The discretization in time and physical space will be performed in the next step. Without the external force, Eq. (3.5) can be rewritten with the discretized velocity set as

$$\frac{\partial f_i}{\partial t} + c_{i\alpha}\frac{\partial f_i}{\partial x_\alpha} = \Omega(f_i). \tag{3.22}$$

Integrating the above equation along a trajectory $\mathbf{x} = \mathbf{x}_0 + h\mathbf{c}_i$, where h is a discrete time step, and $\mathbf{x}_0$ is an arbitrary constant, the lattice Boltzmann equation (LBE) can be obtained in the form:

$$f_i(\mathbf{x} + h\mathbf{c}_i, t + h) = f_i(\mathbf{x}, t) + h\Omega_i(\mathbf{x}, t). \tag{3.23}$$

Now the BGK collision operator can be incorporated in the LBE:

$$f_i(\mathbf{x} + h\mathbf{c}_i, t + h) = f_i(\mathbf{x}, t) - \frac{h}{\tau}[f_i(\mathbf{x}, t) - f_i^{\mathrm{eq}}(\mathbf{x}, t)], \tag{3.24}$$

with a redefined relaxation time $\bar{\tau} = \tau + h/2$, the above LBGK equation can be shown to achieve a second-order accuracy in time [138]. The LBGK equation actually consists of two steps. In the collision step, the distribution function after collision $f_i^*(\mathbf{x}, t)$ is expressed as

$$f_i^*(\mathbf{x}, t) = f_i(\mathbf{x}, t) - \frac{h}{\tau}[f_i(\mathbf{x}, t) - f_i^{\mathrm{eq}}(\mathbf{x}, t)]. \tag{3.25}$$

The computation of $f_i^*(\mathbf{x}, t)$ is restricted to within nodes $\mathbf{x}$, therefore, it is purely local. This step describes the variation of distribution function due to collisions at each lattice site. In the streaming step, the particles after collision stream along the discrete velocity set to the neighboring sites, given by:

$$f_i(\mathbf{x} + h\mathbf{c}_i, t + h) = f_i^*(\mathbf{x}, t). \tag{3.26}$$

The streaming step describes the interaction between neighboring nodes by the shift of particles, which is a non-local but linear operation. The kinematic viscosity of the fluid is dependent on the relaxation time τ and given by:

$$\nu = c_s^2(\tau - \frac{1}{2})h. \tag{3.27}$$

To maintain a positive viscosity and numerical stability, $\tau/h \geq 1/2$ must be satisfied. The macroscopic hydrodynamic variables, density ρ and fluid velocity $\mathbf{u}$ are obtained as the moments of distribution funciton, i.e.

$$\begin{aligned} \rho(\mathbf{x},t) &= \sum_i f_i(\mathbf{x},t), \\ \rho\mathbf{u}(\mathbf{x},t) &= \sum_i \mathbf{c}_i f_i(\mathbf{x},t). \end{aligned} \tag{3.28}$$

3.1.4 From Lattice Boltzmann to Navier-Stokes

In order to use the discrete LBE to simulate the behavior of fluid flow, we will show that the macroscopic continuity and Navier-Stokes momentum equation can be recovered via the multiscale Chapman-Enskog expansion. We define the Knudsen number $Kn = \varepsilon$ as the ratio of molecular mean free path to the characteristic length scale $Kn = l_{\mathrm{mfp}}/l$. Using the Knudsen number Kn as the expansion parameter, the distribution function f_i can be expanded around the equilibrium distribution f_i^{eq} as

$$f_i = f_i^{\mathrm{eq}} + \varepsilon f_i^{(1)} + \varepsilon^2 f_i^{(2)} + \ldots, \quad \varepsilon = Kn. \tag{3.29}$$

In this perturbation analyses, the two lowest orders can provide sufficient accuracy to find Navier-Stokes equation. The expansion of spatial and time derivative can be written in a similar way:

$$\nabla = \varepsilon \nabla^{(1)}, \tag{3.30}$$

$$\frac{\partial}{\partial t} = \varepsilon \frac{\partial}{\partial t^{(1)}} + \varepsilon^2 \frac{\partial}{\partial t^{(2)}} + \ldots, \tag{3.31}$$

The different components in $\partial/\partial t$ are the terms corresponding to the different orders of Kn, and the summation of them equals to the time derivative. The first step of the Chapman-

Enskog expansion for the LBE is the Taylor expansion of Eq. (3.24), written as

$$h(\frac{\partial}{\partial t}+\mathbf{c}_i\cdot\nabla)f_i+\frac{h^2}{2}(\frac{\partial}{\partial t}+\mathbf{c}_i\cdot\nabla)^2 f_i+O(h^3)=-\frac{h}{\tau}f_i^{\mathrm{neq}}, \tag{3.32}$$

which is identical to Eq. (3.22), apart from the higher-order derivative terms. We can find the following equation by separating the above equation into terms of the two lowest orders in *Kn*:

$$\varepsilon: \quad \frac{\partial f_i^{\mathrm{eq}}}{\partial t^{(1)}}+\mathbf{c}_i\cdot\nabla^{(1)}f_i^{\mathrm{eq}}=-\frac{1}{\tau}f_i^{(1)}, \tag{3.33}$$

$$\varepsilon^2: \quad \frac{\partial f_i^{\mathrm{eq}}}{\partial t^{(2)}}+(\frac{\partial}{\partial t^{(1)}}+\mathbf{c}_i\cdot\nabla^{(1)})(1-\frac{h}{2\tau})f_i^{(1)}=-\frac{1}{\tau}f_i^{(2)}. \tag{3.34}$$

Taking the zeroth moments of the above equations by summing over i, we can find:

$$\frac{\partial\rho}{\partial t^{(1)}}+\nabla^{(1)}\cdot(\rho\mathbf{u})=0, \tag{3.35}$$

$$\frac{\partial\rho}{\partial t^{(2)}}=0, \tag{3.36}$$

In the first order in *Kn*, Eq. (3.35) represents the continuity equation. Taking the first moments of Eq. (3.33) and (3.34) by multiplying by c_i, we can find:

$$\frac{\partial\rho\mathbf{u}}{\partial t^{(1)}}+\nabla^{(1)}\cdot\Pi^{(0)}=0, \tag{3.37}$$

$$\frac{\partial\rho\mathbf{u}}{\partial t^{(2)}}+\nabla^{(1)}(1-\frac{h}{2\tau})\cdot\Pi^{(1)}=0, \tag{3.38}$$

where Π are the general notation of moments [136]

$$\Pi^{(0)} = \sum f_i^{\mathrm{eq}} \mathbf{c}_i \mathbf{c}_i = \rho \mathbf{u}\mathbf{u} + \rho c_s^2 \mathbf{I}, \tag{3.39}$$

$$\Pi^{(1)} = \sum f_i^{(1)} \mathbf{c}_i \mathbf{c}_i = -\rho c_s^2 \tau \nabla \mathbf{u} + \tau \nabla (\rho \mathbf{u}\mathbf{u}\mathbf{u}). \tag{3.40}$$

The error term $\tau \nabla(\rho \mathbf{u}\mathbf{u}\mathbf{u})$ can be neglected if $u^2 \ll c_s^2$, when the Mach number is much less than one ($Ma = u/c_s \ll 1$). Thus, LBM is considered to be valid for weakly compressible fluids. Summing up Eq. (3.37) and (3.38) for momentum from their $O(\varepsilon)$ and $O(\varepsilon^2)$ components, we obtain:

$$\left(\varepsilon \frac{\partial}{\partial t^{(1)}} + \varepsilon^2 \frac{\partial}{\partial t^{(2)}}\right)(\rho \mathbf{u}) + \varepsilon \nabla^{(1)} \cdot \Pi^{(0)} = -\varepsilon^2 \nabla^{(1)} (1 - \frac{h}{2\tau}) \cdot \Pi^{(1)}. \tag{3.41}$$

Substituting Eq. (3.39) and (3.40) back to Eq. (3.41) and reserving the spatial and time derivative expansion from Eq. (3.30) and (3.31), the Navier-Stokes momentum equation can be derived as:

$$\frac{\partial \rho \mathbf{u}}{\partial t} + \nabla \cdot (\rho \mathbf{u}\mathbf{u}) = -\nabla p + \nabla \cdot (\eta \nabla \mathbf{u}), \tag{3.42}$$

where the pressure $p = \rho c_s^2$, $\eta = \rho c_s^2 (\tau - h/2)$ is the dynamic viscosity. As seen in the expression for shear viscosity, the relaxation time τ/h must be greater than $1/2$ in order to have a positive viscosity.

3.2 Multiple relaxation time (MRT) scheme

It can be found in the previous section that the relaxation time only enters the first moment of Eq. (3.34) $\Pi^{(1)}$ for LBGK model, while the multiple relaxation time (MRT) collision operator allows independent relaxation rate towards equilibrium for each moment [139], directly corresponding to the hydrodynamic moments. In order to overcome the stability (low viscosity, i.e. τ close to $1/2$) and accuracy (large velocity magnitude) issue in LBGK model, MRT scheme has been constructed with more degrees of freedom to achieve better stability and accuracy. Instead of using a single relaxation time τ in LBGK model, the collision term is relaxed by a collision matrix Λ_{ij}

$$f_i(\mathbf{x}+h\mathbf{c}_i, t+h) - f_i(\mathbf{x}, t) = -\sum_j \Lambda_{ij}\left[f_j(\mathbf{x}, t) - f_j^{\mathrm{eq}}(\rho, \mathbf{u})\right]. \tag{3.43}$$

The collision is performed in the moments space rather than the distribution function. Moments space is mapped to the distribution function f_i through a transformation matrix $\mathbf{M}$ by

$$\mathbf{m} = \mathbf{M}\mathbf{f}, \tag{3.44}$$

where $\mathbf{f}$ is the vector of all the distribution functions for the lattice site, i.e. $(f_0, f_1, f_2, ...f_n)^T$, $\mathbf{m}$ is the moment vector, $\mathbf{m} = (m_0, m_1, m_2, ...m_n)^T$. For D3Q19 lattice, the moment vector is arranged as

$$\mathbf{m} = (\rho, e, \varepsilon, j_x, q_x, j_y, q_y, j_z, q_z, 3p_{xx}, 3\tau_{xx}, p_{ww}, \tau_{xx}, p_{xy}, p_{yz}, p_{xz}, m_x, m_y, m_z)^T. \tag{3.45}$$

These correspond to the mass density ρ, kinetic energy e, kinetic energy square ε, momentum j_x, j_y, j_z, the energy flux independent of the mass flux q_x, q_y, q_z, the symmetric traceless viscous stress tensor p_{ij}, with $p_{xx} + p_{yy} + p_{zz} = 0$ and $p_{ww} = p_{yy} - p_{zz}$ [139]. The additional moments are higher-order moments, which do not affect hydrodynamics. The moment vectors define the transformation matrix $\mathbf{M}$ for D3Q19 lattice model as

$$\mathbf{M} = \begin{pmatrix}
1 & 1 & 1 & 1 & 1 & 1 & 1 & 1 & 1 & 1 & 1 & 1 & 1 & 1 & 1 & 1 & 1 & 1 & 1 \\
-30 & -11 & -11 & -11 & -11 & -11 & -11 & 8 & 8 & 8 & 8 & 8 & 8 & 8 & 8 & 8 & 8 & 8 & 8 \\
12 & -4 & -4 & -4 & -4 & -4 & -4 & 1 & 1 & 1 & 1 & 1 & 1 & 1 & 1 & 1 & 1 & 1 & 1 \\
0 & 1 & -1 & 0 & 0 & 0 & 0 & 1 & -1 & 1 & -1 & 0 & 0 & 1 & -1 & 1 & -1 & 0 & 0 \\
0 & -4 & 4 & 0 & 0 & 0 & 0 & 1 & -1 & 1 & -1 & 0 & 0 & 1 & -1 & 1 & -1 & 0 & 0 \\
0 & 0 & 0 & 1 & -1 & 0 & 0 & 1 & -1 & 0 & 0 & 1 & -1 & -1 & 1 & 0 & 0 & 1 & -1 \\
0 & 0 & 0 & -4 & 4 & 0 & 0 & 1 & -1 & 0 & 0 & 1 & -1 & -1 & 1 & 0 & 0 & 1 & -1 \\
0 & 0 & 0 & 0 & 0 & 1 & -1 & 0 & 0 & 1 & -1 & 1 & -1 & 0 & 0 & -1 & 1 & -1 & 1 \\
0 & 0 & 0 & 0 & 0 & -4 & 4 & 0 & 0 & 1 & -1 & 1 & -1 & 0 & 0 & -1 & 1 & -1 & 1 \\
0 & 2 & 2 & -1 & -1 & -1 & -1 & 1 & 1 & 1 & 1 & -2 & -2 & 1 & 1 & 1 & 1 & -2 & -2 \\
0 & -4 & -4 & 2 & 2 & 2 & 2 & 1 & 1 & 1 & 1 & -2 & -2 & 1 & 1 & 1 & 1 & -2 & -2 \\
0 & 0 & 0 & 1 & 1 & -1 & -1 & 1 & 1 & -1 & -1 & 0 & 0 & 1 & 1 & -1 & -1 & 0 & 0 \\
0 & 0 & 0 & -2 & -2 & 2 & 2 & 1 & 1 & -1 & -1 & 0 & 0 & 1 & 1 & -1 & -1 & 0 & 0 \\
0 & 0 & 0 & 0 & 0 & 0 & 0 & 1 & 1 & 0 & 0 & 0 & 0 & -1 & -1 & 0 & 0 & 0 & 0 \\
0 & 0 & 0 & 0 & 0 & 0 & 0 & 0 & 0 & 0 & 0 & 1 & 1 & 0 & 0 & 0 & 0 & -1 & -1 \\
0 & 0 & 0 & 0 & 0 & 0 & 0 & 0 & 0 & 1 & 1 & 0 & 0 & 0 & 0 & -1 & -1 & 0 & 0 \\
0 & 0 & 0 & 0 & 0 & 0 & 0 & 1 & -1 & -1 & 1 & 0 & 0 & 1 & -1 & -1 & 1 & 0 & 0 \\
0 & 0 & 0 & 0 & 0 & 0 & 0 & -1 & 1 & 0 & 0 & 1 & -1 & 1 & -1 & 0 & 0 & 1 & -1 \\
0 & 0 & 0 & 0 & 0 & 0 & 0 & 0 & 0 & 1 & -1 & -1 & 1 & 0 & 0 & -1 & 1 & 1 & -1
\end{pmatrix}$$

The individual moments m_k can be obtained from the distribution function f_i as

$$m_k = \sum_i M_{ki} f_i. \tag{3.46}$$

Hence, the collision term in Eq. 3.43 can be transformed into the moment space as

$$f_i(\mathbf{x} + h\mathbf{c}_i, t + h) - f_i(\mathbf{x}, t) = -\mathbf{M}^{-1}\mathbf{S}[\mathbf{m}(\mathbf{x}, t) - \mathbf{m}^{\text{eq}}(\mathbf{x}, t)], \tag{3.47}$$

where the equilibrium moment vector $\mathbf{m}^{\text{eq}} = \mathbf{M}\mathbf{f}^{\text{eq}}$, and $\mathbf{S}$ is a diagonal matrix of collision parameters $\mathbf{S} = \text{diag}(s_1, s_2, s_3, ...s_n)$. The relaxation matrix $\mathbf{S}$ contains individual relaxation time for every moment $\tau_i = s_i^{-1}$. A common choice for the collision matrix of the D3Q19 lattice is $\text{diag}\{s_i\} = \text{diag}(0, 1/\tau_{\text{bulk}}, 1.4, 0, 1.2, 0, 1.2, 0, 1.2, 1/\tau, 1.4, 1/\tau, 1.4, 1/\tau, 1/\tau, 1/\tau,$ $1.98, 1.98, 1.98)$, where τ_{bulk} controls the bulk viscosity by $\eta_B = \frac{1}{9}(2\tau_{\text{bulk}} - 1)$ [139].

In the collision step, the moments $\mathbf{m}$ and $\mathbf{m}^{\text{eq}}$ are calculated directly. The post-collision moments m_i^* are determined in a BGK manner:

$$m_i^*(\mathbf{x},t) = m_i(\mathbf{x},t) - s_i[m_i(\mathbf{x},t) - m^{\mathrm{eq}}(\mathbf{x},t)]. \tag{3.48}$$

To transform back from moment space to population space, the distribution function after collision f_i^* can be obtained by multiplying the inverse of transformation matrix:

$$f_i^*(\mathbf{x},t) = \sum_k m_k^*(\mathbf{x},t) M_{ik}^{-1}. \tag{3.49}$$

Finally, the streaming step is carried out in the distribution function space, same as in LBGK model:

$$f_i(\mathbf{x} + h\mathbf{c}_i, t + h) = f_i^*(\mathbf{x},t). \tag{3.50}$$

Implying that the distribution function f_i at position $\mathbf{x} + h\mathbf{c}_i$ and time moment $t + h$ is calculated from the known function f_i^* taken at position $\mathbf{x}$ and time moment t.

3.3 Boundary conditions

The formulation of boundary condition in LBM is non-trivial but needs special treatment in order to ensure the numerical accuracy of calculated flow field. Instead of imposing boundary condition through the macroscopic properties ρ and $\mathbf{u}$ at boundary nodes, the boundary conditions are applied to the distribution function f_i in LBM. Therefore, it is required to determine f_i from the macroscopic information.

3.3.1 Periodic boundary condition

The simplest boundary condition can be applied to domain boundaries is the periodic boundary condition (PBC). It can be used when the flow is periodic or the bulk fluid is far away from the boundaries so that the influence of boundaries can be ignored. Periodic boundary condition in LBM is straightforward. At the boundary nodes, the unknown incoming population $f_i(\mathbf{x},t)$ are given by those leaving the simulation domain at the other side, namely

$$f_i(\mathbf{x},t) = f_i(\mathbf{x}+\mathbf{L},t). \tag{3.51}$$

3.3.2 Bounce back boundary condition

Bounce back method is the most common used boundary condition for fluid-solid interface due to its simplicity in handling complex boundaries. No-slip condition can be achieved using the bounce back scheme. The term "bounce back" means the density hitting a rigid wall be reflected back to where it comes from, as illustrated in Fig. 3.2 for xz plane in D3Q19 lattice. For the standard bounce back method, the boundary nodes are located on the solid nodes, introducing a first-order accuracy [140]. In this scheme, the collision process does not occur. The unknown populations propagated from the solid sites at time $t+h$ is replaced by the populations moving towards the boundary wall at time t, i.e.

$$\begin{aligned} f_5(\mathbf{x},t+h) &= f_6(\mathbf{x},t), \\ f_{13}(\mathbf{x},t+h) &= f_{10}(\mathbf{x},t), \\ f_9(\mathbf{x},t+h) &= f_{14}(\mathbf{x},t). \end{aligned} \tag{3.52}$$

It can be written in a general form:

$$f_{-i}(\mathbf{x},t+h) = f_i(\mathbf{x},t), \tag{3.53}$$

where $-i$ is the conjugate link to i, $\mathbf{c}_{-i} = \mathbf{c}_i$. For the mid-link bounce back method, the boundary is located at the midway between solid and liquid nodes, making the method second-order accurate [141]. Fig. 3.2b illustrates the explicit scheme of mid-link bounce back method. In the streaming step, the unknown populations are replaced by the post-

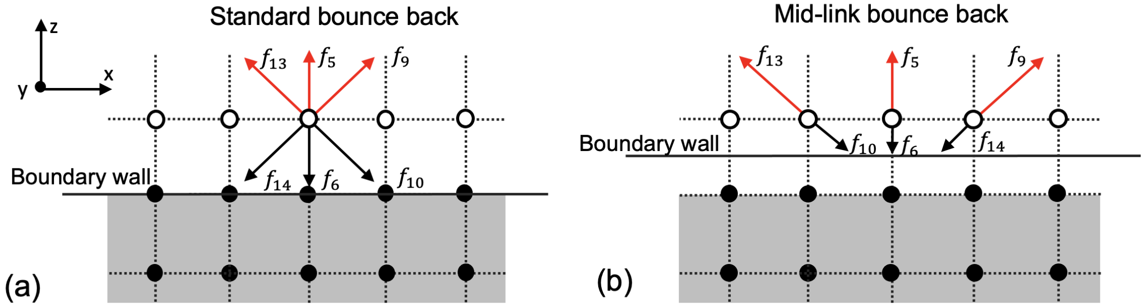

Figure 3.2: Schematic plot of projection of D3Q19 model in y-direction. (a) Standard bounce back boundary condition, where the boundary is located on the solid nodes. (b) Mid-link bounce back boundary condition, where the boundary is located midway between solid (solid circles) and fluid nodes (open circles). The bottom grey region represents the solid region and the top region is fluid region.

collision populations f_i^*, i.e.

$$\begin{aligned} f_5(\mathbf{x}, t+h) &= f_6^*(\mathbf{x}, t), \\ f_{13}(\mathbf{x}, t+h) &= f_{10}^*(\mathbf{x}, t), \\ f_9(\mathbf{x}, t+h) &= f_{14}^*(\mathbf{x}, t). \end{aligned} \tag{3.54}$$

The general form of mid-link bounce back scheme is:

$$f_{-i}(\mathbf{x}, t+h) = f_i^*(\mathbf{x}, t). \tag{3.55}$$

3.3.3 Pressure and velocity boundary condition

Zou and He proposed a method to specify the pressure and velocity at planar boundaries for D2Q9 and D3Q15 lattice[142]. Their method is based on the idea of bounce-back of the non-equilibrium part. Hecht and Harting extended this approach to D3Q19 lattice[143]. According to the continuity equation $\frac{\partial \rho}{\partial t} + \nabla \cdot (\rho \mathbf{u}) = 0$, three out of four variables need to be specified on the boundary.

The pressure boundary condition, in which the density is imposed, is applied as follows. For D3Q19 model in Fig. 3.1, suppose that the inlet is on the bottom plane ($z = 0$) with a specified density ρ_0 and tangential velocity u_x, u_y. The components pointing into the system, f_5, f_9, f_{13}, f_{15} and f_{17} are undetermined. Firstly, Eq. 3.28 is applied on the inlet as

$$\rho_0 = \sum_i^{19} f_i, \tag{3.56}$$

$$\rho_0 u_x = f_1 + f_7 + f_8 + f_9 + f_{10} - (f_2 + f_{11} + f_{12} + f_{13} + f_{14}), \tag{3.57}$$

$$\rho_0 u_y = f_3 + f_7 + f_{11} + f_{15} + f_{16} - (f_4 + f_8 + f_{12} + f_{17} + f_{18}), \tag{3.58}$$

$$\rho_0 u_z = f_5 + f_9 + f_{13} + f_{15} + f_{17} - (f_6 + f_{10} + f_{14} + f_{16} + f_{18}), \tag{3.59}$$

From Eq. 3.56 and 3.59, the unknown velocity component u_z can be calculated as

$$u_z = 1 - \frac{1}{\rho_0}[f_1 + f_2 + f_3 + f_4 + f_7 + f_8 + f_{11} + f_{12} + f_{19} + 2(f_6 + f_{10} + f_{14} + f_{16} + f_{18})]. \tag{3.60}$$

In the above equation systems, we need to determine five unknowns (f_5, f_9, f_{13}, f_{15} and f_{17}). More constraints are added to solve the equations by assuming that the bounce-back rule is still valid for the non-equilibrium part f_i^* at the boundary [142]:

$$f_i^* = f_i - f_i^{\text{eq}}. \tag{3.61}$$

This condition can be written explicitly in z direction as:

$$\begin{cases} f_5 - f_5^{\mathrm{eq}} = f_6 - f_6^{\mathrm{eq}}, \\ f_9 - f_9^{\mathrm{eq}} = f_{14} - f_{14}^{\mathrm{eq}}, \\ f_{13} - f_{13}^{\mathrm{eq}} = f_{10} - f_{10}^{\mathrm{eq}}, \\ f_{15} - f_{15}^{\mathrm{eq}} = f_{18} - f_{18}^{\mathrm{eq}}, \\ f_{17} - f_{17}^{\mathrm{eq}} = f_{16} - f_{16}^{\mathrm{eq}}. \end{cases} \tag{3.62}$$

We can obtain the following equations by substituting the equilibrium distribution function in Eq. (3.16)

$$f_5 = f_6 + \frac{2w_5}{c_s^2}\rho_0 u_z, \tag{3.63}$$

$$f_9 = f_{14} + \frac{2w_9}{c_s^2}\rho_0(u_z + u_x), \tag{3.64}$$

$$f_{13} = f_{10} + \frac{2w_{13}}{c_s^2}\rho_0(u_z - u_x), \tag{3.65}$$

$$f_{15} = f_{18} + \frac{2w_{15}}{c_s^2}\rho_0(u_z + u_y), \tag{3.66}$$

$$f_{17} = f_{16} + \frac{2w_{17}}{c_s^2}\rho_0(u_z - u_y). \tag{3.67}$$

These equation, together with Eq. (3.56) to (3.59) overdetermines the system of equations. Hecht et al. [143] introduced two transversal momentum corrections on the $z-$boundary for distribution propagating in x and y direction, N_x^z and N_y^z, which are not zero if there are velocity gradients. The above equations are corrected by N_x^z and N_y^z as follows:

$$f_9 = f_{14} + \frac{2w_9}{c_s^2}\rho_0(u_z + u_x) - N_x^z, \tag{3.68}$$

$$f_{13} = f_{10} + \frac{2w_{13}}{c_s^2}\rho_0(u_z - u_x) + N_x^z, \tag{3.69}$$

$$f_{15} = f_{18} + \frac{2w_{15}}{c_s^2}\rho_0(u_z + u_y) - N_y^z, \tag{3.70}$$

$$f_{17} = f_{16} + \frac{2w_{17}}{c_s^2}\rho_0(u_z - u_y) + N_y^z. \tag{3.71}$$

Substituting Eq. (3.68)-(3.71) into Eq. (3.57) and (3.58), we obtain the solution for N_x^z and N_y^z:

$$N_x^z = \frac{1}{2}[f_1 + f_7 + f_8 - (f_2 + f_{11} + f_{12})] - \frac{1}{3}\rho u_x, \tag{3.72}$$

$$N_y^z = \frac{1}{2}[f_3 + f_7 + f_{11} - (f_4 + f_8 + f_{12})] - \frac{1}{3}\rho u_y. \tag{3.73}$$

Inserting Eq. (3.72) into Eq. (3.68) gives the distribution functions of unknowns. Similarly, three velocity components can be specified for the velocity boundary condition, and the unknown density ρ and distribution function can be determined.

3.4 Multiphase multi-component models

LBM has emerged as an efficient alternative to the traditional computation fluid dynamics (CFD) in the simulation of multiphase multi-component flow through complex porous media [145, 146, 147, 148, 149]. Owing to the mesoscale nature of LBM, it is capable of capturing both the microscale droplet dynamics and macroscopic fluid displacement features in the porous media. In the CFD simulations, the particulate character of fluid is neglected, hence the multiphase flow models are solved using coupled methods for free moving boundary problem. And molecular dynamics (MD) simulations for

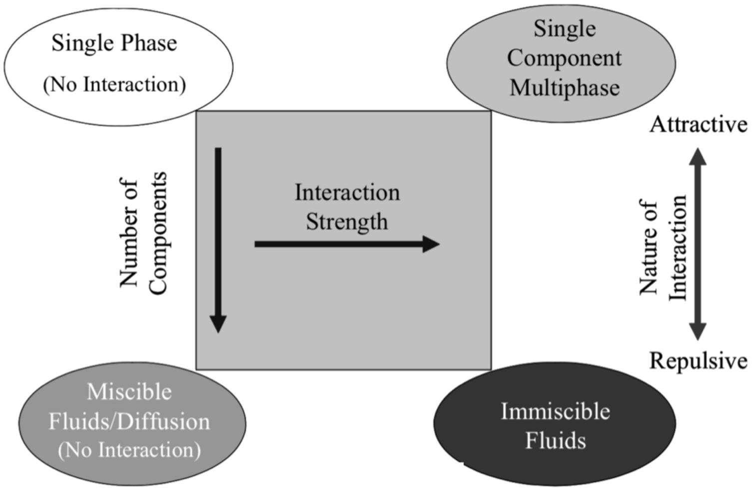

Figure 3.3: Conceptual framework for multiphase/multi-component LBM model. Reproduced from Ref. [144] with permission of Springer.

multiphase flow require high computation cost [150]. There are a number of multiphase multi-component LBM models that have been proposed to describe the evolution of interfacial dynamics [26, 151, 152, 153, 154]. The simulation of multiphase/multi-component system is distinguished from single homogeneous phase fluid by including the interaction between different phases or components. Fig. 3.3 illustrates the conceptual framework of multiphase/multi-component LBM model [144]. The single phase system involves only one fluid component which is not subjected to any long-range interaction force. Adding the long-range attractive interaction to the single phase system allows phase separation into liquid and vapor phase. If a second fluid component is added into the system, we can simulate the miscible fluids in the absence of long range interaction, and immiscible fluids when there exists a repulsive interaction between the different components.

The earliest one of these methods is the color-gradient model [155, 156] based on Rothman-Keller multiphase lattice gas model [157]. The advantage of color-gradient model is that viscosity ratio and surface tension can be controlled separately [158]. However, the maximum density ratio is limited to the order of $O(10)$ [159]. While the pseudopotential

Shan-Chen (SC) model has received more attention since it is developed in 1993 [151]. SC single component multiphase model (SCMP) can also be applied for the density ratio of order $O(10^2)$ [160]. The free energy model is proposed by Swift et al. in 1995 [152], starting from the free-energy functional that is always thermodynamically consistent.

3.4.1 The Shan-Chen model: a "bottom-up" approach

Pseudopotential model developed by Shan and Chen is one of the most widely used multiphase and multicomponent model to describe the surface interaction of immiscible fluids by incorporating an interaction force into LBE [26, 151, 161]. It starts with the microscopic interaction between neighboring particles and leads to the macroscopic phase separation behavior. Therefore, it is called a "bottom-up" approach.

Multiple fluid components can be incorporated in the lattice Boltzmann method by using multiple sets of populations f_i^σ for each component, where $\sigma = 1, 2, ...N$ indexes the components, and f_i^σ is the distribution function of the component σ. Following Shan and Chen [151, 26], the effective force acting on the σth components owing to the nearest-neighbors has the following form:

$$\mathbf{F}_\sigma(\mathbf{x},t) = -\psi_\sigma(\mathbf{x},t)\sum_{\bar{\sigma}} g_{\sigma\bar{\sigma}} \sum_{\mathbf{x}'} w_i \psi_{\bar{\sigma}}(\mathbf{x}',t)(\mathbf{x}'-\mathbf{x}), \tag{3.74}$$

where $g_{\sigma\bar{\sigma}}$ determines the interaction strength between fluid component σ and $\bar{\sigma}$. A positive value of $g_{\sigma\bar{\sigma}}$ corresponds to repulsive interactions that lead to demixing. The sum over $\mathbf{x}'$ runs over the neighboring lattice sites that are connected to $\mathbf{x}$ by a discrete velocity vector $\mathbf{x}'-\mathbf{x} = h\mathbf{c}_i$. The effective mass ψ_σ of component σ is a monotonous function of density $\rho_\sigma(\mathbf{x},t)$, given by

$$\psi_\sigma(\mathbf{x},t) = \psi[\rho_\sigma(\mathbf{x},t)] = 1 - \exp[-\rho_\sigma(\mathbf{x},t)/\rho_0], \tag{3.75}$$

with a reference density ρ_0.

In the implementation used in this Thesis, in order to describe the dynamic forces, the SC forces are incorporated in the collision operator by adding the shift velocity to the fluid velocity . Accordingly, the hydrodynamic velocity $\mathbf{u}(\mathbf{x},t)$ is given by

$$\mathbf{u}(\mathbf{x},t) = \frac{1}{\rho(\mathbf{x},t)} \sum_{\sigma} \left[\sum_{i} f_i(\mathbf{x},t)\mathbf{c}_i + \frac{h}{2}\mathbf{F}_\sigma(\mathbf{x},t) \right]. \tag{3.76}$$

The introduction of interaction forces leads to a correction of the ideal equation of state $p = \rho c_s^2$ for a gas of density ρ, thus the pressure tensor $P_{ij}(\mathbf{x})$ is computed as: [162]

$$\begin{aligned} P_{ij}(\mathbf{x}) = &\sum_{\sigma}\sum_{k} \rho_\sigma(\mathbf{x})(c_{ki} - u_i(\mathbf{x}))(c_{kj} - u_j(\mathbf{x})) + \frac{1}{4}\sum_{\sigma,\bar{\sigma}} g_{\sigma\bar{\sigma}} \sum_{x'} [\psi_\sigma(\mathbf{x})\psi_{\bar{\sigma}}(\mathbf{x}') \\ &+ \psi_{\bar{\sigma}}(\mathbf{x})\psi_\sigma(\mathbf{x}')](\mathbf{x} - \mathbf{x}')^2. \end{aligned} \tag{3.77}$$

where c_{ki} is the Cartesian component of k-th velocity vector $\mathbf{c}_k$, $k = 0, \ldots, 18$ for D3Q19 lattice model. The interfacial tension $\gamma_{\sigma\bar{\sigma}}$ between the two components σ and $\bar{\sigma}$, for example, water and oil is the integral of the difference between normal pressure tensor P_n and the transversal pressure tensor P_t across the flat interface. For a planar interface developed along the z-axis, where $P_n = P_{zz}$ and $P_t = P_{xx} = P_{yy}$, the interfacial tension $\gamma_{\sigma\bar{\sigma}}$ is given by

$$\gamma_{\sigma\bar{\sigma}} = \int [P_{zz}(z) - P_{xx}(z)]dz, \tag{3.78}$$

It can be calibrated to a desired value by adjusting the interaction strength $g_{\sigma\bar{\sigma}}$. From Eq. (3.77) and (3.78), it is noted that the interfacial tension is an emergent result of interaction force, hence depends on the density ρ and interaction strength $g_{\sigma\bar{\sigma}}$. It cannot be adjusted independently of density [162]. This is the main disadvantage of the Shan-Chen model.

To describe the liquid-solid interactions, it is convenient to treat the solid as a virtual component and introduce a liquid-solid interaction force analogous to the liquid-liquid interaction force as [163]

$$\mathbf{F}_s^{\sigma}(\mathbf{x},t) = -g_{s,\sigma}\psi_{\sigma}(\mathbf{x},t)\sum_{\mathbf{x}'}\psi(\rho_s^{\sigma})(\mathbf{x}'-\mathbf{x})s(\mathbf{x}',t), \tag{3.79}$$

where $s(\mathbf{x}',t)$ is 1 if $\mathbf{x}$ is a solid site and 0 if it is a fluid site, $g_{s,\sigma}$ is the interaction strength between fluid component σ and the solid wall, and ρ_s^{σ} is a virtual wall density. ρ_s^{σ} is a tunable parameter to specify the wettability of the solid substrate. $\rho_s^{\sigma} = 0$ corresponds to a neutral wetting condition. A negative ρ_s^{σ} is the wettable condition for σ component, and positive value is non-wettable. The Young's equation can be written in the form [164]

$$\cos\theta = \frac{g_{s,\sigma}(\rho_s^{\sigma}-\rho^{\sigma}) - g_{s,\bar{\sigma}}(\rho_s^{\bar{\sigma}}-\rho^{\bar{\sigma}})}{g_{\sigma\bar{\sigma}}(\rho^{\sigma}-\rho^{\bar{\sigma}})}. \tag{3.80}$$

This provides a convenient way to adjust the contact angle through the virtual wall density. If the same interaction strength is used for fluid-fluid and fluid-solid interactions $g_{s,\sigma} = g_{s,\bar{\sigma}} = g_{\sigma\bar{\sigma}}$, the estimated contact angle depends only on the density ratio [163]

$$\cos\theta = \frac{\rho_s^{\sigma}-\rho_s^{\bar{\sigma}}}{\rho^{\sigma}-\rho^{\bar{\sigma}}} - 1. \tag{3.81}$$

The contact angle can be calibrated through the measurements of a droplet on flat substrate or in a duct [164].

One of the limitation of Shan-Chen model is the large spurious current around the interface of a droplet. The Shan-Chen force $\mathbf{F}_{\sigma}$ can be rewritten in the following form using Taylor expansion of the effective mass $\psi_{\bar{\sigma}}(\mathbf{x}+h\mathbf{c}_i)$:

$$\begin{aligned}\mathbf{F}_{\sigma}(\mathbf{x},t) = -\psi_{\sigma}(\mathbf{x},t)\sum_{\bar{\sigma}} g_{\sigma\bar{\sigma}}\sum_i w_i\mathbf{c}_i h[\psi_{\bar{\sigma}}(\mathbf{x},t) + c_i h\nabla\psi_{\bar{\sigma}}(\mathbf{x},t) \\ + \frac{1}{2}c_ic_ih^2\nabla^2\psi_{\bar{\sigma}}(\mathbf{x},t) + \frac{1}{6}c_ic_ic_ih^3\nabla\Delta\psi_{\bar{\sigma}}(\mathbf{x},t) + \ldots],\end{aligned} \tag{3.82}$$

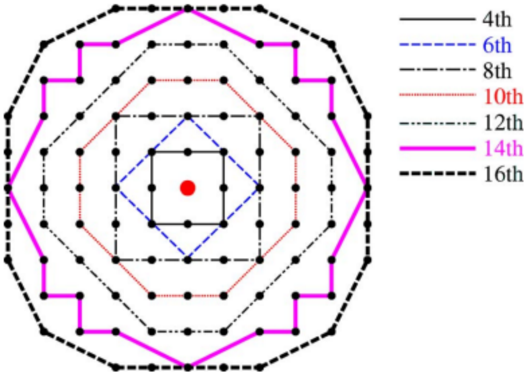

Figure 3.4: 2D illustration of different orders of isotropy in calculating the Shan-Chen force. Reproduced from Ref. [160] with permission of APS.

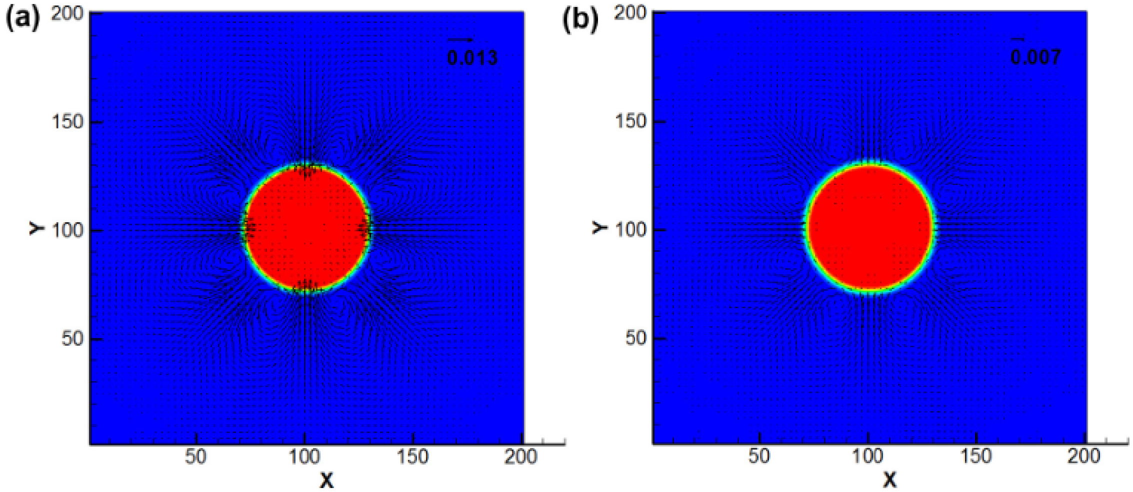

Figure 3.5: Spurious velocity of a steady droplet with isotropic order of (a) 4 and (b) 8. Reproduced from Ref. [165] with permission of Elsevier.

For most of the applications of Shan-Chen model, only the nearest and next-nearest lattice sites are considered in calculating the interaction force, leading to the insufficient isotropy of the discrete gradient operator in Eq. (3.82). The tangential force component gives rise to the spurious current. For a steady droplet, the velocity is expected to be zero everywhere. However, due to the insufficient isotropy of the discrete gradient operator, a small but finite amplitude circulating flow near the interface can be observed when simulating a stationary droplet. A large spurious velocity may lead to numerical instability. As the density ratio increases, the magnitude of spurious velocity also goes up, which limits the maximum density ratio achievable. By expanding the layers of lattice sites used to calculate the Shan-Chen force, higher order of isotropy can be achieved as illustrated in Fig. 3.4, hence decreases the spurious current. Fig. 3.5 shows the spurious velocity of a steady droplet in a vapor phase with different isotropic order of 4 and 8 [165].

The magnitude of spurious velocity decrease with high order of isotropy. Sbragaglia et al. proposed an extended pseudopotential model that allows the use of different equation of state, high grid refinement and high order of isotropy, which significantly reduced the spurious current [160].

3.4.2 Numerical simulation of droplet

Surface tension

For LBM simulation of the droplet interaction with fibers using the Shan-Chen model, one needs to calibrate the interfacial tension and contact angle . Therefore, we performed the Laplace test to study the effect of coupling strength g_{br} on the interfacial tension between the two fluid components. g_{br} determines the interaction strength between two fluid components r and b. Low value of g_{br} causes a low interaction force and thus a more diffuse interface. The simulation were conducted in a square domain of size $240 \times 240 \times 240$ lattice units. Periodic boundary condition is applied to the domain boundaries. Initially, a droplet with a specified radius R_i is placed in the center of computation domain. As described in the previous section, the density ratio in the SCMP Shan-Chen model can be up to $O(10^2)$ when simulating liquid-gas system, while for the MCMP model, the density ratio between the two fluid components is often neglected because it is controlled the coupling strength. Therefore, in our simulation using MCMP Shan-Chen model, the initial density of the two fluid component, ρ_b and ρ_r, is chosen to be $\rho_b = 1$ and $\rho_r = 0$ inside the droplet, and $\rho_r = 1$ and $\rho_b = 0$ outside the droplet. To achieve the desired dynamic viscosity M between fluids, the kinematic viscosity ratio can be tuned to match M, given by[166]

$$M = \frac{\eta_b}{\eta_r} = \frac{\rho_b \nu_b}{\rho_r \nu_r}, \tag{3.83}$$

where η_b and η_r are the dynamic viscosity ratio of components b and r, and ν_b and ν_r are the kinematic viscosity of b and r. Throughout this work, we chose the relaxation time of the two components as $\tau_b = \tau_r = 1.0$, leading to the kinematic viscosity ratio of 1. The simulations are initiated with a sharp interface, where the densities ρ_b and ρ_r change from 1 to 0 across the interface. The pressure difference across the interface $p_c = 2\gamma/R$, where γ is the surface tension and R is the drop radius, is monitored during the simulation until it reaches a steady state. Fig. 3.6 shows the time evolution of capillary pressure p_c and drop radius for droplet with different initial radii. It can be observed that the shrinkage of droplet is larger for smaller droplet due to the diffusion of interface and increase of capillary pressure. For $g_{br} = 0$, the fluid mixture is completely miscible. With increasing g_{br} above a critical value, the two components separate and the interface becomes thinner until the numerical instability occurs due to the increased spurious velocities.

In Fig. 3.7, the density profile of the two fluid components across the interface is shown for three g_{br} values of 0.12, 0.14 and 0.16. The interface layer is where the density changes gradually from 1 to 0. And the exact interface position used for determining the droplet radius R is defined at where the order parameter $\phi = \rho_r - \rho_b = 0$. To measure the droplet radius R, we calculated the order parameter ϕ from ρ_r and ρ_b , and the Euclidean distance R_j from the center of droplet to the position where $\phi = 0$ in the computation domain. The drop radius R is determined as the average of R_j. As shown in the plot, the thickness of interface layer is reduced with increasing g_{br} from around 6 lattice sites to 4 lattice sites.

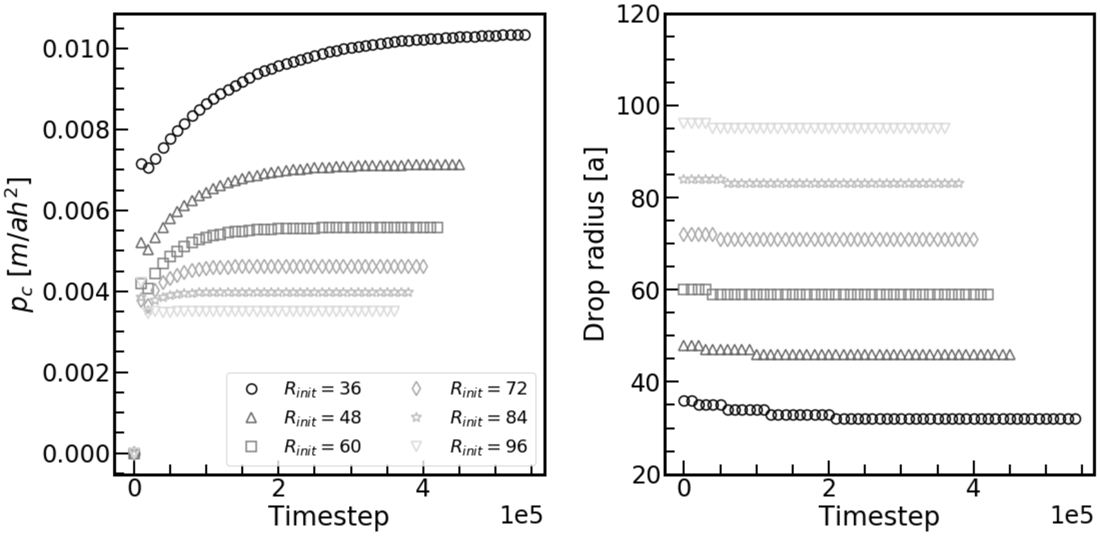

Figure 3.6: Time evolution of capillary pressure p_c and drop radius for droplet with different initial radius in the Laplace test.

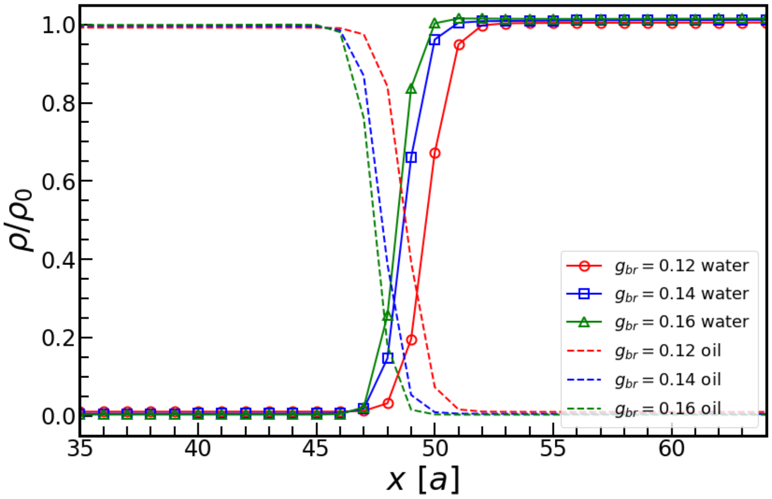

Figure 3.7: Density profile of two fluid components across the interface of a steady droplet along $x-$axis.

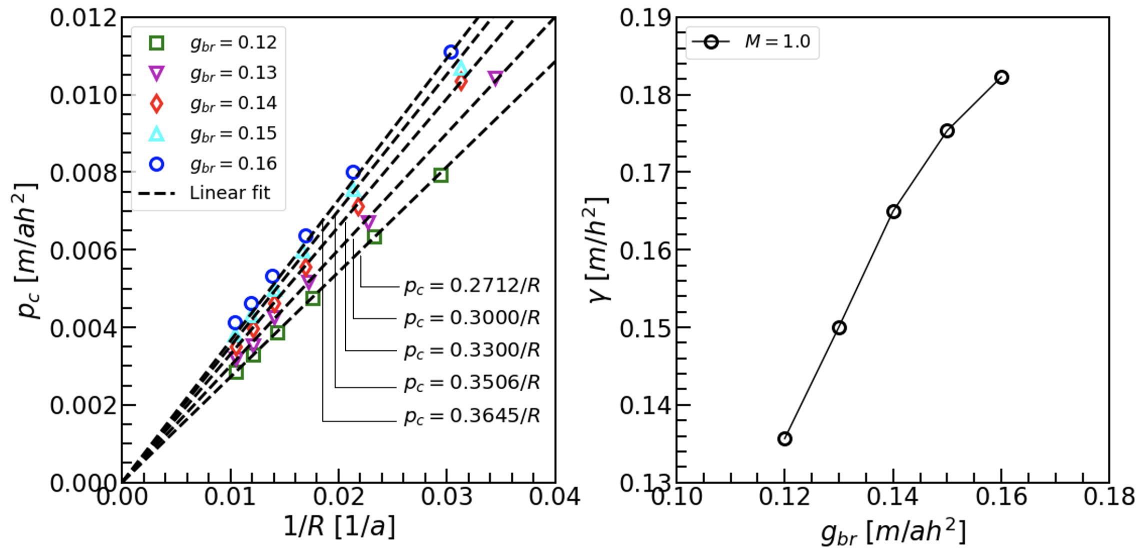

Figure 3.8: Left: pressure difference across the interface is proportional to the inverse of drop radius. Right: surface tension as a function of interaction strength.

Fig. 3.8 shows the linear correlation between pressure difference across the interface and inverse of the droplet radius obtained using the least-square-fit for g_{br} from 0.12 to 0.16. The fitting parameters are shown in Fig. 3.8. This behavior is consistent with Laplace's law. The surface tension is determined from the linear fitting parameter and increases with g_{br}.

Contact angle

In order to study the effect of pseudo wall density of a flat substrate and coupling strength on the resultant contact angle, simulations were conducted in a cubic domain of size $240a \times 240a \times 240a$. A solid wall of 3 lattice sites thick is placed on the bottom plane ($z = 0$). In order to calculate the adhesion force between solid and liquid, the thickness of wall should be at least 2 lattice site. A droplet as a spherical cap is initialized on the solid surface. The wetting condition is completely controlled by the pseudo wall density ρ_{wall}. Negative value of ρ_{wall} leads to contact angle $\theta < 90°$ and positive value of ρ_{wall} gives contact angle

$\theta > 90°$.

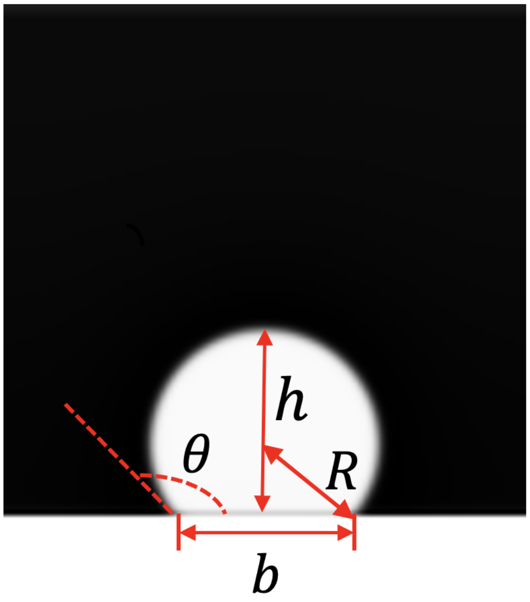

Figure 3.9: Geometric parameters of a sessile drop, h the drop heights, R the drop radius, b the drop base, and θ is contact angle.

Fig. 3.9 shows the cross section of a droplet sitting on hydrophobic surface from LBM simulation, where the contact angle can be measured geometrically via

$$\theta = \pi - \arctan \frac{b/2}{h-R}, \tag{3.84}$$

where the drop radius is given by $R = \frac{4h^2+b^2}{8h}$. The time evolution of drop shape on flat substrate is shown in Fig. 3.10 for $\rho_{\mathrm{wall}} = -0.5$ and 0.5, corresponding to the equilibrium contact angle of 14.3° and 158.2°, respectively. Mid-link bounce back boundary condition is applied on the bottom plane and periodic boundary condition is applied on other domain boundaries. The width of the interface introduces a length scale that can take over the role of the slip length, thus allowing the contact line motion over a no-slip wall through diffusion between two immiscible liquids [167]. The evolution of contact angle is plotted in Fig. 3.11 until it reaches the equilibrium state. In Fig. 3.12, we varied the pseudo wall density from -0.5 to 0.5 at fixed g_{br} = 0.14, and compared the contact angle obtained from geometrical measurement with the analytical expression of Huang's approach in Eq. (3.80). The contact angles calculated from Eq. (3.80) agree well with the measured ones.

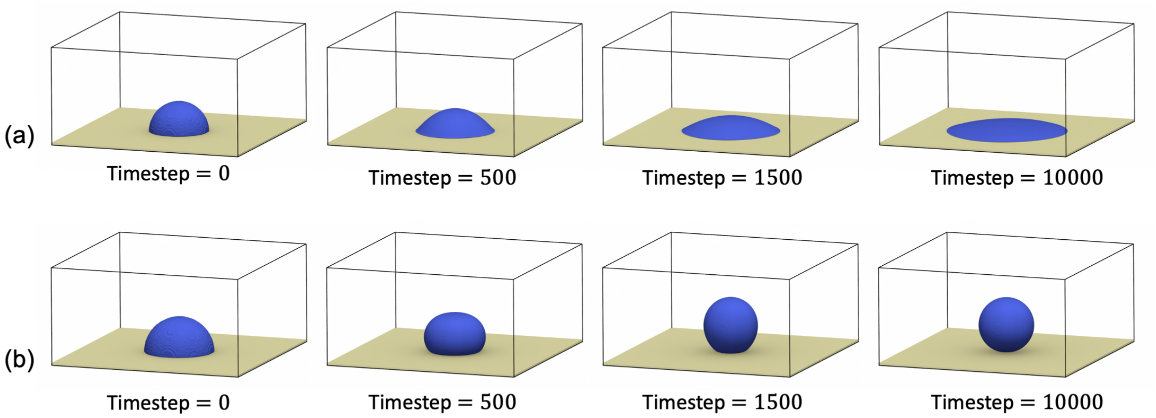

Figure 3.10: Time evolution of droplet shape on the flat substrates with virtual wall density (a) η_{wall} = −0.5 and (b) 0.5.

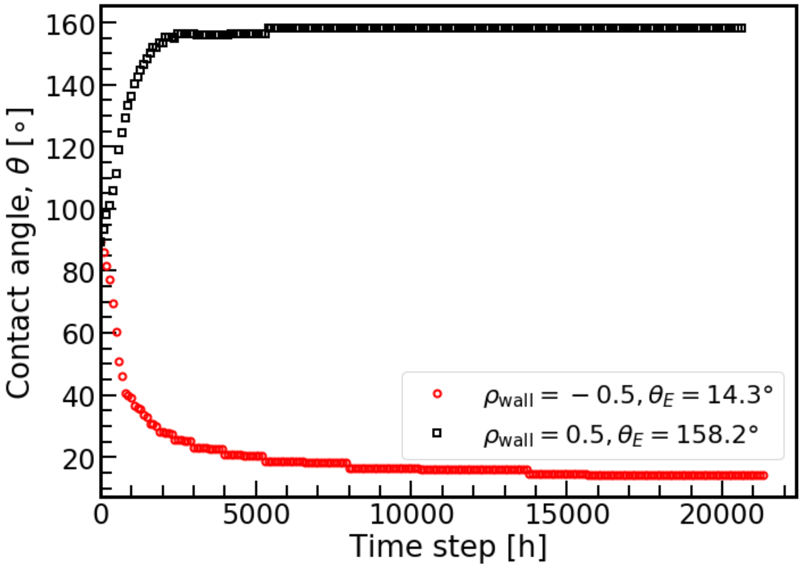

Figure 3.11: Time evolution of contact angle for virtual wall density η_{wall} = −0.5 and 0.5.

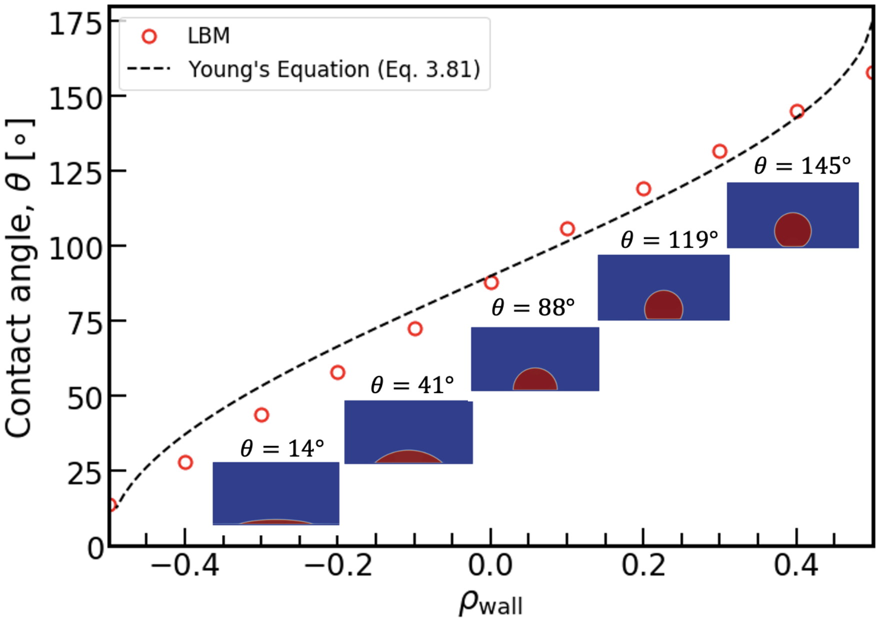

Figure 3.12: The dependency of contact angle on the value of virtual wall density ρ_{wall}

CHAPTER 4

PORE-NETWORK EXTRACTION AND MORPHOLOGICAL ANALYSIS OF FIBROUS MEDIA

4.1 Generation of 3D random fibrous media

In this study, we use computationally generated nonwoven fibrous media with layers of both plywood and randomly oriented fibers [2]. These digital samples are generated to mimic the properties of electrospun fiber membranes [38]. The plywood geometry consists of layers of parallel fibers, where each layer is rotated by 90 degrees around the normal axis. The orientation of the fibers in each layer is thus orthogonal to the orientation in adjacent layers in Fig. 4.1(a). The parameters used for generation of the plywood geometry are the box size L, the radius R_f of the fibers, the distance d between the centerline of the fibers, and the spacing h between the layers. A plywood fibrous geometry is shown in Fig. 4.1(a). The advantage of using ordered fiber arrays is that the flow pattern is periodic so that a clear relationship between normalized permeability and fiber diameter can be obtained [168]. It is worth noting that our plywood geometry with alternating orientation of the fibers differs from the unidirectional regular arrays [66, 169] and isotropic networks [68] that have been considered in the literature. Random fibrous membranes were created with the Digital Material Laboratory Software GeoDict [170]. We used the FiberGeo module of GeoDict to generate nonwoven fibrous membranes with random placement and orientation of fibers. When infinitely long fibers are placed and oriented randomly in each

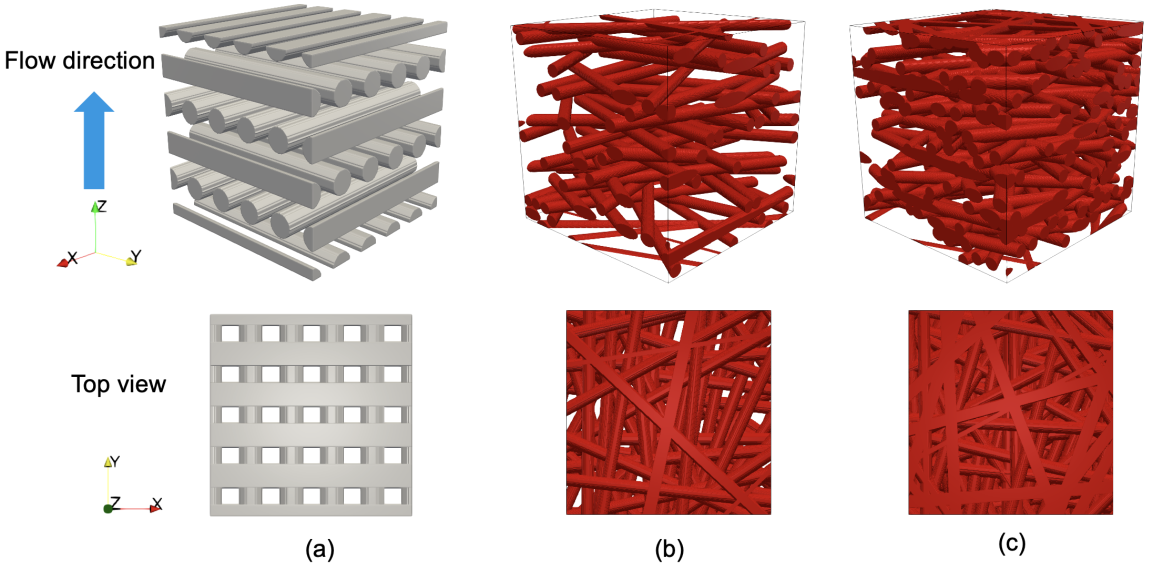

Figure 4.1: Digital representations of fibrous porous media were generated as layered arrangements of fibers with (a) plywood and ((b) and (c)) random in-plane orientation distributions. The geometries with random fiber arrangements were generated with (b) non-overlapping fibers for porosity $\phi \geq 0.7$ and (c) overlapping fibers for lower porosity $\phi < 0.7$. Adapted from Ref. [2] with permission of APS.

plane without constraints, they will typically intersect the other fibers. In this work, we refer to the fiber networks with and without intersections as overlapping and non-overlapping fiber geometries, respectively.

Fiber networks with a well-defined fiber orientation and without fiber overlap can also be created with the FiberGeo module. Structural parameters for the fibers can be defined for different fiber types, including fiber shape and size. Here we used straight cylindrical fibers of varying fiber radius R_f. The global parameters include the domain size, resolution, target Solid Volume Percentage (SVP $= 1 - \phi$, where ϕ is the porosity, SVP $= \frac{\text{Volume of fibers}}{\text{Total volume of cell}}$) and overlap mode. We used a cubic domain of size L and a resolution of $a = 1$ μm. The resolution is defined as the voxel length, $a = L/N$, where N is the number of voxles along each side.

To create laminated anisotropic fibrous media, we set the main axis of the fibers parallel to the xy-plane with a uniform in-plane angle distribution between 0° and 180°. In this case, the fibers lay on the xy-plane and their main axis orientation in relation to the x-direction follows a uniform distribution in the interval $[0°, 180°]$. During the generation phase, the fibers are randomly placed in the domain and oriented randomly in the xy-plane according to the specified distribution, until the target solid volume percentage is reached (stopping criterion). The fibers extend through the entire domain. Therefore, the fiber length depends on its position in the cell and in-plane orientation. The maximum possible length is $\sqrt{2}L$, corresponding to the diagonal of the square $L \times L$. The typical fiber length is on the order of the domain size. The corresponding diameter/length ratios depend on the fiber radius and range from ≈ 0.07 at $R_f = 7a$ to ≈ 0.15 at $R_f = 15a$ in a domain of size $L = 200a$.

To generate the non-overlapping fibrous structures, any existing overlaps are removed after the generation phase. This is accomplished by shifting and rotating the fibers until no overlaps remain. The maximum rotation angle can be specified to make sure the orientation of fibers is slightly out of the xy-plane. The touching of fibers can be allowed. With the non-overlapping mode, it was possible to generate non-overlapping fibrous membranes with porosities down to around 70%. Further decrease of porosity leads to long run-time to shift and rotate the fibers in a large domain.

For smaller values of porosity, the random placement of the fibers becomes excessively time consuming due to the increasing number of constraints. The constraints can be loosened by allowing the fibers to overlap, and we used overlapping fibers to generate fibrous membranes with porosities down to 10%. The overlapping of the fibers may change the characteristics of the pore space, however, we found that this effect appears to be negligible. In our generated geometries, the fibers are randomly oriented but straight, leading to nonwoven structures in contrast to the fiber webs considered by Koponen et al. [56]. The random fibrous structures created here model fibrous membranes produced by melt-blowing or electrospinning processes [38]. Two examples of random fiber arrangements without and with overlaps are shown in Fig. 4.1(b) and (c).

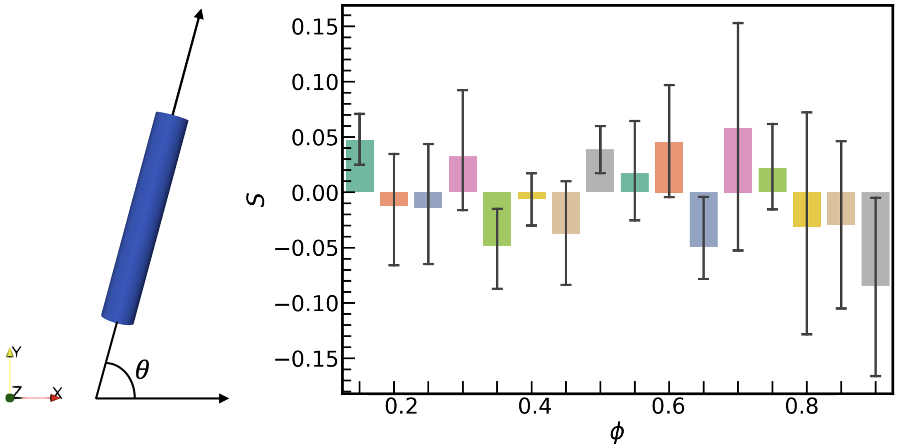

(a) (b)

Figure 4.2: (a) Schematic illustration of fiber orientation angle θ. (b) Nematic order parameter S of the generated random fiber geometries.

To quantify the anisotropy and fiber orientation in the generated plywood and random fiber mats, we employ the 2D nematic order parameter S, defined as,

$$S = \langle \cos(2\theta) \rangle, \tag{4.1}$$

where θ is fiber orientation with respect to $x-$direction, $\theta \in [0, \pi)$, as illustrated in Fig. 4.2(a). The brackets denote the average over all fibers. For a unidirectional fiber mat along $x-$direction, the order parameter is 1. If the fiber angle distribution is uniform, the corresponding nematic order parameter is zero. For the random fiber mats, it can been in Fig. 4.2(b) that the order parameter fluctuates around zero due to the specified uniform distribution of fiber orientation. The small deviation can be attributed to the limited number of fibers.

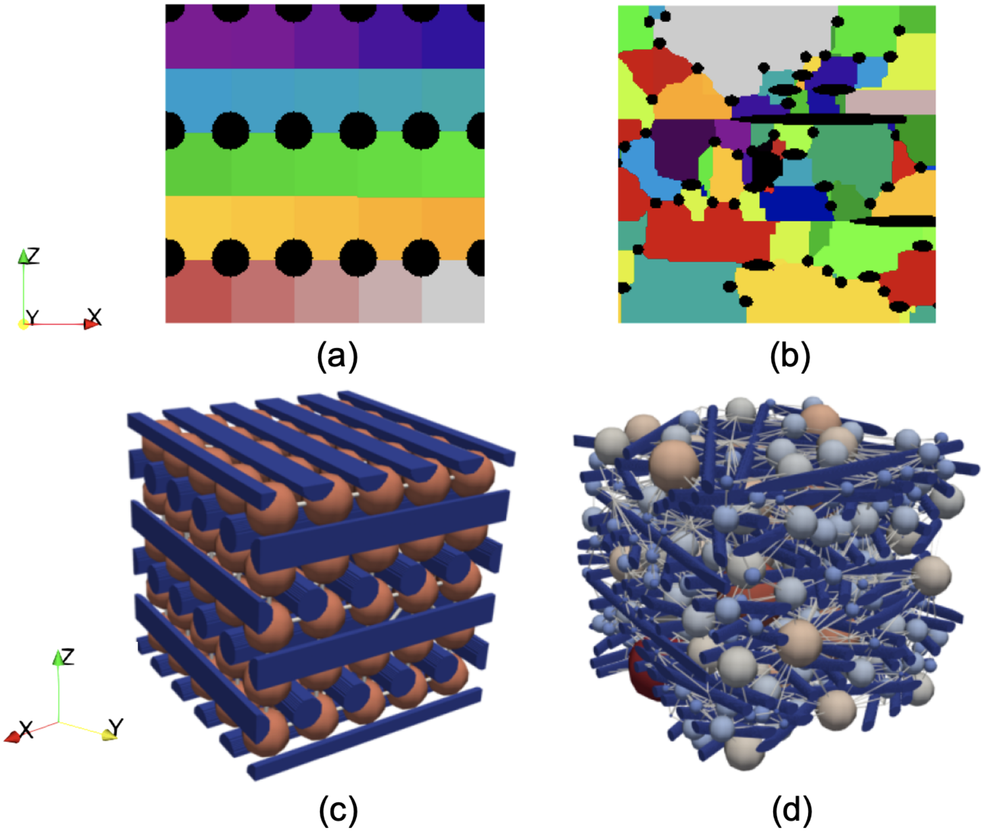

Figure 4.3: Segmented pore space ((a) and (b)) and pore network representation ((c) and (d)) of fibrous porous media. The colored regions in (a) and (b) indicate the SNOW basins corresponding to each retained peak in the local distance transform. Each basin is assigned an integer value represented by a different color. The pore networks in (c) and (d) represent the inscribed spheres of the basins as pores that are connected by throat channels. The colors of the spheres represent the size of the pores. The ordered fiber arrangements ((a) and (c)) yield a plywood periodic pore network whereas the random fiber arrangements ((b) and (d)) yield a complex pore network. Reproduced from Ref. [2] with permission of APS.

4.2 Pore space segmentation and microstructure analysis

We use the subnetwork of the over-segmented watershed (SNOW) algorithm from the OpenPNM package [171] to extract the pore network from both plywood and random fibrous geometries. A Gaussian blur filter was applied to the distance transform, where a standard deviation of 0.35 was chosen for the convolution kernel. The Gaussian blur filter is a measure of similarity between two position $\mathbf{x}$ and $\mathbf{x}'$. It evalues to 1 if the $\mathbf{x}$ and $\mathbf{x}'$ are identical, and approaches 0 as $\mathbf{x}$ and $\mathbf{x}'$ move further apart. It can be defined as

$$K(\mathbf{x},\mathbf{x}') = \exp\left(-\frac{||\mathbf{x}-\mathbf{x}'||^2}{2\sigma^2}\right), \tag{4.2}$$

where $||\mathbf{x}-\mathbf{x}'||$ is the Euclidean distance between $\mathbf{x}$ and $\mathbf{x}'$, and σ is the standard deviation of the Gaussian distribution. The Gaussian blur filter is applied to remove the extra peaks in the distance map [171]. Subsequently, a spherical maximum filter with a radius of 4 was applied. The maximum filter replaces each voxel value of the image with the maximum value of its neighbor voxels window, i.e., $\mathrm{dst}(\mathbf{x}) = \max(\mathrm{src}(\mathbf{x}'))$, where dst is the output image, src is the input image, and $\mathbf{x}'$ is the points in a spherical element with radius of R and centered at $\mathbf{x}$. When R is too small, many spurious maxima are found. If R is too large, some maxima are missed.

The result of the watershed segmentation of the pore space and the pore-networks extracted with SNOW are shown in Fig. 4.3. The local maxima in the distance map are passed as markers to the marker-based watershed algorithm, which finds the basins of the distance map, yielding the segmentation of each pore region as shown in Fig. 4.3(a) and (b). Fig. 4.3(a) and (b) shows the cross section of segmented pore space perpendicular to $y-$direction. Each pore region is represented by different colors. The overlaid structure of plywood and random fiber arrangements with the SNOW extracted pore-network can be seen in Fig. 4.3(c) and (d). Fig. 4.4(a) and (b) compare the stick-and-ball representation of SNOW pore networks of plywood and random fibrous materials in a cubic domain of size $L = 200a$. The pore networks of different porosities ϕ in a cubic domain of size $L = 400a$ are shown in Fig. 4.4(c)-(d).

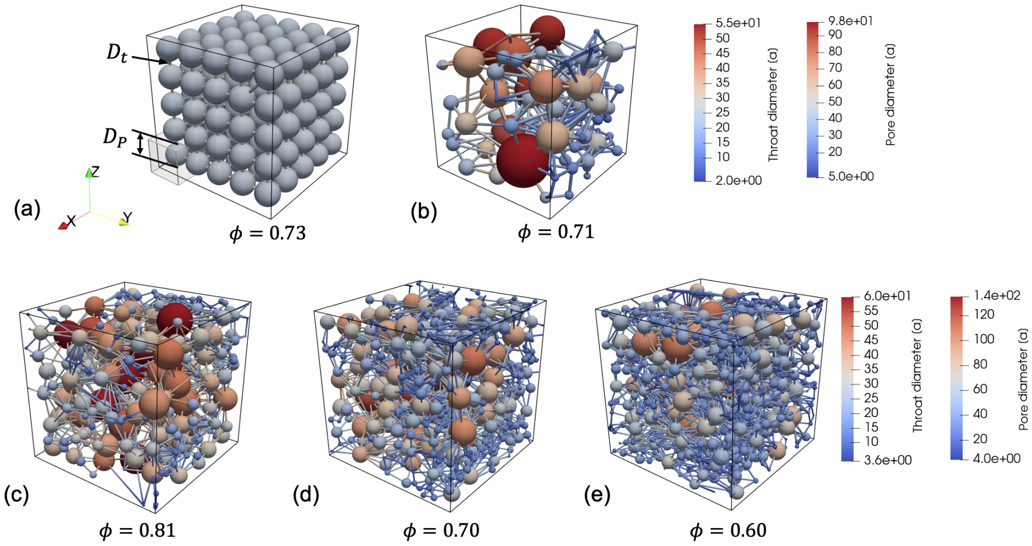

Figure 4.4: The stick and ball representation of the SNOW network of (a) plywood and (b) random fibrous materials in a cubic domain of size $L = 200a$. The pore networks of porosity (a) $\phi = 0.81$ (b) $\phi = 0.70$ and (c) $\phi = 0.60$ in a cubic domain of size $L = 400a$.

From the pore network representation, we obtain the distribution of pore diameters D_p, throat diameters D_t and lengths L_t, and coordination numbers n_c. D_p and D_t is illustrated in a unit cell of pore-throat in Fig. 4.5. The length of throat L_t is defined by the Euclidean distance between the centroids of two pores minus the radius of each neighboring pore. The coordination number n_c is defined as the number of pores connected each individual pore. In addition, we estimate the specific surface area S_0 of the fibers from the pore and throat areas. The specific surface area is defined as $S_0 = A_{\text{surf}}/V_{\text{solid}}$, where A_{surf} is the surface area of pore region and V_{solid} is the solid volume. It can be estimated in the SNOW algorithm by assuming pore bodies as spheres, then subtracts the areas of neighboring throats, namely,

$A_{\text{surf}} = \sum_i (4\pi R_{i,p}^2 - \sum_j \pi R_{j,t}^2)$, where $R_{i,p}$ is the radius of pore i, and $R_{j,t}$ is the radius of neighboring throat j. For the plywood geometries, A_{surf} can be calculated directly from the surface area of fibers as $A_{\text{surf}} = 2\pi R_f L N$, where R_f is the fiber radius, L the domain size and N the number of cylindrical fibers. The pore network of the plywood geometries also served as a validation of the estimate for S_0 by comparing with analytical calculations in section 4.3.

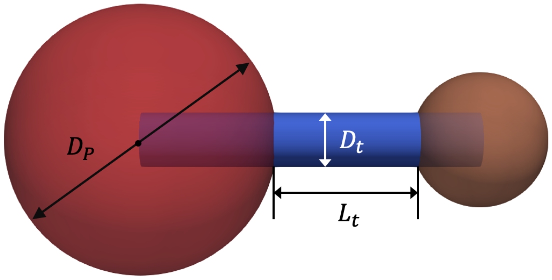

Figure 4.5: Unit cell of pore-throat.

Nonwoven fibrous media were computationally generated using layered arrangements with plywood and random fiber orientations, as explained in section 4.1. An example of a plywood fibrous geometry is shown in Fig. 4.1(a). Random fibrous media were generated with GeoDict using the same fiber radius and a random fiber orientation distribution within each layer of the sample. In the porosity range $0.7 \leq \phi \leq 0.9$ we used both the non-overlapping and overlapping mode in FiberGeo to investigate the effect of overlapping arrangements on the morphological and transport properties. Two examples of random fiber arrangements with and without overlaps, respectively, are shown in Fig. 4.1(b) and (c). The SNOW algorithm available in OpenPNM [171] was employed to extract the pore network from the generated fibrous media as shown in Fig. 4.3. We analyze the statistical distributions obtained from the pore-network and compare them to theoretical models for layered fibrous media (see Appendix A).

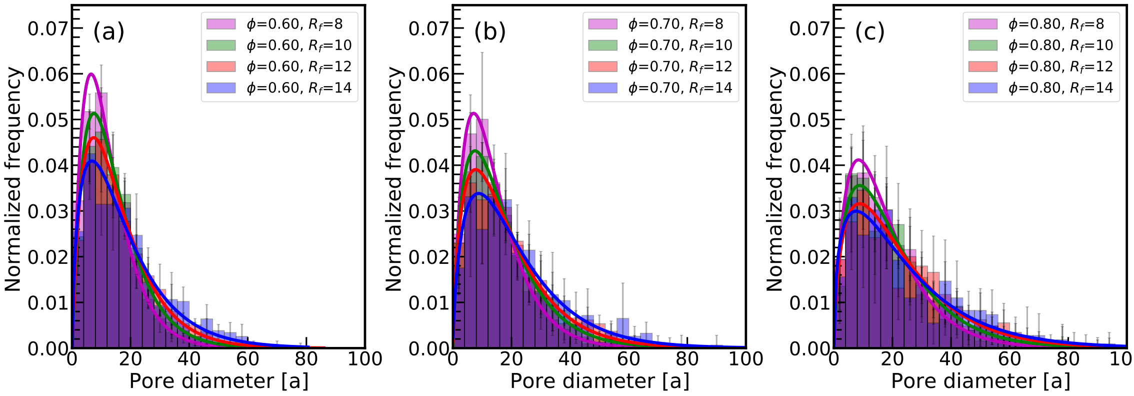

Figure 4.6: Dependence of the pore size distribution on the fiber radius for porosities of ϕ = 0.60 (a), ϕ = 0.70 (b), and ϕ = 0.80 (c). Solid lines represent a gamma distribution fitted to the histograms. The peak of the pore size distribution decreases with increasing fiber radius while the width of the distributions slightly widens. Reproduced from Ref. [2] with permission of APS.

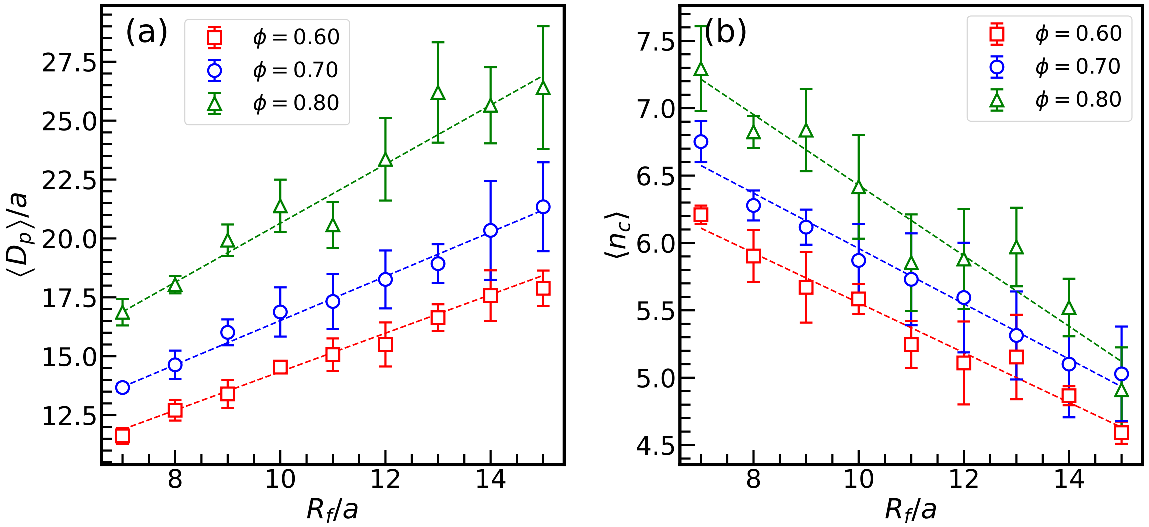

Figure 4.7: Influence of the fiber radius on the mean pore size (a) and the mean connectivity (b) for different porosities. The dashed lines represent linear fits to the data. The mean pore diameter increases linearly with the fiber radius while the connectivity decreases. Reproduced from Ref. [2] with permission of APS.

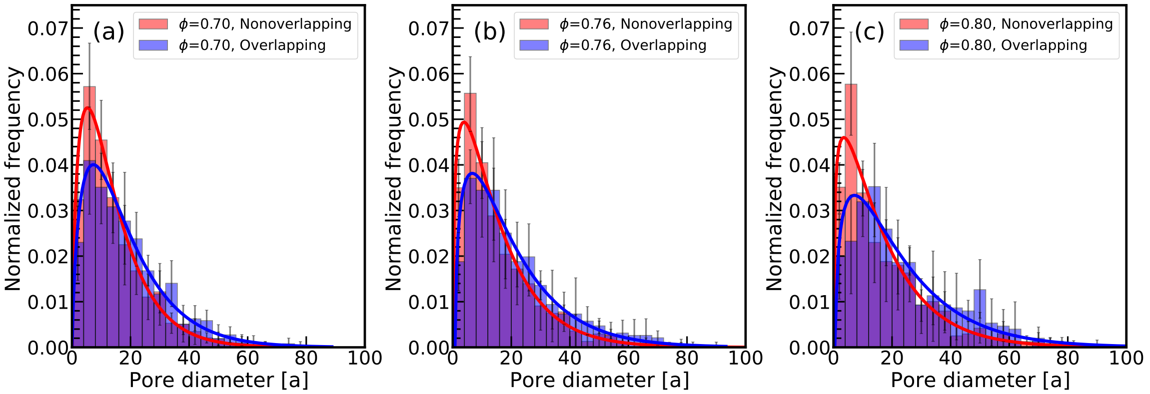

Figure 4.8: Effect of fiber overlapping on the pore size distribution in fibrous media with porosities ϕ = 0.70 (a), ϕ = 0.76 (b), and ϕ = 0.80 (c). Solid lines represent a gamma distribution fitted to the histograms. The number of small pores is reduced in geometries with overlapping fibers. Reproduced from Ref. [2] with permission of APS.

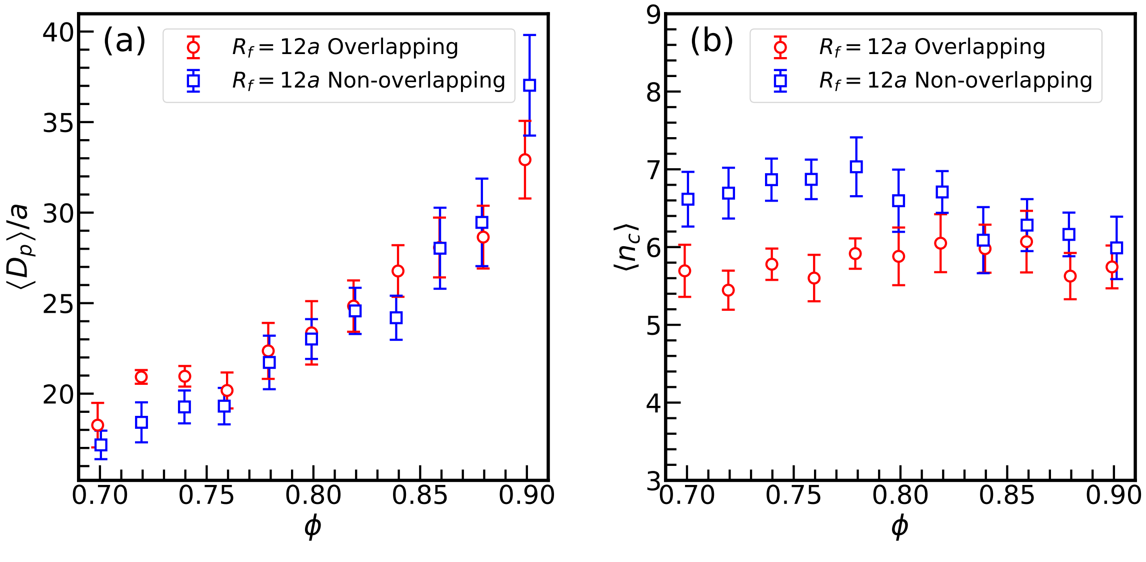

Figure 4.9: Influence of fiber overlapping on the mean pore diameter (a) and mean connectivity (b) for porosities in the range 0.70 ≤ ϕ ≤ 0.90. Reproduced from Ref. [2] with permission of APS.

4.2.1 Dependence on fiber radius and overlap

For real fibrous membranes, it is important to understand the impact of manufacturing parameters on the pore space morphology. Among the controllable factors are the fiber structural characteristics such as fiber diameter and fiber shape, and the amount of overlapping that results from the manufacturing process. Therefore, we generated random fibrous media using different fiber radius between $R_f = 7a$ and $R_f = 15a$ and the possibility of overlapping, as described in section 4.1.

The dependence of the pore size distribution on the fiber radius is shown in Fig. 4.6 for three different porosities. The histograms show that the frequency of smaller pores decreases with increasing fiber diameter, while the distribution broadens. Therefore, the mean pore diameter increases with increasing fiber diameter. The dependence of the mean pore diameter on the fiber radius is shown in Fig. 4.7. The mean pore diameter follows a linear increase with similar slope for the considered porosities. Conversely, the mean connectivity decreases as the fiber radius increases, which indicates that the complexity of the pore network is reduced.

The effect of allowing the fibers in the random arrangements to overlap is shown in Fig. 4.8 for three different porosities. For non-overlapping arrangements, the fibers are placed more homogeneously throughout the medium, leading to a narrower distribution of pore sizes. Vice-versa, the pore size distribution broadens for overlapping arrangements.As shown in Fig. 4.9, the mean connectivity of overlapping fiber arrangements is slightly lower than that of non-overlapping fiber structures for porosities $\lesssim 0.82$. However, the mean connectivity is comparable at higher porosity, and the overlapping has no pronounced effect on the mean pore size. We thus expect that the non-overlapping and overlapping fiber arrangements have similar effective properties.

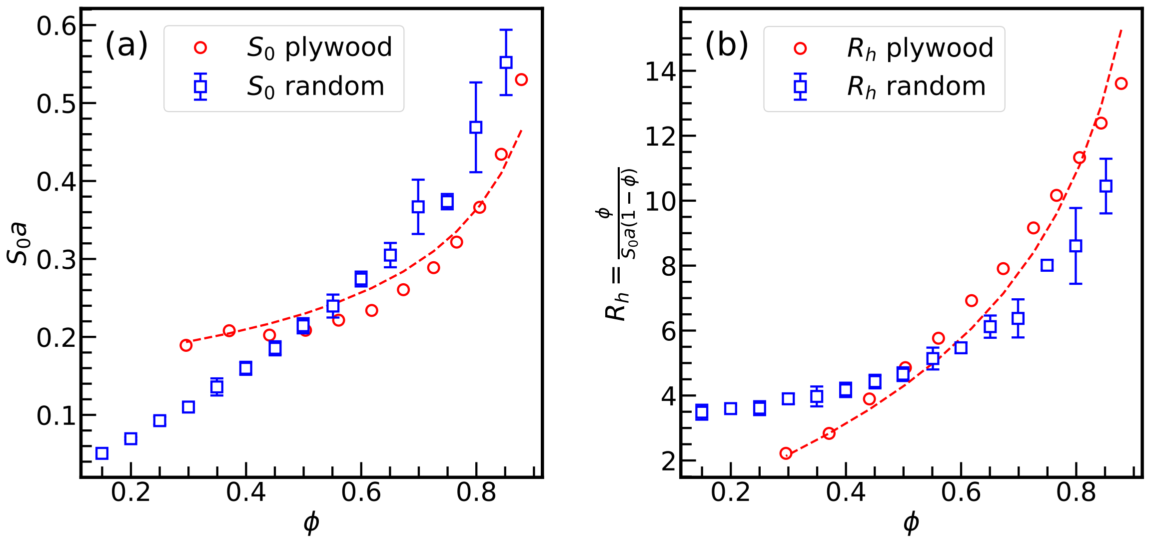

Figure 4.10: Dependence of specific surface area (a) and geometric hydraulic radius (b) on the porosity for plywood and random fibrous media. The dashed lines represent analytical predictions for plywood fiber arrangements. Reproduced from Ref. [2] with permission of APS.

4.3 Effective geometric pore space properties

The first step in connecting macroscopic properties of porous media to their microscopic morphology is the calculation of effective pore space properties. Here, it is of particular interest how the properties vary between plywood and random fiber arrangements. Two important geometric properties of porous media are the specific surface area $S_0 = A_p/V_{\text{solid}}$ and the hydraulic radius $R_h = V_p/A_p$, where A_p is the surface area of the pore space, and V_{solid} and V_p are the solid volume and the pore volume, respectively. The hydraulic radius can be expressed in terms of specific surface area and porosity as $R_h = \phi/(S_0(1-\phi))$. The specific surface area can be calculated from the pore-network extracted with the SNOW algorithm. The pores are assumed to be spherical and their interfacial area is calculated by subtracting the cross-sectional area of the connected throats. The throat surface areas are calculated for arbitrary shape by integrating the throat perimeter along the length, which is more accurate than assuming straight cylinders. The total surface area of the pores and throats is divided by the total volume of the fibers to give S_0. The pore-network based calculation of the specific surface area was used for both non-overlapping and overlapping fiber arrangements. For the plywood fiber arrangements, where all fibers have the same length and no overlaps, the specific surface area $S_0 = 2/R_f$ is controlled by the fiber radius $R_f = L\sqrt{(1-\phi)/(\pi N_f)}$, and the hydraulic radius is thus expected to scale with the porosity as $R_h \propto \phi/\sqrt{(1-\phi)}$.

Fig. 4.10(a) shows the specific surface area of the fibrous media as a function of porosity, which is commonly considered the main determining factor of macroscopic properties. For the plywood geometries, the values calculated from the pore-networks are in good agreement with the theoretical scaling, as shown by the dashed lines. This indicates that the pore network yields a good approximation of the surface area and volume of the pore space in spite of the assumption of spherical pores and tube-like throats. For random fiber arrangements, the calculated values for the specific surface area and hydraulic radius deviate from the plywood geometries scaling because the exposed surface area of the fibers varies due to random orientation and overlaps. This reflects the more complex structure of the pore space where the geometric properties are affected by the size distribution of pores and throats. We compared the specific surface area of the random fibrous media to the values obtained in Ref. [56] for samples of foam- and water-deposited pulp sheets, which were calculated using a marching-cube algorithm. For pulp sheets with porosities between 82% and 91%, the reported values of the specific surface area S_0 range from 0.52 to 0.67. These values are in good agreement with the specific surface areas $S_0 = 0.46 - 0.70$ for our generated fibrous media, which indicates that our approach generates representative samples of realistic fibrous membranes.

The differences between plywood and random fiber arrangements suggests to investigate the dependence of the effective geometric properties on the microstructure of the

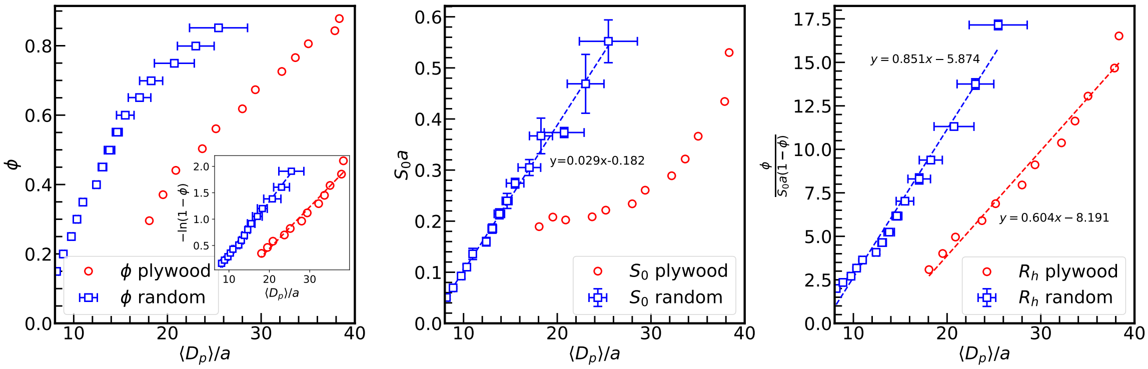

Figure 4.11: Dependence of porosity (a), specific surface area (b), and geometric hydraulic radius (c) on the mean pore size in plywood and random fibrous media. The dashed lines represent linear fits to the data. Adapted from Ref. [2] with permission of APS.

pore space and the statistical pore size distribution. Fig. 4.11 shows the dependence of the porosity, specific surface area, hydraulic radius, and constriction factor on the mean pore size of plywood and random fibrous media. The porosity increases with pore size approaching $\phi = 1.0$ asymptotically. As shown in the inset of Fig. 4.11(a), the increase is well described by a logarithmic scaling $-\ln(1-\phi) \propto \langle D_p \rangle$. This is an interesting observation as it suggests that any quantity depending logarithmically on the porosity will scale linearly with the mean pore size $\langle D_p \rangle$. Such logarithmic relations have been proposed for the tortuosity of porous media [172, 173].

As observed before, the specific surface area in Fig. 4.11(b) shows a marked difference between plywood and random fiber arrangements. While the plywood geometries exhibit a superlinear increase with the pore size, the specific surface area of the random geometries appears to increase linearly with the mean pore size. This is intriguing since the fiber surface area scales with R_f^2 which was shown to be linearly related to the mean pore size squared, cf. Fig. 4.7(a). It suggests that only a fraction of the fiber surface area is exposed to the pore space, while the remaining area represents contacts between fibers. These contacts are a result of the layering of the fibers in the non-woven structure, where each fiber belongs to a layer with random fiber orientations within the layer, such that the fibers lay across fibers in the adjacent layers thereby reducing the pore-exposed fiber surface.

The plot in Fig. 4.11(c) shows the dependence of the geometric hydraulic radius on the mean pore size. The hydraulic radius $R_h = \phi/(S_0(1-\phi))$ combines the influence of the mean pore size on the porosity and the specific surface area. From the observation $\ln(1-\phi) \sim -p\langle D_p \rangle$ with a small coefficient p, we expect $\phi \sim p\langle D_p \rangle$ and $R_h \sim p\langle D_p \rangle / \sqrt{1 - p\langle D_p \rangle}$. To leading order in $p\langle D_p \rangle$, we hence expect a linear scaling between R_h and $\langle D_p \rangle$ for both plywood and random fiber arrangements. This is confirmed by the dashed lines in Fig. 4.11(c) that represent a linear fit to the data. The linear correlation between the hydraulic radius and the mean pore size establishes a link between effective pore space properties and the statistical mean of the pore size distribution. This opens up possibilities to express macroscopic transport properties of porous media in terms of statistical properties of the pore space. For example, it will enable us to quantify the influence of pore space microstructure on the permeability and tortuosity of porous media, where the mean pore size corresponds to a characteristic hydraulic length in lieu of the hydraulic radius. A detailed investigation of microstructure effects on fluid transport in plywood and random fibrous media will be reported elsewhere.

4.4 Conclusions

We have presented a computational framework for characterizing the microstructure of nonwoven fibrous media by means of statistical analysis of the pore space properties obtained from segmented pore networks. Randomly generated three-dimensional fiber arrangements served as realistic models of fibrous porous membranes. We utilized a watershed segmentation algorithm [77, 78, 171, 81] to extract pore-networks from both ordered and disordered fibrous media.

The nonwoven fibrous media considered in this work were generated with the Fiber-

Geo module of the GeoDict software [170]. Using the solid volume fraction as a stopping criterion, we were able to generate random fiber arrangements with a prescribed porosity down to 70%. To generate fibrous media with lower porosity, it was necessary to allow the fibers to overlap. While this may in principle affect the geometric characteristics of the pore space, we found that it did not have a significant effect on the properties we analyzed. The nonwoven fiber networks are representative for fibrous membranes produced by melt-blowing or electrospinning [174, 175, 176, 38, 177, 178, 179, 180] and are different from, e.g., the fiber webs considered by Koponen et al. [181]. We only generated systems with straight fibers and a monodisperse fiber radius. Electrospinning and melt-blowing are applicable to a wide range of fiber materials, and in some cases such as polymeric submicron fibers the flexibility of the fibers may affect the structure and properties of nonwoven mats. Silberstein et al. [182] characterized fiber mats electrospun from amorphous polyamide and reported that fibers of submicron diameter tend to deviate increasingly from being straight and rod-like with decreasing diameter. The relatively low bending stiffness of fibers is an important feature for mechanical deformation of fiber mats under load. For a combination of sol-gel processing and electrospinning of ceramic fibers, Chen et al. [38] observed that almost straight cylindrical fibers can be produced at low relative humidity (30%), whereas the fiber shape deviated from straight cylindrical shape at high relative humidity levels (50%).

Pourdeyhimi et al. [183] have presented an algorithm to generate nonwoven structures in which the fibers may bend around contact points with other fibers. This algorithm could in principle be used to generate fibrous media with curved fibers, however the pore-space characterization of such media is beyond the scope of the current work. While the results of our study only apply to straight fibers, the general framework can be extended to include fibrous media with polydisperse fiber diameters or other specific features relevant to manufacturing processes for fibrous membranes.

For the morphological analysis of the generated structures, we employed the SNOW algorithm implemented in the OpenPNM package, which uses a watershed segmentation of the local distance transform to extract the pore network [171]. By analyzing the standard deviation of the mean properties of 27 samples, we ensured that the size of the generated geometries is sufficiently large to capture the representative volume element (RVE) [54, 184]. We compared the cumulative distribution of pore sizes to theoretical models based on gamma distribution [74, 73, 69], and found that it is important to take into account the non-uniform fiber orientation distribution to accurately predict the cumulative pore size distribution. At higher porosity, the theoretical model underpredicts the frequency of small pores which limits the accuracy of macroscopic transport properties predicted from these models. It is worth noting that the identification of pores and throats in the segmented pore space is prone to ambiguity, which may affect the results of the morphological analysis. Alternative algorithms to extract the pore network from the segmentation could be explored to investigate the impact of specific definitions of pore and throat sizes based on the local distance transform of the pore space [171].

We further investigated the influence of the mean pore size on effective pore space properties such as porosity, specific surface area, and geometric hydraulic radius. The dependence reveals the differences between random and plywood fiber arrangements, leading to a different scaling of these properties as a function of porosity, which is often used to establish phenomenological relationships for porous media. For prediction of macroscopic properties of fibrous media, it is thus important to characterize the microstructure of the pore space in terms of statistical properties.

In conclusion, the statistical analysis of pore network properties of nonwoven fibrous media provides insights into the dependence of morphological variation on characteristic parameters such as fiber radius and overlapping. The finding that the effective properties show a dependence on the mean pore size that is different between plywood and random fiber arrangements indicates that the randomness on the microscopic level can have a significant effect on macroscopic properties of porous media and their scaling behavior. Determining the statistical distribution of pores and throats in the pore network and their sizes enables us to connect the macroscopic properties to pore-scale features of specific fibrous samples. While we have used computationally generated fibrous porous media, the segmentation approach is applicable to microstructure representations of real porous media that can be obtained using experimental imaging techniques such as X-ray computed tomography or scanning electron microscopy. Our framework thus provides a basis for predicting effective properties from real microstructure images. In addition, the insights into the influence of experimentally controllable parameters, such as the fiber radius and orientation, can aid in adjusting manufacturing processes for fibrous membranes with tailored properties for filtration and separation applications.

The data and code used to generate the figures in this chapter can be accessed and executed through Code Ocean [185].

CHAPTER 5

MICROSTRUCTURE EFFECTS ON TRANSPORT PROPERTIES OF FIBROUS MEDIA

We performed the lattice Boltzmann simulations of single-phase fluid flow through the fibrous porous media to study the steady-state velocity field $\mathbf{u}(\mathbf{x})$ in the pore space for varying applied pressure gradient $\partial p/\partial z$ [3].

The D3Q19 model with 19 discrete velocities $\mathbf{c}_i$ and the lattice speed of sound $c_s = \frac{1}{\sqrt{3}}\frac{a}{h}$ is employed in this work, where a is the lattice unit for length, and h is the time unit in LBM. A common choice for the collision matrix of the D3Q19 lattice is $\mathrm{diag}\{\gamma_k\} = \mathrm{diag}(0, \gamma_b, 1.4, 0, 1.2, 0, 1.2, 0, 1.2, \gamma_s, 1.4, \gamma_s, 1.4, \gamma_s, \gamma_s, \gamma_s, 1.98, 1.98, 1.98)$, where γ_b controls the bulk viscosity [139]. This D3Q19-MRT model is implemented in the parallel lattice Boltzmann code LB3D [186]. LB3D allows to load complex geometries from a file containing information about the location of solid and fluid sites on the lattice. Within the lattice Boltzmann method, the lattice links that are intersected by the solid surface must be handled by boundary conditions. Here, we used the standard bounce back (SBB) scheme that realizes a no-slip boundary condition with the first order accuracy. To reduce viscosity-dependent boundary effects [140], we used a multi-relaxation time collision operator with $\gamma_s = 1/(0.8h)$ and $\gamma_{\mathrm{bulk}} = 1/(0.84h)$. This choice follows a calibration study by Narvaez et al. [187, 188], where the relative error of measured permeability was evaluated, and the choice of relaxation parameters was shown to produce very accurate results for Poiseuille flow in circular, quadratic, and triangular pipes. To simulate a pressure driven flow through porous media, we employed on-site pressure boundary conditions [143] by setting the mass densities at the inlet and outlet to ρ_{in} and ρ_{out}, respectively. The fluid density in the pore space is initialized with a linear gradient by interpolating ρ_{in} and ρ_{out}. These densities are kept fixed at the inlet and outlet during the simulation to impose the pressure gradient $\partial p/\partial z$. The different density at inlet and outlet is applied to provide a pressure gradient and driving force of the flow, as described in Section. 3.3.3 using the pressure boundary condition. The total fluid density is measured during simulation to make sure mass conservation. We also calculated the Mach number of the flow by $Ma = u_{\text{max}}/c_s < 0.1$ to satisfy the incompressible fluid constraint. The coordinate axes were chosen such that the flow is driven in the z direction. Since a random porous geometry is not compatible with periodic boundary conditions, the four sides of the simulation parallel to the flow are enclosed with solid boundaries. This effectively encloses the porous medium in a square channel, which enables us to use the permeability of an empty channel as a reference value.

To load the generated geometries into LB3D, the output files from GeoDict were converted to ASCII files containing the coordinates of solid voxels using an in-house Python script. The voxelized fiber geometries were loaded into a cubic lattice domain of L^3 lattice sites. All simulations were run until the system reached a steady state,where convergence was assumed when the relative change of the mass flux m_z in the direction of the pressure gradient fell below 10^{-5} between measurements recorded every 1000 timesteps, i.e., $|1 - m_z(t)/m_z(t - 1000h)| < 10^{-5}$. The simulations were carried out on Clemson University's Palmetto cluster using 4 computer nodes, each with 16 Intel Xeon E5-26xx CPU cores. The elapsed real time to reach steady state depends on the porosity and was in the range 8-30 hours. The data and code used to generate the figures in this chapter can be accessed and executed through Code Ocean [185].

5.1 Code validation

The simulation setup was first validated by considering the classic flow through an empty square channel. A single phase flow is modeled in a square channel of size $200 \times 200 \times 200$ lattices, shown as the schematics in Fig. 5.1(a). Mid-link bounce back boundary condition is applied to the channel walls. The general solution of fully developed flow in a $b \times b$ square channel is given by [189, 143]:

$$u_z(x,y) = u_0 \left[1 - (\frac{y}{b})^2 + 4 \sum_{k=1}^{\infty} \frac{(-1)^k}{a_k^3} \frac{\cosh(\frac{a_k x}{b})}{\cosh(a_k)} \cos(\frac{a_k y}{b}) \right], \tag{5.1}$$

where $u_0 = \frac{(2b)^2 \Delta p}{8 \eta L}$, $\alpha_k = (2k-1)\pi/2$, k=1,2,..., η is the dynamic viscosity, Δp is the pressure difference, and L is the length of the channel. The steady-state flow profile was compared to the analytical solution in Fig.5.2. Here, the infinite sum in Eq. (5.1) is truncated at 100 terms and compared to the numerical results for the velocity profile along $x-$axis at $y = L/8, L/4$ and $L/2$. The velocity field in steady state obtained from LB simulation is shown in Fig. 5.1(b). We find excellent agreement between numerical results and analytical solution in Fig. 5.2.

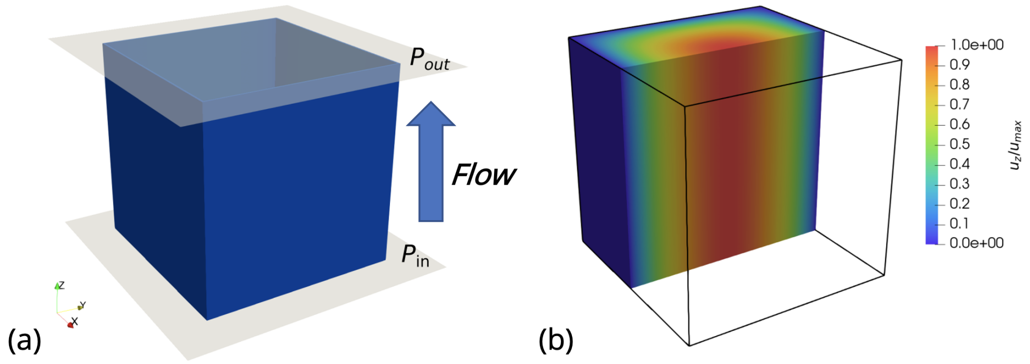

Figure 5.1: (a) Schematics of single phase flow through a square channel. (b) The cross section of velocity field in steady state.

In the lattice Boltzmann simulations, we determined the trans-plane permeability κ

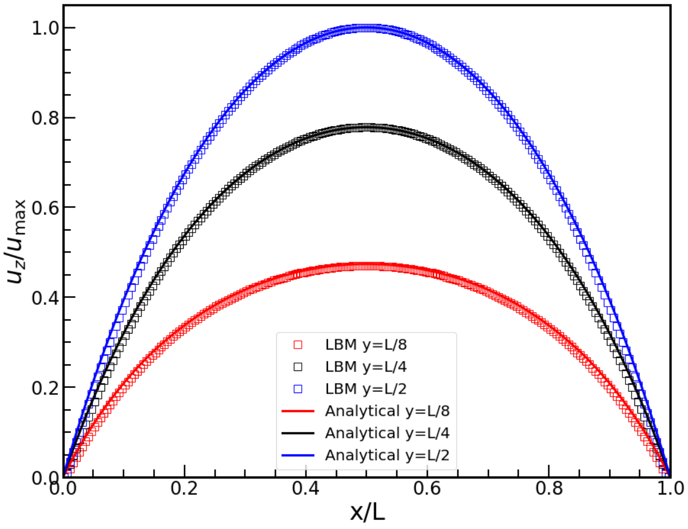

Figure 5.2: Velocity profile in a square channel as a function of the position along x-axis at $y = L/8, L/4$ and $L/2$.

based on Darcy's law Eq. (1.3) by using the mass flux $m_z = \rho \langle u_z \rangle$ measured in simulations

$$q = \langle u_z \rangle = -\frac{\kappa}{\eta} \frac{\Delta p}{L}. \tag{5.2}$$

where $\langle u_z \rangle$ is the averaged velocity, and the pressure gradient is determined from the density difference between inlet and outlet $\Delta p/L = c_s^2 \Delta\rho/L$. Thus, the trans-plane permeability κ is given by:

$$\kappa = -\eta \frac{q}{\frac{\partial p}{\partial z}} = \left(\frac{1}{\gamma_s} - \frac{h}{2} \right) \frac{m_z L}{\Delta\rho}, \tag{5.3}$$

where m_z is the mass flux in the direction of the pressure gradient, $\Delta\rho = \rho_{\mathrm{in}} - \rho_{\mathrm{out}}$, L is the sample thickness, and $\eta = \rho c_s^2 (\frac{1}{\gamma_s} - \frac{1}{2})$ is the dynamic viscosity. The measured flow rate q shows the expected linear dependence on the applied pressure gradient Δp. There exists an analytical expression for the permeability of a square channel with cross-section $L \times L$ in the form of an infinite series[190]

$$\kappa = \frac{L^2}{4} \left[\frac{1}{3} - \frac{64}{\pi^5} \sum_{n=0}^{\infty} \frac{\tanh((2n+1)\pi/2)}{(2n+1)^5} \right] \approx \frac{L^2}{4} \cdot 0.140577. \tag{5.4}$$

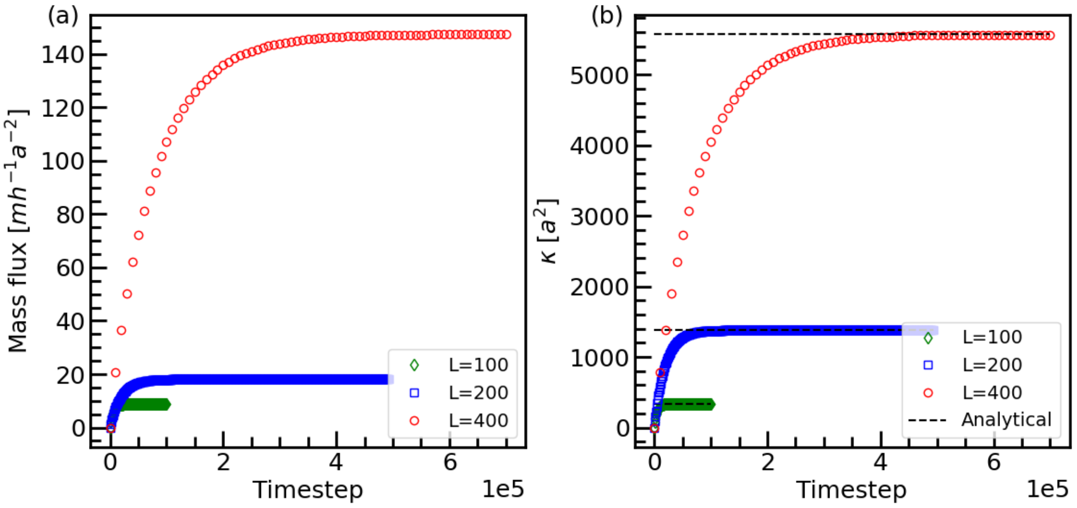

Figure 5.3: Time evolution of mass flux and measured trans-plane permeability κ of square channel of size $L = 100, 200$ and 400.

We determined the conductance of the square channel of side length 100, 200 and 400 lattices, both from the slope of the $q - \Delta p$ curve and directly from Darcy's law, The results are in excellent agreement with the analytical prediction, as shown in Fig. 5.3.

In addition, we checked that the chosen lattice spacing a was sufficiently small to avoid effects due to finite grid resolution. Discretization errors in the LBM are mainly caused by the bounce-back boundary conditions and by Knudsen effects in small pores [191, 192]. The Knudsen number can be tuned by viscosity according to the definition: $Kn = l_{\text{mfp}}/D = \mu/(c_s D)$, where D is the width of channel in pore region. The width of channel decreases in small pores, leading to higher Kn. These effects may lead to a viscosity dependent error in the permeability of a porous medium. We performed simulations of flow in random fibrous geometries with porosities between 24% and 97% with resolution of $a = 1$ μm and $a = 0.5$ μm, respectively, corresponding to simulation domains of 200^3 and 400^3 lattice sites. When plotted over the porosity, the measured permeabilities are virtually indistinguishable between the two resolutions. The relative error $\delta_\kappa = |\kappa_{200}/\kappa_{400} - 1|$ between the high-

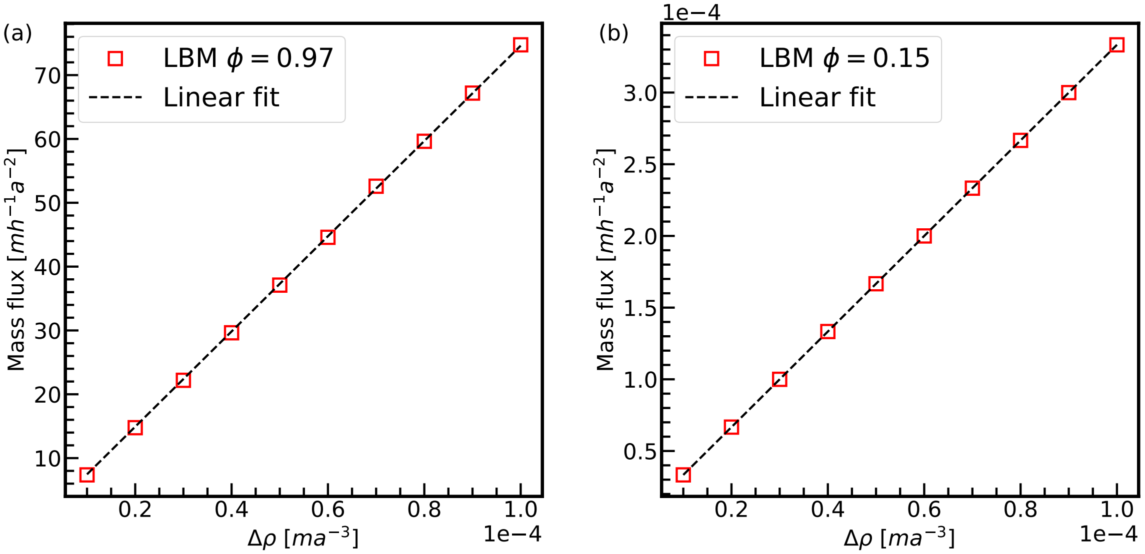

Figure 5.4: Linear correlation between pressure gradient and mass flux for random fibrous media of porosity 0.97 and 0.15.

resolution permeability κ_{400} and the low-resolution permeability κ_{200} is less than 4% in all cases. The relative error of the measured tortuosity is even lower (<0.5%). These results indicate that the higher resolution does not increase the accuracy here. All results below are thus reported for simulations using a cubic lattice of size $(200a)^3$.

Finally, we checked that the measured flow rate in the fibrous media obey linear relationship for the range of applied pressure gradients. We validated the linear relationship between q and $\Delta P/L$ at both the upper limit of 97% porosity and the lower limit of 15% porosity in Fig. 5.4. The Reynolds number $\mathrm{Re} = u\langle D_p \rangle/\nu$ calculated based on the measured mean flow velocity u and mean pore diameter D_p in the fibrous media is in the range of 1.6×10^{-7} to 1.4×10^{-1}. In very low porosity media, local countercurrents may lead to a threshold hydraulic gradient below which no macroscopic flow occurs [7]. This pre-Darcy regime, that has been reported in experimental studies [193, 194], is outside the scope of the current work. The results of the simulations validate that the averaged flow rate is in the linear relationship with the pressure difference for the range of porosities and applied pressure gradients considered here.

The steady-state velocity fields in a plywood and a random fibrous medium are shown in Fig. 5.5. The flow in the random geometry is more complex and heterogeneous than in the plywood geometry. While the plywood geometry exhibits straight flow paths between interconnected pores throughout the thickness, the random geometry requires the flow path to curve around the fibers leading to a higher tortuosity. In addition, due to the heterogeneous pore sizes the velocity varies considerably between different regions of the pore space. In the following, these features and their impact on the permeability and tortuosity are analyzed in detail.

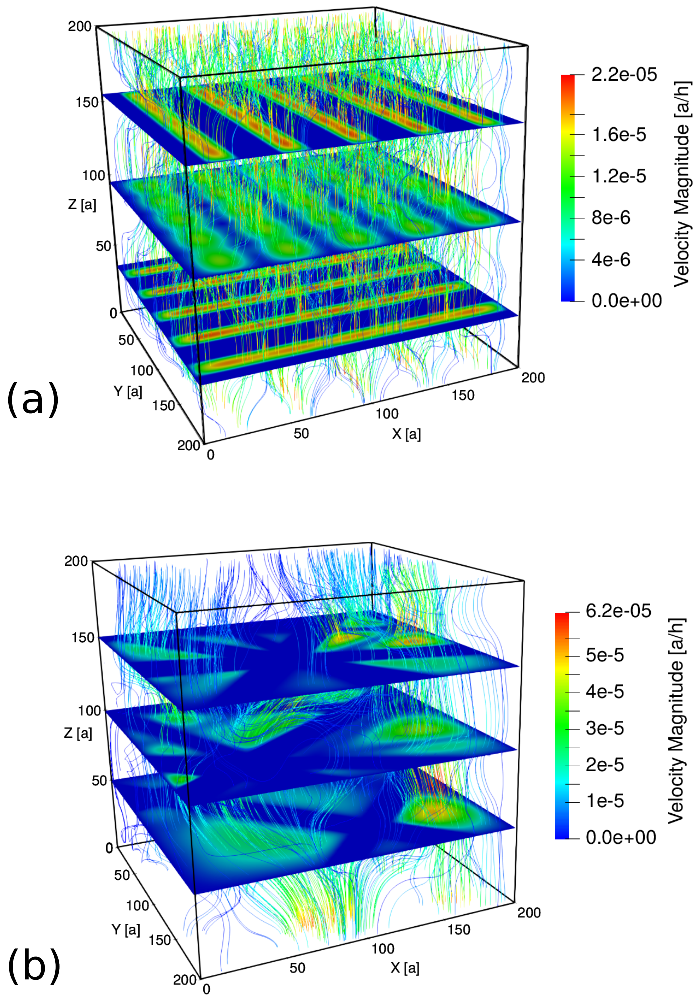

Figure 5.5: Velocity fields in (a) plywood and (b) random media obtained from lattice Boltzmann simulations of hydraulic flow. The flow patterns are more complex in random fibrous media, where a few larger stream tubes contribute an increased mass flow. Reproduced from Ref. [3] with permission of APS.

5.2 Tortuosity of nonwoven fibrous media

In this work, the hydraulic tortuosity $\tau = \langle \lambda \rangle / L$ can be extracted from the streamlines of flow in complex geometries. Generally, the average can be written in the form

$$\tau = \frac{1}{L} \frac{\sum_i w_i \lambda_i}{\sum_i w_i}, \tag{5.5}$$

where λ_i is the length of the ith discrete streamline and w_i is a weight. However, some ambiguity exists with regard to the definition of the weights w_i. A practical definition was proposed by Matyka et al. [195] and weighs the streamline length $\lambda(\mathbf{x})$ by the local flux $u_\perp(\mathbf{x})$ across an arbitrary surface A

$$\tau = \frac{1}{L} \frac{\int_A \lambda(\mathbf{x}) u_\perp(\mathbf{x}) \mathrm{d}^2 \vec{r}}{\int_A u_\perp(\mathbf{x}) \mathrm{d}^2 \mathbf{x}}. \tag{5.6}$$

It was shown [196] that the surface integral can be written as a volume integral

$$\tau = \frac{\int_V u(\mathbf{x}) \mathrm{d}^3 \mathbf{x}}{\int_V u_{||}(\mathbf{x}) \mathrm{d}^3 \mathbf{x}}, \tag{5.7}$$

where $u_{||}(\mathbf{x})$ is the velocity component parallel to the flow direction. This leads to the particularly simple expression for the flux-weighed tortuosity [196, 197]

$$\tau = \frac{\langle |\mathbf{u}| \rangle}{\langle u_{||} \rangle}, \tag{5.8}$$

where the spatial average is taken over the pore space. In the lattice Boltzmann method, the flux-weighed tortuosity can be computed directly from the velocity field by evaluating Eq. (5.8) using the local steady-state velocities $\mathbf{u}(\mathbf{x})$. The computed results for the tortuosity as function of the porosity of the generated samples are shown in Fig. 5.6.

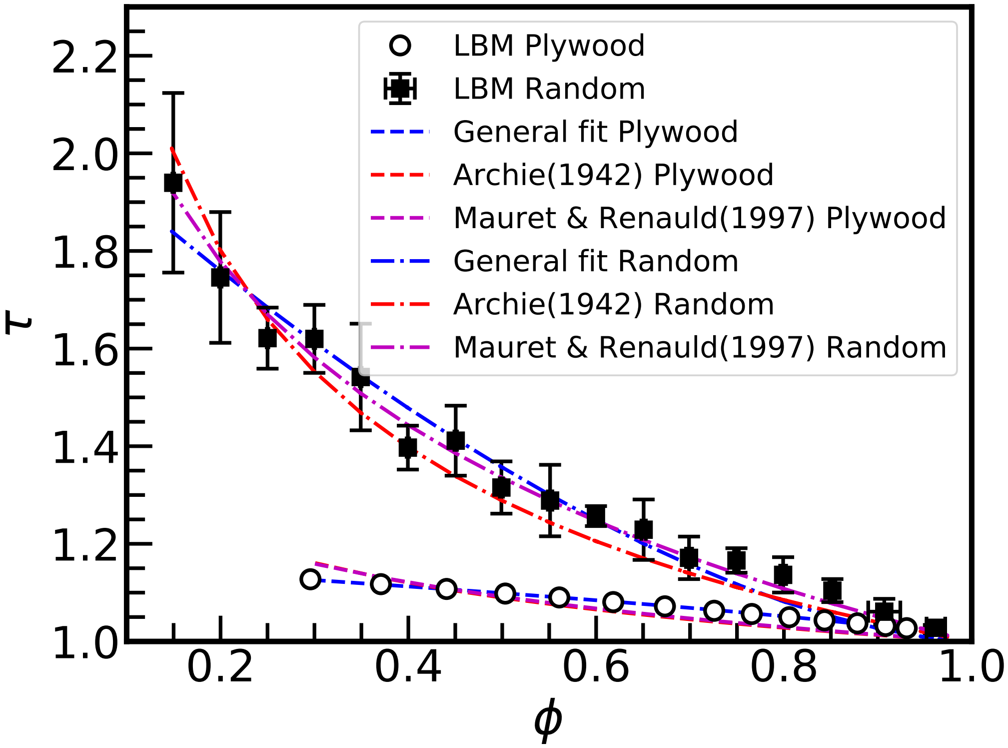

Figure 5.6: Tortuosity as a function of porosity in plywood-type and random fibrous media. The curves show fit results to several common tortuosity expressions for porous media. The tortuosity is significantly increased in random fiber arrangements compared to plywood arrangements, where the flow paths are only slightly elongated even at low porosities. Reproduced from Ref. [3] with permission of APS.

Table 5.1: Results of curve fitting the tortuosity measured in simulations to several common tortuosity expressions, including Archie's law [198], a logarithmic expression used by Mauret and Renauld [173], and a more general expression used by Weissberg [172] and others. Reproduced from Ref. [3] with permission of APS.

Porous structure	**Reference**	**$\tau - \phi$ relation**	**Parameters**	r^2
Granular beds	Archie (1942) [198]	$\tau = \phi^{-\gamma}$	Plywood $\gamma = 0.1238 \pm 0.0088$	0.5851
			Random $\gamma = 0.3655 \pm 0.0054$	0.9029
Packed beds	Mauret & Renauld (1997) [173]	$\tau - 1 = p \ln \phi$	Plywood $p = 0.1321 \pm 0.0092$	0.6377
			Random $p = 0.4834 \pm 0.0080$	0.9260
Freely overlapping	Weissberg (1963) [172]	$\tau - 1 = p(1-\phi)^{\gamma}$	Plywood $p = 0.1621 \pm 0.0016$, $\gamma = 0.7118 \pm 0.0104$	0.9982
obstacles	Ho (1982) [199]		Random $p = 1.0871 \pm 0.0374$, $\gamma = 1.6085 \pm 0.0781$	0.9083

The tortuosity is often assumed to follow Archie's law $\phi/\tau^2 \propto \phi^m$ [198], where m is referred to as the cementation factor [59], i.e.,

$$\tau = p\phi^{-\gamma}, \tag{5.9}$$

where p is a constant and $\gamma = \frac{m-1}{2}$. More generally, the scaling relation for the tortuosity can be written in the power law form as [172, 199]

$$\tau - 1 = p(1-\phi)^{\gamma}. \tag{5.10}$$

Various conjectures have been made in the literature on the relationship between tortuosity and porosity, and propositions for parameters in (5.10) are based on different theoretical arguments and fitting results. For diffusional transport in porous media, Weissberg [172] argued that

$$\tau - 1 = -p\ln(\phi), \tag{5.11}$$

with $p = 1/2$, implying a lower bound $-\frac{1}{2}\ln\phi \approx \frac{1}{2}(1-\phi)$ with $\gamma = 1$. The logarithmic relation (5.11) was also used in a study on the hydraulic tortuosity of fiber mats by Mauret and Renauld [173].

The curve fitting results for the tortuosity of the random fibrous media considered here are shown in Table 5.1 and plotted in Fig. 5.6. The fit of Archie's law yields the exponents $\gamma = 0.124 \pm 0.009$ for plywood geometries and $\gamma = 0.365 \pm 0.005$ for random geometries. The values are significantly smaller than $\gamma = 1$ showing the slow increase of tortuosity with decreasing porosity. The coefficient of determination is relatively low for plywood geometries. This is because the plywood arrangement of the fibers allows straight paths through the rectangular areas between the crossing points of fibers in different layers. The flow along these paths can permeate the entire mat without deflections even at very low porosities.

The generalized expression in Eq. (5.10) yields a better fit to the tortuosity data. The fit parameters are $p = 0.162 \pm 0.002$ and $\gamma = 0.71 \pm 0.01$ for the plywood geometries, and $p = 1.087 \pm 0.037$ and $\gamma = 1.61 \pm 0.08$ for the random geometries. Both the exponent and the prefactor are lower for plywood fiber arrangements as a result of the minor impact of porosity on the tortuosity.

For the logarithmic relation Eq. (5.11) of Mauret and Renauld [173], we find a coefficient $p = 0.132 \pm 0.009$ for the plywood geometries and $p = 0.483 \pm 0.008$ for the random geometries. The latter value is similar to the value $p = 1/2$ found for systems of overlapping spheres [172, 199] but different from the values $p = 1$ or $p = 2/3$ found for arrangements of cylinders [200]. This shows that the tortuosity of fibrous membranes is not as strongly dependent on the porosity as in other porous media. Nevertheless, the logarithmic relation gives the best fit to the data for random fibrous geometries, which is in line with the finding of Matyka et al. [195] for flow simulations in a system of freely overlapping squares.

Based on the curve fitting results, we cannot single out a specific one of the various tortuosity expressions that describes the $\tau - \phi$ relationship in the fibrous porous media considered here. In contrast to arrangements of small obstacles that are often used to model porous media, fibers span the whole system and the streamlines cannot split and merge along the fiber axis. This may lead to a qualitatively different streamline pattern in the fibrous medium and affect the tortuosity calculation based on the velocity field. The slow increase of the tortuosity with decreasing porosity suggests that even in relatively dense fiber arrangements the flow paths are not significantly elongated. This may be a result of the layered structure, where the projections of pores along the flow direction may overlap between layers, such that the streamlines can traverse several layers without deflection. This is obvious in the plywood geometries, where the rectangular overlay pattern always allows straight paths through the entire system. The random fiber orientations reduce the number of straight paths but do not generate as many streamline distortions as in granular porous media.

An interesting observation is the difference between the Archie exponent γ and the exponent m found by fitting Costa's permeability expression in the next section. These exponents are related by $\gamma = (m-1)/2$, however, the separate fits to the porosity and the tortuosity confirm this relation neither for the plywood geometries nor for the random geometries. This indicates that lumping the averaged structural properties τ and ϕ into general expressions does not capture the effects of the local pore-space structure accurately.

5.3 Trans-plane permeability of nonwoven fibrous media

The permeability measures the hydraulic conductivity, and the functional form of its dependence on the various characteristics of porous materials is a-priori unknown. Here we only consider the scalar permeability. The Kozeny-Carman relation described in Section 1.1.2 was re-examined by Costa [59] by considering the pore space as a random fractal with no symmetry axes, which leads to the expression

$$\kappa = C_c \frac{\phi^m}{1-\phi}, \tag{5.12}$$

with a semi-empirical coefficient dimensional C_c.

Although these $\kappa - \phi$ relations have been found to describe various classes of porous media well, the Kozeny model does not always yield quantitative agreement, in particular at high porosities $\phi \to 1$. Hence various other relations have been proposed for porous media including fibrous materials. Gebart [201] theoretically and numerically analyzed the flow through ordered arrays of fibers and arrived at the relation

$$\kappa = C\left(\sqrt{\frac{1-\phi_c}{1-\phi}} - 1\right)^{\frac{5}{2}}, \tag{5.13}$$

where ϕ_c is the percolation threshold of porosity below which no flow occurs, and C is a dimensional parameter. The derivation is based on the assumption that the permeability of flow perpendicular to the fiber axis is dominated by the throats formed between the fibers at their closest distance, which mainly holds for close-packed arrangements of fibers. Other studies have reported an exponential dependence of the permeability on the porosity [202, 181]. However, the data used to fit the exponential relation did not cover porosities near the percolation threshold ϕ_c. Nabovati et al. [60] included a wide range of porosities from near the percolation threshold to dilute systems and found that good fitting results can be obtained with a generalized version of Gebart's expression (5.13)

$$\kappa = C_1\left(\sqrt{\frac{1-\phi_c}{1-\phi}} - 1\right)^{C_2}. \tag{5.14}$$

However, they only considered isotropic 3D fibrous media The validity of these relations for 2D nonwoven fibrous media is thus an open question. Unlike the porosity and specific surface area, the tortuosity is not easily accessible in experimental measurements. In many cases, only the combined value of $C_{kc}k = C_k\tau^2$ can be extracted from the permeability relations (1.8), leaving the Kozeny-Carman coefficient and the tortuosity undetermined. Moreover, the precise notion of tortuosity depends on the transport mechanism and several specific definitions have been discussed in the literature[203].

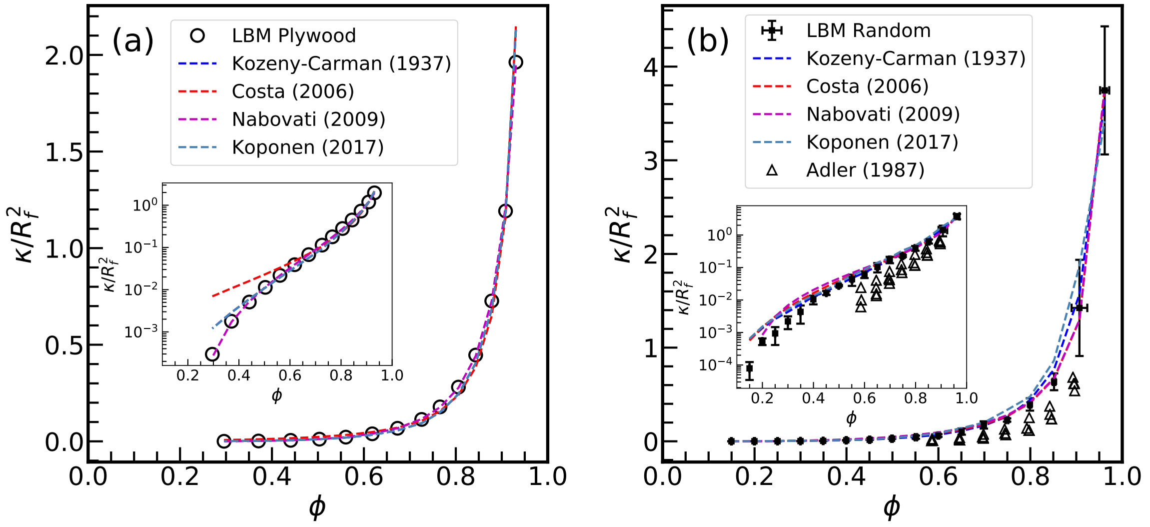

Figure 5.7: Dimensionless permeability as a function of porosity in (a) plywood and (b) random fibrous media. The curves show the fit results to several common permeability expressions for porous media. The logarithmic scale (inset) shows appreciable differences at low porosities for Kozeny-Carman type permeability expressions. Adapted from Ref. [3] with permission of APS.

Table 5.2: Results of curve fitting the permeability measured in simulations to several common permeability expressions including the Kozeny-Carman relation [13, 14], random fractals with no symmetry axis (Costa [59]), random overlapping fibers (Nabovati et al. [60], and a microstructure-based relation by Koponen et al. [56]. Reproduced from Ref. [3] with permission of APS.

Fibrous medium	**Reference**	**$\kappa-\phi$ relation**	**Parameters**	r^2
Kozeny-Carman	Kozeny (1927) [13]	$\kappa = \frac{1}{C\tau^2 S_0^2}\frac{\phi^3}{(1-\phi)^2}$	Plywood $C = 5.0936 \pm 0.1171$	0.9865
	Carman (1937) [14]		Random $C = 1.8568 \pm 0.0260$	0.9962
Pulp sheets	Koponen et al. (2017) [56]	$\kappa = \frac{1}{C\tau^2 S^2}\frac{\phi^3}{(1-\phi)^2}\frac{\langle D_p^4\rangle\langle D_p\rangle^2}{2\langle D_p^2\rangle^3}$	Plywood $c_t = 2.5479 \pm 0.0587$	0.9865
			Random $c_t = 1.5844 \pm 0.0605$	0.9726
Fiber mats	Costa (2006) [59]	$\kappa = C_c \frac{\phi^m}{1-\phi}$	Plywood $C_c/a^2 = 5.7394 \pm 0.3025$, $m = 0.9672 \pm 0.3480$	0.9760
			Random $C_c/a^2 = 23.4039 \pm 0.3564$, $m = 3.0641 \pm 0.2270$	0.9984
Overlapping	Nabovati et al. (2009) [60]	$\kappa = C_1\left(\sqrt{\frac{1-\phi_c}{1-\phi}} - 1\right)^{C_2}$	Plywood $C_1/a^2 = 0.2826 \pm 0.0191$, $C_2 = 2.2755 \pm 0.0291$	0.9997
fibers			$\phi_c = 0.2299 \pm 0.0219$	
			Random $C_1/a^2 = 0.3761 \pm 0.1256$, $C_2 = 1.7550 \pm 0.0956$	0.9981
			$\phi_c = 0.1496 \pm 0.1647$	

The flow field from LBM simulations were used to determine the trans-plane permeability of nonwoven fibrous media. The computed results for the permeability as a function of the porosity of generated samples are shown in Fig. 5.7. As expected, the random fibrous samples show a considerably lower permeability than the plywood fiber geometries. We also compared the LBM simulation results with the transversal permeability determined from Monte Carlo simulations from Ref. [204]. The porous media used in Monte Carlo simulations is derived from the classical site percolation, in which the grid is occupied by solid or liquid randomly in each square lattice of size a. The squares which are occupied by the solid phase are prolongated in solid bundles, along the longitudinal direction. The porous media generated using this approach is different from fibrous media where the curvature of fibers play a key role in the porous structure. The simulation is performed on a 2D lattice with $N_c \times N_c$ squares of size a. Fig. 5.7 shows that the transversal permeability measured in Monte Carlo simulations is slightly lower than LBM simulation results in the porosity range $0.6-0.9$.

We evaluated the accuracy of the permeability expressions (1.8), (5.12), and (5.14) for plywood fibrous media. The curve-fitting results are shown in Table 5.2 and plotted in Fig. 5.7. We report the fit values obtained with the `curve_fit` function in SciPy along with the variance of the parameter estimate and the coefficient of determination r^2. All relationships yield a good fit with a coefficient of determination $r^2 > 0.97$. However, plotting the curves on a logarithmic scale as shown in the inset axes in Fig. 5.7 reveals that the Kozeny–Carman type expressions (1.8) and (5.12) overestimate the permeability at lower porosities $\phi < 0.5$.

The fitted Kozeny-Carman coefficient is $C_{kc} = 5.09 \pm 0.12$ for the plywood geometries and $C_{kc} = 1.86 \pm 0.03$ for the random geometries. The value for plywood geometries is in good agreement with the value of $C_{kc} \approx 5$ that has been found for porous beds of spherical and nonspherical particles [14, 205]. The significant difference between random and plywood fiber arrangements indicates that the Kozeny-Carman coefficient for fibrous porous media is non-universal and depends on the microstructure of the pore space. The randomness of the fiber orientations reduces the permeability by a factor greater than 2.5.

The coefficient C_c in Costa's expression [59] is a dimensional parameter that incorporates the pore cross-sectional area. We obtain the fitted values of $C_c/a^2 = 5.74 \pm 0.3$ for the plywood fiber geometries and $C_c/a^2 = 23.4 \pm 0.36$ for the random fiber geometries. The tortuosity factor is $m = 0.97 \pm 0.35$ for the plywood fiber geometries and $m = 3.06 \pm 0.23$ for random fiber geometries. The value for random fiber mats is close to the value 3.48 found by Costa for sisal and jute fiber mats [59]. The difference of m between plywood fiber geometries and random fiber mats indicates that the scaling of the tortuosity is significantly altered by the random fiber orientation. Costa's expression for the permeability is based on the assumption of a fractal fragmented system, and the appreciable difference for plywood fiber geometries at lower porosities owes to the fact that the plywood arrangement of the fibers does not represent a random fractal with no axes of symmetry.

The permeability expression by Nabovati et al. [60] is based on Gebart's analytical treatment of flow through narrow slots between close-packed fibers and includes three fitting parameters C_1, C_2, and ϕ_c. We obtain $C_1/a^2 = 0.28 \pm 0.02$, $C_2 = 2.28 \pm 0.03$, and $\phi_c = 0.23 \pm 0.02$ for the plywood fiber geometries, and $C_1/a^2 = 0.38 \pm 0.13$, $C_2 = 1.76 \pm 0.10$, and $\phi_c = 0.15 \pm 0.16$ for random fiber mats. The close values of the coefficient C_1 and the exponent C_2 for both geometries and the improved quality of the fit to the data suggest that the permeability expression [60] is more applicable to fibrous porous media . The improvement stems from the inclusion of the critical porosity below which no percolating paths exist and no permeating flow occurs. The critical porosity is higher for the random fiber arrangements because this random orientation of the fibers leads to more isolated pores that are not connected to the open pore space.

Overall, we conclude that the Kozeny-Carman type permeability expressions do not fully capture the effect of fiber microstructure on the permeability for low-porosity fibrous mats with random fiber distribution. This may be explained by the presence of isolated pores that do not contribute to fluid transport, leading to a reduction of the number of percolating paths through the pore space when the packing density of the fibers is large. This effect is taken into account by the model of Ref. [60] which therefore leads to a more accurate prediction of the permeability of fibrous media with closely packed fibers.

5.4 Microstructure effects of fibrous media

The κ-ϕ and τ-ϕ relations hide the microstructure of the porous medium in the parametric coefficients and exponents. It is therefore interesting to investigate the dependence of these parameters on the structural properties of the pore network. In our randomly generated fibrous media, the main parameters are the fiber diameter and the allowance of overlaps. The effects of these factors are reported here.

5.4.1 Effect of fiber radius

The fiber radius is one of the parameters that can be tuned in the production process of fiber membranes, and it has a major effect on the porosity and the microstructure of the pore space. Since the permeability has units of length squared, it is commonly normalized by the square of a characteristic length scale. For the fibrous media, a suitable length scale is the fiber radius R_f. To study the individual effect of fiber diameter on the permeability, we have plotted the permeability as a function of fiber diameter at constant porosity in Fig. 5.8. Empirical models have been established to relate the in-plane and trans-plane permeability to the measurable structural properties, porosity and fiber radius [206, 207], which suggest a quadratic dependence of the permeability on the fiber diameter. Our data clearly shows the validity of these assumptions. Since the specific surface area decreases as the inverse fiber radius, the quadratic increase of the permeability implies a $R_f^{-1/2}$ scaling of the tortuosity. The fitted lines in Fig. 5.8 suggest that the computed tortuosity follows

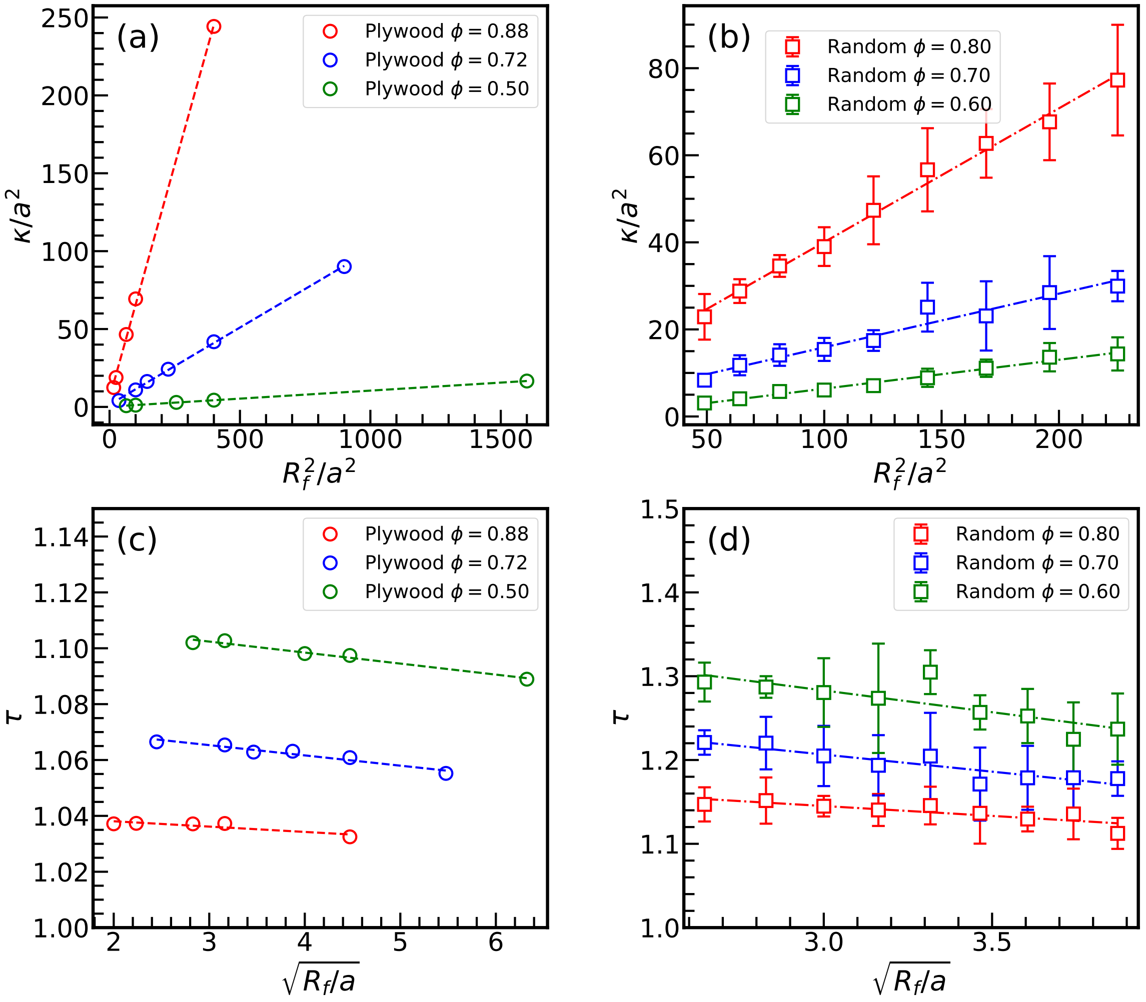

Figure 5.8: Influence of the fiber radius on the permeability ((a) and (b)) and tortuosity ((c) and (d)) of plywood ((a) and (c)) and random ((b) and (d)) fibrous media. The lines represent linear fits to the data. The permeability increases quadratically with the fiber radius which confirms the fiber radius as a characteristic length scale. The square of the tortuosity decreases apparently linearly with increasing fiber radius. Reproduced from Ref. [3] with permission of APS.

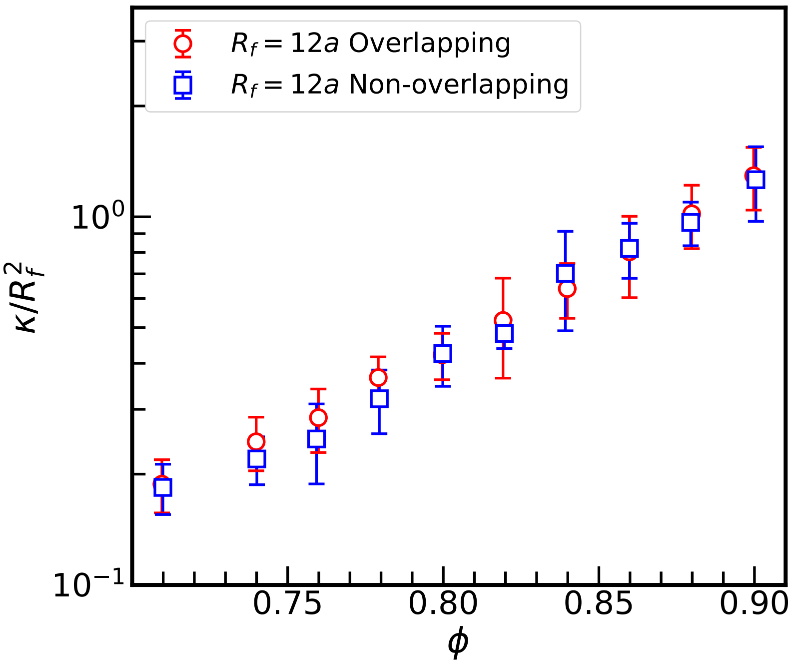

Figure 5.9: Influence of fiber overlapping on (a) permeability and (b) tortuosity of random fibrous media with porosities in the range $0.70 \le \phi \le 0.90$. Reproduced from Ref. [3] with permission of APS.

this scaling to a reasonable degree.

5.4.2 Effect of fiber overlapping

We investigated the effect of fiber overlapping on the hydraulic properties of fibrous media. As explained above, we allowed the fibers to overlap in order to generate geometries with lower porosities which cannot be obtained with non-overlapping fiber arrangements. In Fig. 5.9, we compare the permeability and tortuosity of overlapping and non-overlapping fiber geometries. Previous results by Sousa [208] suggest that the effect of overlapping is to decrease the permeability in low porosity media, while it is negligible for porous media with $\phi > 0.85$. In the investigated porosity regime, our results show no significant difference between the permeability of non-overlapping and overlapping fiber arrangements . Overall, allowing the fibers to overlap has no pronounced influence on the trans-plane permeability of nonwoven fibrous media. This fact may be used to strengthen the mechanical properties of filter materials without affecting their hydraulic properties.

5.5 Conclusions

We have presented a computational analysis of the dependence of trans-plane permeability on the microscopic pore-space properties of nonwoven fibrous porous media. Randomly generated three-dimensional fiber arrangements served as realistic models of fibrous porous mats. We employed the lattice Boltzmann method to simulate fluid flow through nonwoven fibrous media and obtained the permeability and tortuosity from the simulated flow field. The results reveal the dependence of permeability and tortuosity on the pore-space morphology of nonwoven fibrous media. We have performed curve-fitting of several of the most common expressions to the values of permeability and tortuosity obtained from the simulations. These formulas are summarized in Tabel 5.1 and 5.2. Our results reveal that the classical Kozeny-Carman type expressions overestimate the permeability of low-porosity fibrous media, and a semi-empirical expression in Ref. [60] yields better agreement with our data. The improvement can be ascribed to the inclusion of a critical porosity below which no flow occurs, and the fitting results indicate that the critical porosity is higher in random fibrous media due to an increased number of small unconnected pores. In general, we found that the Kozeny-Carman coefficient can vary substantially with porosity.

CHAPTER 6

DROPLET SURFACE MORPHOLOGY TRANSITION ON FIBER

6.1 Introduction

N95 respirator, which is composed of multilayers of polypropylene (PP) nonwoven fabrics, has become the best protective method since the outbreak of COVID-19 pandemic. Numerous researches have been conducted to make masks more efficient and understand the efficiency metric. We focus on one side of this problem asking what is the criterion for capturing aerosol droplets by a single fiber in a fibrous mask. These droplets are small and hence inertial forces are not important in the process of drop attachment to the fiber. Therefore, the wetting properties of fibers and the fiber diameter become the crucial parameters in the mask design. This topic is of fundamental interest to materials science as it provides insight on phenomena of wetting and adhesion to fibrous materials.

When a small droplet is placed on a cylindrical fiber of definite radius, its equilibrium shape is determined by the contact angle, fiber radius and drop volume [104, 209, 17, 106]. For the case of small contact angle and large drop volume, the drop takes an axisymmetric barrel shape. When the contact angle is sufficiently large and drop volume is small, non-axisymmetric clam-shell drops are observed. The axisymmetric droplet is typically firmly adhered to the fiber and hence can be considered as being captured in a fibrous mask. The clamshell droplets are easy to shade off and hence the materials properties of the fibers that lead to clamshell droplets are considered undesirable.

In the absence of gravity, the Laplace excess pressure Δp across the droplet surface is constant when the droplet is in equilibrium, i.e.,

$$\Delta P = \gamma\left(\frac{1}{R_1} + \frac{1}{R_2}\right) = \text{contant}, \tag{6.1}$$

where R_1 and R_2 are the principal radii of curvature , γ is the surface tension. In general, R_1 and R_2 vary along the drop surface. The barrel shaped drop can be modeled by an unduloid [104]. Carrol [209] presented an experimental study on the movement of a droplet off a cylindrical fiber as the droplet volume increased. The critical volume for the transition were determined prior to the roll-up event.

McHale et al. [106] employed a numerical approach using finite element method to solve Eq. (6.1) with Surface Evolver [210] package by evaluating the surface free energy of both barrel shape and clam-shell droplets. The absolute stable conformation is determined as the one with lower surface free energy for a given volume and contact angle. McHale et al. [211, 17] suggested that the inflection point on a barrel shape droplet should be considered as the criterion for stability between the two conformations. The inflection point is where one of the radii of curvature change sign. The existence of inflection point in the profile of a barrel shape drop is necessary to minimize the Laplace excess pressure in Eq. (6.1). Therefore, the minimal value of reduced thickness n_{min} has been derived as follows to satisfy the inflection point condition [211],

$$n_{\text{min}} = \frac{1 + \sin\theta_E}{\cos\theta_E}. \tag{6.2}$$

By considering the response of the system to the changes in the Laplace excess pressure, the metastability condition, which describes the ability of a given shape against perturbations of the shape, is given as [209].

$$2n^3 \cos\theta_E - 3n^2 + 1 = 0, \tag{6.3}$$

where θ_E is the equilibrium contact angle, $n = R/R_f$ is the reduced thickness, R and R_f are the thickness of liquid and the fiber radius, respectively.

In the recent work by Chou et al. [212], the coexistence of barrel shaped and clam-shell droplet for the same droplet volume and contact angle has been shown from experimental observations and Surface Evolver simulations. By employing two different initial shapes, Chou et al. [212] reported that one can obtain either barrel or clam-shell for certain range of droplet volumes and contact angles. The morphology diagram is constructed from Surface Evolver simulations and it consists of three regimes: barrel only, clam-shell only, and barrel and clam-shell simultaneously. The stability of both conformations in the uncertainty regime has been verified by applying a shape perturbation. Both conformations can sustain small perturbations and relax back to their equilibrium conformation.

In this chapter, we use multicomponent pseudopotential LBM model to simulate the morphological transition of droplet deposited on a fiber. The method has been employed by Wang et al. [213, 214] to investigate the dynamic spreading and retraction of certain amount of liquid on parallel fiber rails, which confirms the existence of bistable regions in the morphology diagram. They constructed the energy landscape associated with droplet wetting length and probed the energy barrier of shape transformations. In this work, we adopted two different initial shapes to study the barrel shaped and clam-shell droplets on a single fiber. The accuracy of LBM simulation is validated by comparing the profile of barrel shape drop in equilibrium with experimental results and analytical description. We study the dynamics of wetting behavior of an initially sitting-on and wrapping-around droplet configurations. Finally, the morphology diagram determined from LBM simulations is compared with experimental and analytical results. The code used to generate the figures in this chapter is modified from Ref. [214].

6.2 Simulation conditions

The numerical simulations of droplet wetting a fiber have been carried out using the parallel lattice Boltzmann code LB3D [186]. A rectangular domain of size $240a \times 240a \times 300a$ was created and a fiber was placed with its center at $x = 120a$, $y = 120a$ and $z = 150a$. Periodic boundary conditions were applied at all domain boundaries. The fiber diameter corresponds to 20 lattice sites. A contact angle ranging from 10° to 68° is realized by varying the pseudo wall density ρ_{wall} from -0.5 to -0.15. Mid-link bounce back boundary condition was employed at the fiber surface to achieve the no-slip conditions. Due to the diffusion nature of multicomponent LBM model, contact line motion is allowed over the no-slip walls.

In order to create a droplet in the computation domain, we performed the Laplace test as described in Sec. 3.4.2. This test allowed us to determine the equilibrium densities of the two fluid components for the given coupling strength g_{br} and drop diameter. An intermediate coupling strength $g_{br} = 0.14\rho_0 a^2/h^2$ is used throughout this work to achieve the desired phase separation and maintain the numerical stability. From the linear fitting of Laplace pressure and inverse of drop radii, the surface tension γ is determined to be $\gamma = 0.165\rho_o a^3/h^2$. We chose the BGK relaxation time of the two components as $\tau_b = \tau_r = 1h$, resulting in a kinematic viscosity ratio of 1.0. As an initial condition, the fluid is set at rest. The droplet on a fiber can adopt symmetrical barrel-shape or non-axisymmetric clam-shell shape. To investigate the energetically preferential shape, we use a wrapping-around conformation that is fully engulfing the fiber as the initial approximation of a barrel-shaped drop, and a sitting-on conformation that is partially engulfing the fiber as the initial approximation of a clam-shell drop, as shown in Fig. 6.1(a). Here, we varied the initial droplet radius in order to study the effect of drop volume on equilibrium conformation, thus the initial contact angle is arbitrarily chosen based on the initial droplet radius. During simulations, we monitored the Laplace excess pressure across the interface until it reaches the equilibrium state. The Laplace excess pressure is defined by choosing a probe inside the droplet and another one outside, then calculating the pressure difference ΔP between the two probes. The droplet is in equilibrium when the Laplace excess pressure satisfies the criteria

$$\left|\frac{\Delta P(t) - \Delta P(t - 1000h)}{\Delta P(t)}\right| < 10^{-5}, \tag{6.4}$$

where t is the current time-step, and h is the time-step size. The interfacial layer has a finite width due to the diffusion of the two fluid components. Therefore, we define the exact position of interface by introducing the order parameter $\phi = \rho_b - \rho_r$, which is zero at the interface. The droplets volume varies slightly during the morphological transition by using this definition of interface. However, the variation is always less than 3%, and we can consider the droplets as volume conserved.

In order to determine the critical reduced thickness $n = R/R_f$ for the morphology transition between the barrel-shaped and clam-shell drops, the droplet volume was varied stepwise for the two different initial configurations until we observe the transition from one morphology to another. The gravity is not taken into account in the current work. The fiber surface is smooth enough for the chosen resolution and chemically homogeneous such that there is no contact angle hysteresis. For comparison with analytical description and experimental results, the variables are scaled by the fiber radius R_f. We obtained the dimensionless drop volume $\bar{V} = V^{1/3}/R_f$, droplet radius $n = R/R_f$, and dimensionless Laplace excess pressure as $\bar{P} = \Delta P(R_f/\gamma)$. The time scale and velocity are normalized based on viscous-capillary scaling, leading to the dimensionless time $\bar{t} = t\gamma/(\rho\nu R_f)$ and velocity $u/u_{vc} = \rho\nu u/\gamma = Ca$, which is the Capillary number, Ca.

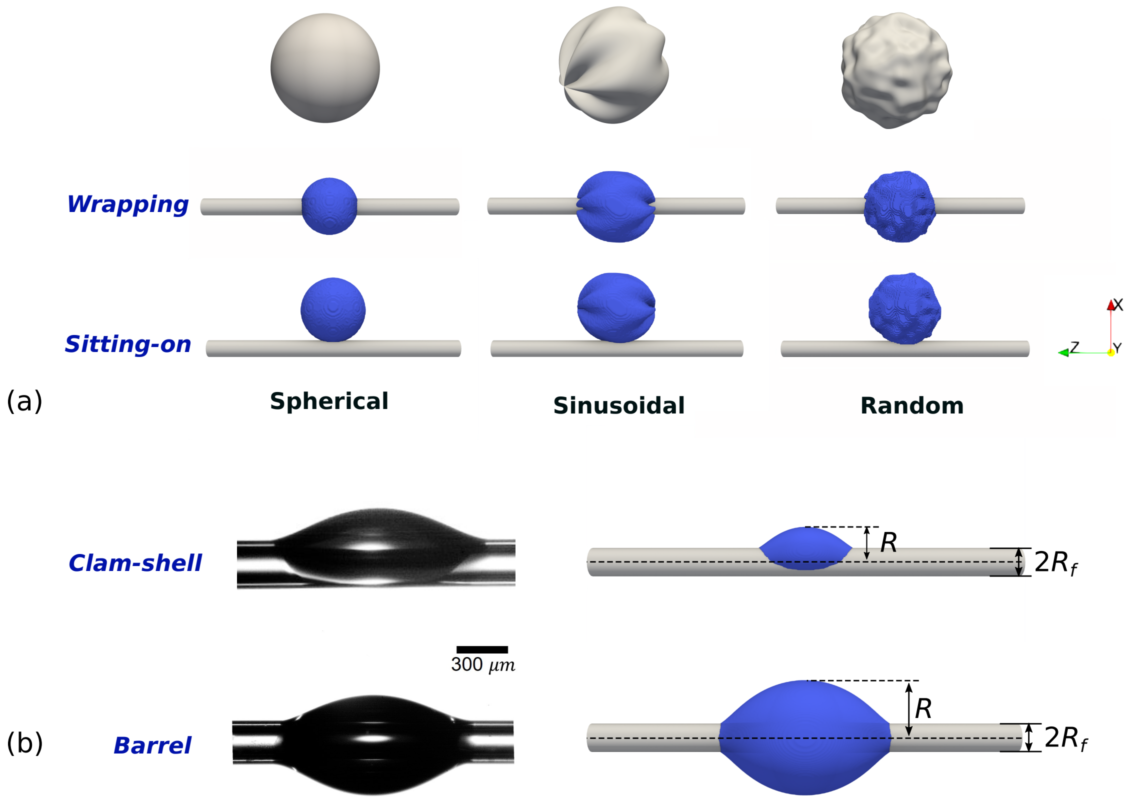

Figure 6.1: (a) The initial droplet configuration on a fiber: the wrapping around approximation for an axisymmetric barrel drop, and the sitting-on approximation for a non-axisymmetric clam-shell drop. Sinusoidal and random perturbations are introduced to the smooth spherical droplet surface. (b) Equilibrium morphology of clam-shell and barrel droplet from (left) deposition experiments and (right) LB simulations. (Experimental image courtesy of Yueming Sun)

Fig. 6.1(b) compares the experimental picture of a barrel drop and clam-shell with equilibrium configurations obtained from LB simulations. Two types of experiments were conducted: drop deposition on a glass fiber and drop formation from a film through fiber coating using glycerol solution. The deposition process is performed by continuously depositing a small drop of diameter around 28 μm on glass fibers with radius R_f = 125 and 40 μm. The time period for deposition is 4950 μs. The deposition experiment continues until the volume of drop is sufficiently large to observe the transition from a clam-shell to barrel drop. It should be noted that contact angle hysteresis of the fiber used in experiment affects the contact line motion, resulting in the asymmetric barrel shape with respect to fiber axis in the droplet deposition experiments. However, the characteristics of barrel drop and clam-shell can still be identified and thus distinguish the two morphologies. Moreover, the maximum Bond number, $Bo = \Delta\rho g R^2/\gamma$ (where $\Delta\rho$ the density difference between the two phases, g the gravity acceleration, R the drop radius, and γ the surface tension) is $Bo = 0.016$, i.e. it is much less than 1, suggesting that the gravitational effect on drop shape can be neglected. Fig. 6.1(b) shows the clam-shell and barrel drop on fibers with contact angle of 22.3° and 35.3°, respectively. The reduced thickness $n = R/R_f$ is defined with the geometric parameters in Fig. 6.1(b).

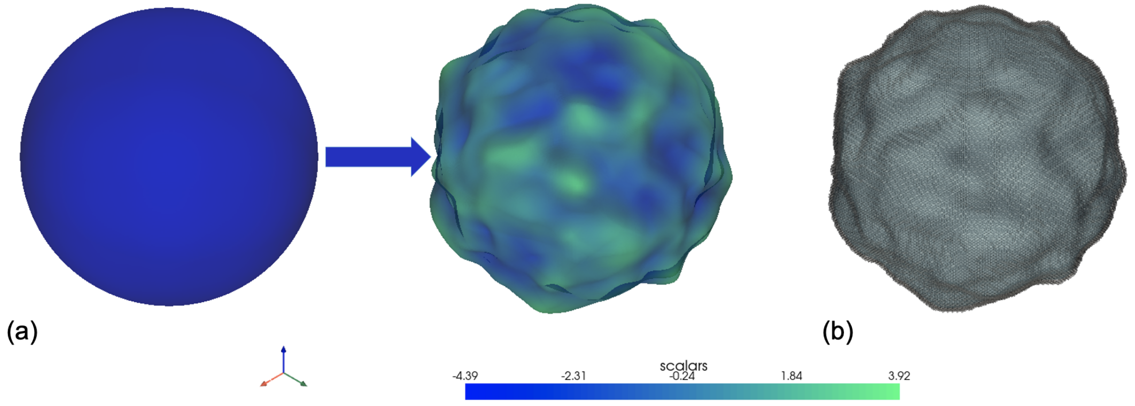

Figure 6.2: (a) Spherical drop with its surface perturbed by Perlin noise. (b) Voxelized surface mesh.

To study the effects of droplet deviation from spherical shape on its equilibrium droplet shape, we considered sinusoidal and random noise, as illustrated in Fig. 6.1(a). The sinusoidal noise is generated as follows: the drop profile in Cartesian coordinates is given by

$$x = r\sin\phi\cos\theta, \quad y = r\sin\phi\sin\theta, \quad z = r\cos\phi + z', \tag{6.5}$$

where r is the fiber radius, $\phi \in [0,\pi]$, $\theta \in [0,2\pi)$, and $z' = h\sin(\lambda\theta + \alpha)$, h, λ and α are the amplitude, angular speed and phase of the sinusoid, respectively. The random noise is generated by using Perlin noise algorithm, which is a type of gradient noise and provides naturally appearing patterns or textures [215]. Here we apply the Perlin noise on a sphere using `PyVista` package [216]. The Perlin noise is generated typically in three steps: 1) pseudorandom gradient vectors are created on the 8 corners of a given grid in a 3D space, then the distance vectors from a given position (x, y, z) to its surrounding corners is calculated, 2) by taking the dot product between the gradient vector and the distance vector, a scalar value is calculated as the influence value to the position (x, y, z), 3) final value of scalar is obtained by interpolating between the noise values, to construct smooth patterns within the grid. As illustrated in Fig. 6.2(a), the sphere is warped by the generated scalar to give some variation in the surface coordinates based on the influence value of the Perlin noise. Finally, the surface mesh of distorted sphere is voxelized and used as the initial configuration in LB simulations, shown in Fig. 6.2(b).

6.3 Results and Discussion

6.3.1 Mathematical model of barrel drop

Carroll [104] proposed a method to estimate the contact angle of a fiber by measuring the wetting length L and reduced thickness n of a barrel-shaped drop. For a small droplet, where gravity can be neglected, the drop longitudinal is illustrated in Fig. 6.3. Considering an arbitrary point $P(x, z)$ on the drop surface, the Laplace pressure across the interface is constant, namely,

$$\frac{1}{R_1} + \frac{1}{R_2} = K_1, \tag{6.6}$$

where K_1 is a constant. The two principal radii of curvature satisfy the following relations:

$$R_1 d\phi = ds \sec\phi, \quad R_2 = x \operatorname{cosec}\phi. \tag{6.7}$$

Substituting Eq. (6.7) into Eq. (6.6) gives

$$\frac{1}{x}\frac{d}{dx}(x\sin\phi) = K_1. \tag{6.8}$$

The integration of Eq. (6.8) gives

$$x\sin\phi = \frac{1}{2}K_1x^2 + K_2. \tag{6.9}$$

The two constants K_1 and K_2 can be determined by applying the boundary conditions, given by the angle ϕ between one of the principal radius of curvature at point P and fiber axis,

$$\phi = \pi/2 - \theta, \qquad x = x_1, \tag{6.10}$$

$$\phi = \pi/2, \qquad x = x_2, \tag{6.11}$$

where θ is the contact angle. Using the relationship $dz/dx = -\tan\phi$, Carroll derived the gradient of the drop profile as [104] ,

$$\frac{d\bar{z}}{d\bar{x}} = \frac{-(\bar{x}^2 + an)}{\sqrt{(n^2 - \bar{x}^2)(\bar{x}^2 - a^2)}}, \tag{6.12}$$

where the reduced coordinates $\bar{x} = x/x_1$ and $\bar{z} = z/x_1$ are normalized by fiber radius x_1. $n = x_2/x_1$ is the reduced thickness and the parameter a is expressed by

$$a = \frac{n\cos\theta - 1}{n - \cos\theta}. \tag{6.13}$$

Integrating Eq. (6.12) with the above boundary condition gives the reduced wetting length $\bar{L} = L/x_1$ as,

$$\bar{L} = 2[aF(\varphi,k) + nE(\varphi,k)], \tag{6.14}$$

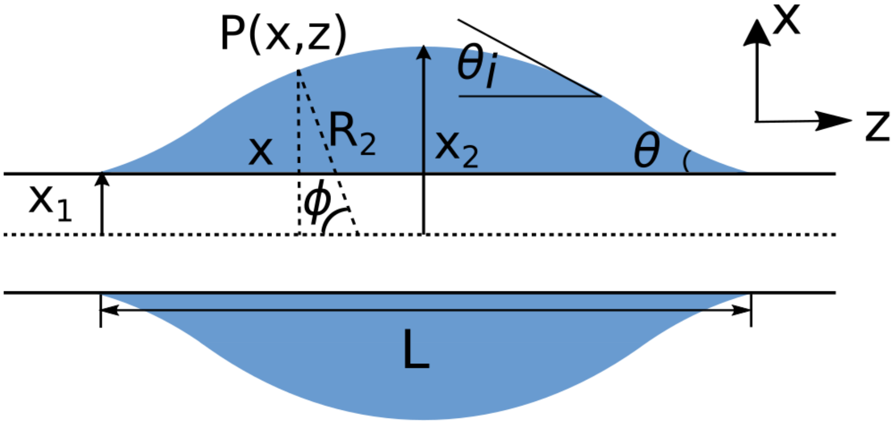

Figure 6.3: Schematic illustration of the cross-sectional geometry of a barrel-shaped drop on a fiber.

where $F(\varphi,k)$ and $E(\varphi,k)$ are elliptic integrals of the first and second kind, respectively. The parameters of elliptic integral φ and k are given by

$$\sin^2\varphi = \frac{n^2-1}{n^2k^2}, \qquad k^2 = \frac{n^2-a^2}{n^2}. \tag{6.15}$$

The reduced drop volume $\overline{V} = V/x_1^3$ can be obtained from the integral of circular cross section area lying between ±$L/2$, and subtraction of the fiber volume,

$$\overline{V} = \frac{2\pi n}{3}\left[(2a^2+3an+2n^2)E(\varphi,k) - a^2F(\varphi,k) + \frac{1}{n}\sqrt{(n^2-1)(1-a^2)}\right] - \pi L. \tag{6.16}$$

Laplace pressure $\overline{\Delta P} = \Delta P(x_1/\gamma)$ in the reduced form is calculated by

$$\overline{\Delta P} = \frac{2(n-\cos\theta)}{n^2-1} \tag{6.17}$$

Therefore, it is possible to evaluate the contact angle θ by measuring drop volume and wetting length using Eq. (6.14) and (6.16). Unlike the complete wetting on flat substrate, where the Laplace excess pressure can be reduced to zero by increasing R_1 and R_2, the two

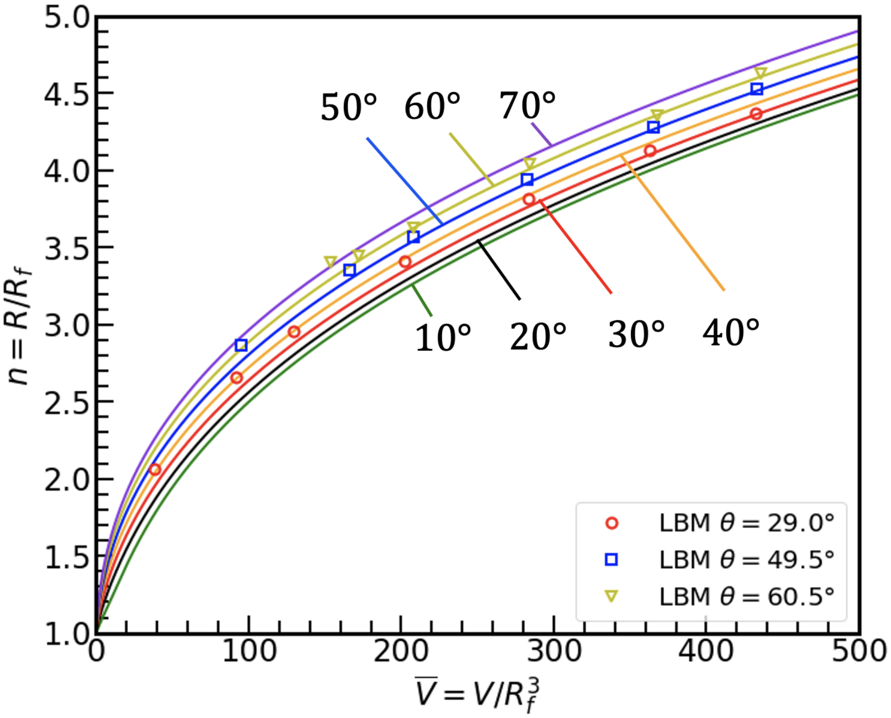

Figure 6.4: The normalized droplet radius n as a function of drop volume $\overline{V}$ measured in simulations (symbols) agree with the analytical calculation (lines).

radii of curvature cannot be increased simultaneously for the barrel shaped droplet. However, the Laplace excess pressure in Eq. (6.1) can still be reduced for the barrel shaped drop by changing the sign of one radius of curvature R_2 relative to the other. This indicates that there exists an inflection point on the profile of barrel drop at where one of radius of curvature changes in sign. The maximum of $\frac{d\bar{z}}{d\bar{x}}$ is obtained at the inflection point. According to Eq. (6.12), the position of $\frac{d\bar{z}}{d\bar{x}}|_{\max}$ is $\bar{x}_{1,2} = \pm\sqrt{an}$ or $\bar{x} = 0$. The inflection point must occur somewhere between x_1 and x_2, suggesting that $\bar{x} = \sqrt{an} > 1$. Solving this inequality gives the minimum value of n [211],

$$n_{\min} = \frac{1 + \sin\theta}{\cos\theta}. \tag{6.18}$$

Fig. 6.4 shows the dependence of reduced thickness n on barrel-shaped drop volume $\overline{V}$. We plot the reduced thickness n calculated from LB simulations along with the analytical prediction from Eq. (6.16). The simulation results show excellent agreement with the theoretical value over the range the liquid volume and fiber contact angle. It can be seen that the deviation from analytical solution slightly increases for small liquid volume. This deviation may be due to the fact that inflection angle is not considered in Carroll's formulation. The inflection angle is larger than equilibrium contact angle, which implies an increase in the reduced thickness n.

We compared the contour of barrel droplet obtained from experiments with simulation results in Fig. 6.5. As we described in the previous section, contact angle hysteresis is not considered in the numerical simulation due to the smoothness and chemical homogeneity of fiber surface. However, the effect of contact angle hysteresis cannot be ignored in experiments. In Fig. 6.5, the advancing contact angle is $\theta_A = 43.8°$ and the receding contact angle is $\theta_R = 33.7°$. During the transition from clam-shell to barrel drop, the liquid is spreading on the bottom and retracting on the top of the fiber. Therefore, the liquid contact angle on the bottom is the advancing contact angle. Here in Fig. 6.5(a), the equilibrium contact angle of fiber used in simulation is 43.2°, close to the advancing contact angle. The droplet morphology obtained from simulation follows the contour (red line) of experimental result on the bottom of the fiber, suggesting that the droplet shape can be determined accurately from simulation for the specified contact angle. Owing to the fact that contact angle hysteresis being ignored in simulation, the simulated barrel drop is always axisymmetric with respect to the cylinder axis. Thus, it deviates from experimental contour on the top. In this case, the drop volume in simulation is $\overline{V} = 11.17$, larger than that in experiment $\overline{V} = 10.94$. In Fig. 6.5(b), we compare the droplet shape on a fiber of equilibrium contact angle $\theta = 33.8°$ with the experimental image. With the same reduced thickness $n = 5.75$, the contact angle formed by the barrel drop is slightly larger than the receding contact angle. We also compared the contour of droplet with the same volume as experiment in Fig. 6.5(c). The fiber contact angle in simulation is the same as advancing contact angle. It can be seen that the reduced thickness n on the bottom part is smaller than that of experiment due to the asymmetry of experimental result.

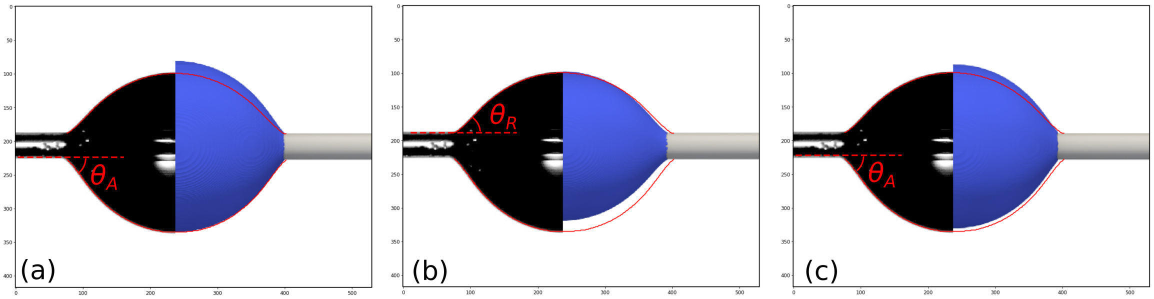

Figure 6.5: Comparisons of barrel droplet contour between experiment and simulation. The fiber radius, drop volume and mean reduced thickness ($n = D/2$, where D is the barrel drop diameter) in experiment are $R_f = 40\mu m$, $\overline{V} = 10.94$ and $n = 6.21$. The droplet contour in experiments are indicated by red lines. Volume and reduced thickness $(\overline{V}, n)$ in simulations are (a) $(11.17, 6.67)$, (b) $(9.80, 5.75)$, and (c) $(10.95, 6.41)$

6.3.2 Effect of initial perturbation

To investigate the effect of drop non-sphericity, we consider sinusoidal and random noise on drop initial shape. Fig. 6.6(a) and (b) shows the simulation snapshots of the time evolution of droplet shape with sinusoidal noise and Perlin noise, respectively. The initial droplet radius is 42 lattice sites and fiber contact angle is 24.5°. For the sinusoidal perturbation, the amplitude h and angular speed λ are 5 and 6, respectively. For the Perlin noise, the scalar value which characterizes the variation of drop radius is generated in the range of $(-5, 5)$. The three phase contact line motion can be observed in Fig. 6.6. For both types of perturbations, the deformed droplets have quite different Laplace pressure initially due to the local variation of radii of curvature, and quickly relax towards an approximate spherical drop under the Laplace pressure difference, followed by the spreading on the fiber. The simulation results shows that final equilibrium conformations are not affected by the initial perturbation. Fig. 6.7 compares the dependency of reduced thickness n on drop volume $\overline{V}$ for equilibrium morphology of barrel drop and clam-shell. Drop volume is slightly different due to the initial perturbation on drop shape. However, the reduced thickness n is very close and follows the same trend for both equilibrium morphology.

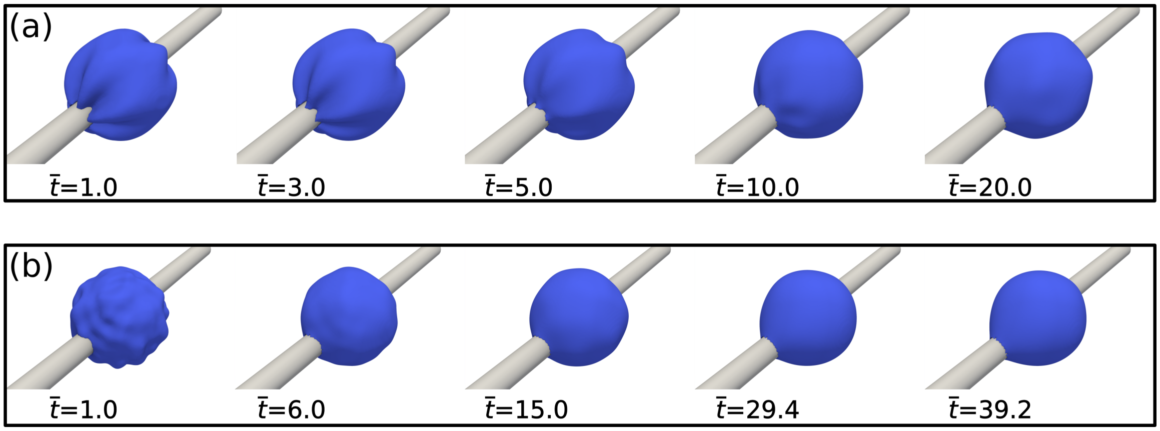

Figure 6.6: Simulation snapshots of the droplet relaxation towards the smooth surface for (a) sinusoidal and (b) random perturbation.

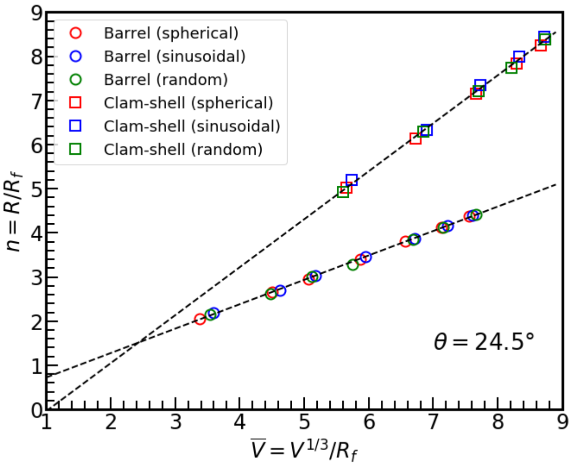

Figure 6.7: Comparisons of reduced thickness n in equilibrium between smooth spherical drop and droplets with sinusoidal and random perturbations. The contact angle is 24.5°.

6.3.3 Transition from barrel-shaped to clam-shell drop

We now focus on the wetting behavior of the wrapping-around droplet during equilibration. Fig. 6.8 (a) shows a sequence of simulation snapshots for droplet with volume $\overline{V} = 4.13$ roll-up on a fiber under the effect of surface tension. The contact angle of the fiber is

49.5°. Carroll [209] investigated the "roll-up" process of droplets from the experiments of solubilization of an oil drop attached to a fiber. The transition from barrel drop to clam-shell was shown during the solubilization of oil drop by an aqueous surfactant, accompanied by the reduction of drop volume. We observe the similar roll-up process of barrel drop from time sequence $\bar{t}$ = 1568.0 to $\bar{t}$ = 7840.0. The barrel drop becomes non-axisymmetric after $\bar{t}$ = 1568.0 and move up to the upper surface of fiber until it finally evolves into a clam-shell conformation. On the other hand, for the larger droplet with volume $\overline{V}$ = 5.06, Fig. 6.8(b) shows the spreading motion of droplet along fiber axis, and it remains the barrel shaped until reaches the steady state.

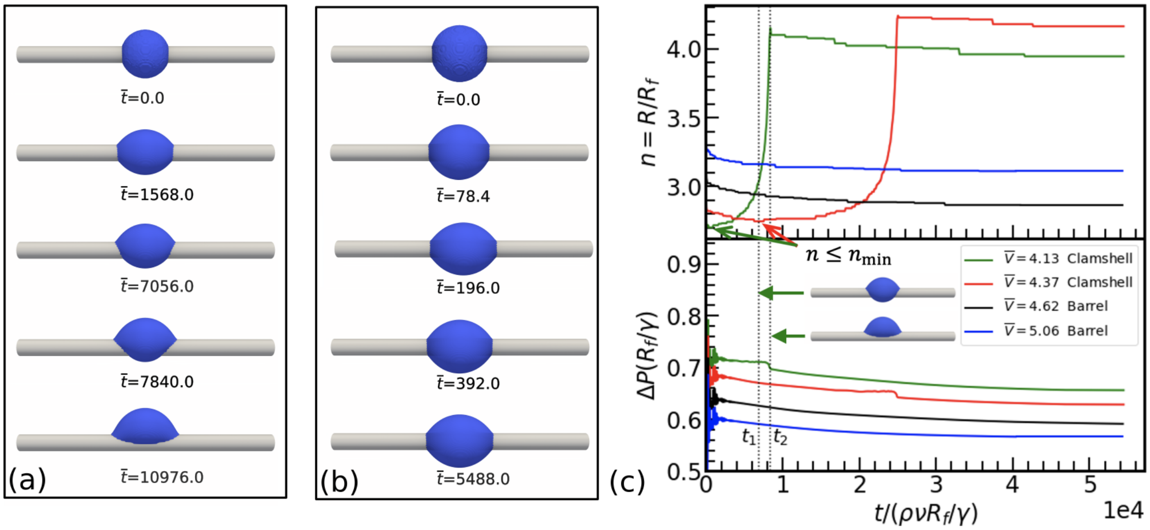

Figure 6.8: Simulation snapshots of the time evolution of droplets shape using wrapping around initial configuration. (a) Transition from a barrel drop to a clam-shell drop. Drop volume and fiber contact angle are $\overline{V}$ = 4.13, θ = 49.5. (b) The spherical drop evolves into a barrel-shaped drop for $\overline{V}$ = 5.06. The right panel (c) shows the time evolution of reduced thickness and the Laplace pressure of the droplet. The inserted images show the roll-up process of droplet with volume $\overline{V}$ = 4.13 at time t_1 and t_2.

To explain the roll-up process, we plot the corresponding time evolution of reduced thickness n and reduced Laplace pressure $\Delta P(R_f/\gamma)$ in Fig. 6.8 (c). Due to the spreading of droplet, n decreases in the early stage. For the relatively small droplets ($\overline{V}$ = 4.13 and

4.37), n becomes less than the minimum value $n_{\text{min}} = 2.71$ determined from Eq. (6.18) at some moment, indicating that the inflection point vanishes in the profile of a barrel drop. Therefore, it becomes unstable and starts moving off the fiber, which results in the increase of n. At the bottom of the fiber, thickness of liquid film reduces and the film breaks in the time interval between t_1 and t_2, as illustrated in Fig. 6.8 (c). We notice the sudden change in Laplace pressure due to the liquid film breakup. Once it approaches a clam-shell conformation, there is a small reduction in n during the relaxation towards equilibrium.

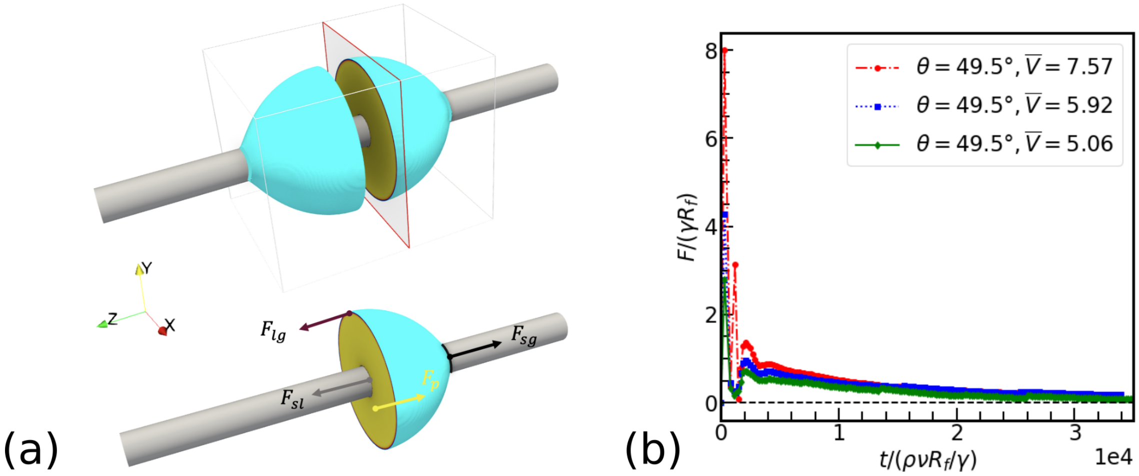

Figure 6.9: (a) Schematic for the free body diagram analysis. The barrel droplet is mirror symmetric with respect to plane $z = 0$ with the z-axis parallel to the fiber axis. By making an imaginary cut at the droplet symmetric plane perpendicularly to the fiber axis, one part of the droplet is replaced by an equivalent system of forces acting on the droplet cross-section at the cut. (b) Time evolution of the total force acting on the cut-plane for droplet of volume $\overline{V} = 7.57$, 5.92 and 5.06.

The equilibration towards a barrel shape can also be illustrated by the force balance analysis. Fig. 6.9 (a) shows the free body diagram for a barrel drop on a fiber. We can make an imaginary cut at the droplet center perpendicularly to the fiber, and replace one part of the droplet with the equivalent forces acting along the z-axis. Based on the free body diagram in Fig. 6.9 (a), the total force F in z-direction can be described as,

$$F = F_{lg} + F_{sl} - F_p - F_{sg}, \tag{6.19}$$

where $F_p = \int_A \Delta P dA$ is the pressure resultant acting on the cross-section area enclosed by the fiber and drop surface. Here, $\Delta P = P_{\text{in}} - P_{\text{out}}$ is the pressure difference between each facets of area dA inside the drop and the pressure outside the drop. $F_{lg} = \gamma P_d$ is the force due to the surface tension at the droplet surface, where $P_d = 2\pi R_d$ is the drop perimeter. $F_{sl} = \gamma_{sl} P_f$ is the force due to surface tension γ_{sl} at the solid/liquid interface, where $P_f = 2\pi R_f$ is the fiber perimeter. $F_{sg} = \gamma_{sg} P_f$ is the force due to surface tension γ_{sg} at the solid/gas interface. We can calculate $F_{sl} - F_{sg} = -\gamma \cos\theta P_f$ from Young's equation. Thus, Eq. (6.19) is rewritten as:

$$F = \gamma(P_d - \cos\theta P_f) - \int_A \Delta P dA. \tag{6.20}$$

Fig. 6.9(b) shows the transient net force calculated from Eq. (6.20). The force evolution exhibits fast rise to a maxima in the early stage, followed by a long, gradual decrease to zero. The large force corresponds to the quick deformation of droplet in the early stage. As is evident from Fig. 6.9(b), as the drop volume increases, the magnitude of force also increases.

6.3.4 Transition from clam-shell to barrel-shaped drop

We next consider the final shape of the drop when a spherical drop is deposited on fiber. The fiber contact angle θ and drop volume $\overline{V}$ are varied in the simulation. In Fig. 6.10, the fiber contact angle is 24.5°. Inspection of the final shape of the drop reveals that both barrel-shaped drop and clam-shell can be reached, as illustrated in Fig. 6.10 (a) and (b). The time evolution of drop shape shows a rapid deformation of the menisci driven by the excess pressure in the initial stage, followed by the downwards motion of the liquid. This

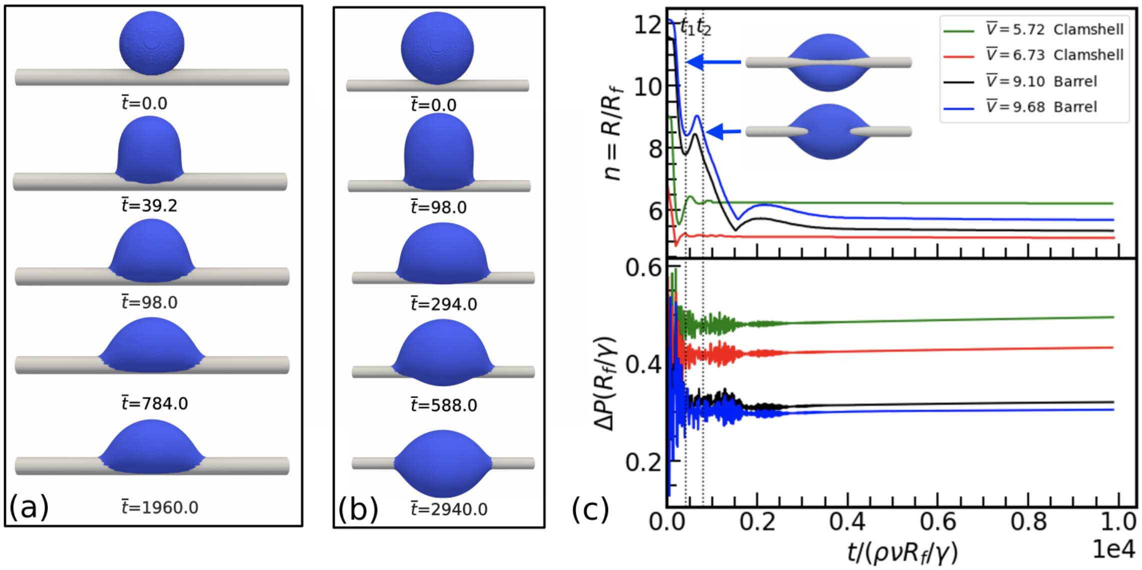

Figure 6.10: Simulation snapshots of the time evolution of droplets shape using sitting-on initial configuration. (a) The spherical drop evolves into a clam-shell for $\overline{V} = 5.72$. (b) Transition from the clam-shell to barrel drop. Drop volume and fiber contact angle are $\overline{V} = 9.68$, $\theta = 24.5$. The right panel (c) shows the time evolution of reduced thickness and the Laplace pressure of the droplet. The inserted images are the bottom view of drop-on-fiber at time t_1 and t_2 for $\overline{V} = 9.68$.

is illustrated by a decrease of the reduced thickness n and variation of Laplace excess pressure as shown in Fig. 6.10 (c). For the relatively small droplets ($\overline{V} = 5.72$ and 6.73), the equilibrium state of clam-shell is reached. However, the larger droplets ($\overline{V} = 9.10$ and 9.68) can adopt the equilibrium barrel shape, as shown in Fig. 6.10 (b). The transition between conformations at $\bar{t} = 294.0$ and $\bar{t} = 588.0$ is of the most interest. The inserted images in Fig. 6.10 (c) are the bottom view of the droplet at t_1 and t_2, which shows that the contact lines separated by the fiber approach each other from the two sides. Eventually, the contact lines come together, and the droplet can fully wrap the fiber and evolve towards the axisymmetric barrel shape.

The similar clamshell-to-barrel transition can be observed in droplet deposition experiments. Fig. 6.11 shows the morphological transition on a fiber with advancing/receding contact angle of 35.3°/27.1° by increasing the volume of the droplet. During the time interval of 20 ~ 40s, the droplet volume exceeds the critical volume for clamshell-to-barrel transition. Therefore, the transition from clam-shell to barrel can be seen after t = 20s.

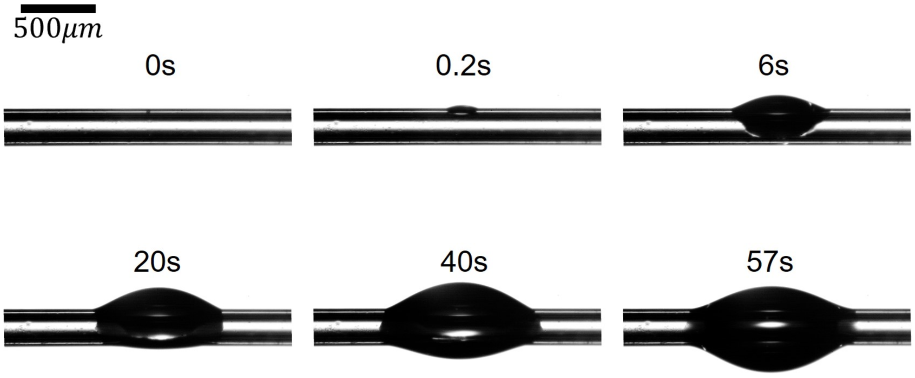

Figure 6.11: Snapshots of transition from clam-shell to barrel-shaped drop in the deposition experiment. Droplet volume increases gradually by depositing small droplets on the fiber. The advancing/receding contact angle of the fiber is 35.3°/27.1°. (Image courtesy of Yueming Sun)

To better understand the mechanism driving this morphological transition, we examined the instantaneous flow field of droplets with volume $\overline{V}$ = 9.68 and 5.72 in Fig. 6.12 (a) and (b), respectively. Fig. 6.12 (a) and (b) show the velocity field in xy plane, perpendicular to the fiber axis z. In the initial stage, droplet spreads along fiber axis (z direction) driven by capillary pressure, resulting in the motion of fluid particles towards the fiber. At the second stage, the internal flow in the region near the top of droplet moves changes direction and particles move upwards. While the contact line connects at the bottom for the larger droplet ($\overline{V}$ = 9.68), leading to the net downward velocity of the droplet. However, for the smaller droplet ($\overline{V}$ = 5.72), the magnitude of downward velocity is relatively small and the contact lines do not meet at the bottom. Therefore, we observed the net upward velocity at the second stage ($\bar{t}$ = 294.0) in Fig. 6.12 (b). Finally, when the droplet is in equilibrium, the velocity vanishes everywhere, except for small currents near the interface, which is the spurious currents in the multi-phase lattice Boltzmann model.

Figure 6.12: Instantaneous flow field in the xy plane of mirror symmetry for (a) transition from clam-shell to barrel drop with volume $\overline{V}$ = 9.68, (b) clam-shell drop remains in its original shape for $\overline{V}$ = 5.72. The drop shape is overlaid with the flow field.

6.3.5 Morphology diagram

To determine the critical condition for transitions between the barrel and clam-shell droplets, in Fig. 6.13 (a) and (b) we summarized the simulation results in the parameter space of reduced thickness n and contact angle θ. In Fig. 6.13(a), we decreased the droplet volume at a fixed contact angle, until it crossed the critical volume and the droplet spontaneously adopts a clam-shell shape. Fig. 6.13(c) shows the corresponding volume change. As the volume decreases, the reduced thickness n decreases until a critical value, below which the clam-shell is obtained. The critical value of n increases with contact angle. The polynomial curve fitting between critical n and contact angle gives the boundary below which no barrel drop can be found when we start from a pierced sphere. We further compared the phase boundary evaluated from LB simulation with fiber coating experiments. Due to the Plateau–Rayleigh instability, the barrel-shaped and clam-shell drops are formed from the liquid film. The morphological transition starts with the axisymmetric conformation, and is driven by the same mechanism as barrel-to-clamshell transition in LB simulation. Therefore, the critical value of n shows good agreement between experiments and simulation, both aligned with the inflection condition in Eq. (6.18). The critical volume $V^{1/3}/R_f$ for barrel-to-clamshell transition is indicated by the curve fitting in Fig. 6.13 (c). The limited condition of spherical drop is considered in Fig. 6.13 (a). If the barrel drop adopts the spherical surface for a given contact angle, the reduced thickness can be evaluated from the geometrical relation as,

$$n = \frac{1}{\cos\theta}. \tag{6.21}$$

The drop shape is no longer symmetric with respect to fiber axis below this value, thus determining the absolute minimum of n, shown as the dotted line in Fig. 6.13 (a).

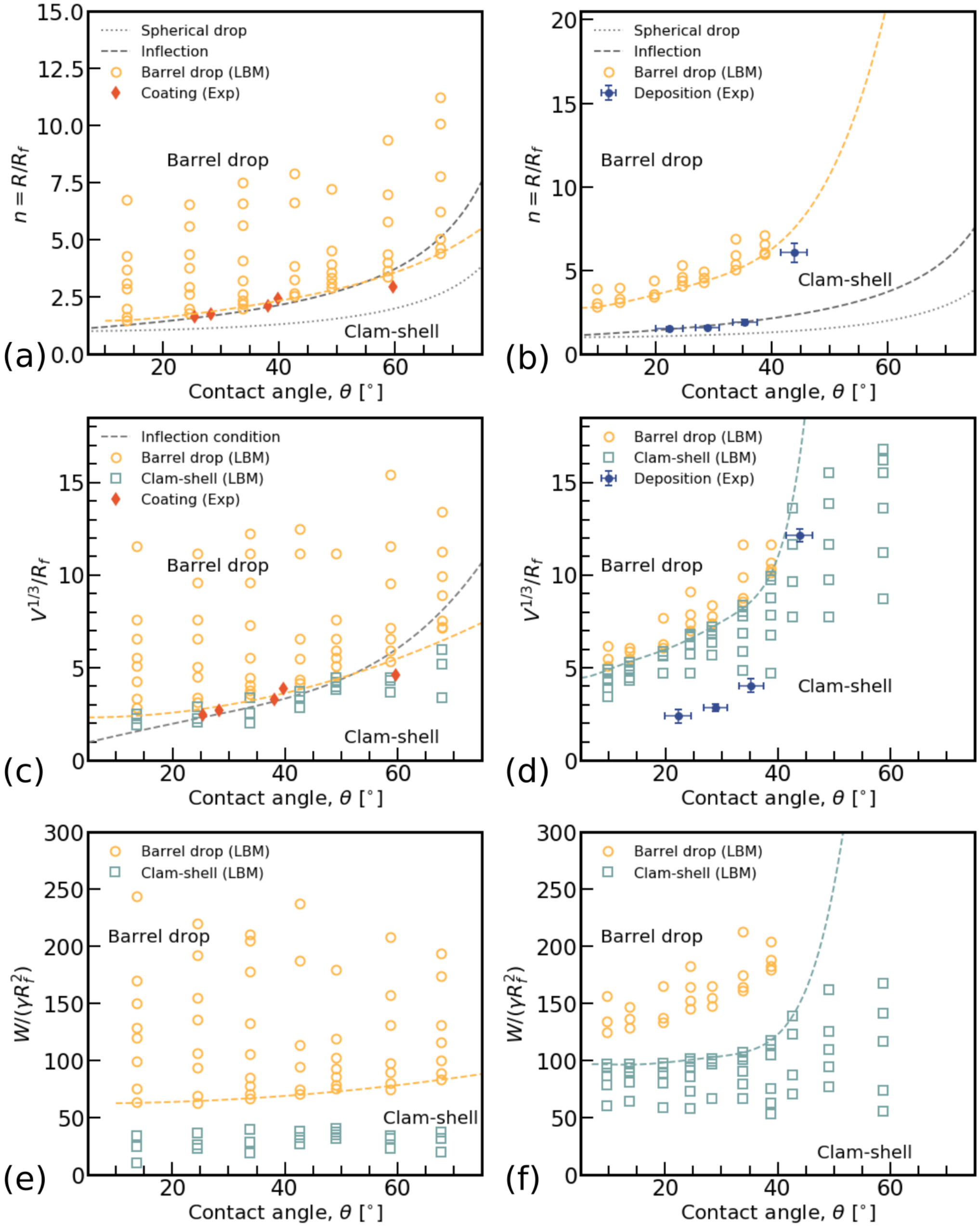

Figure 6.13: The initial configuration of (a, c) pierced spherical drop and (b, d) deposited spherical drop gives the contact angle, critical reduced thickness n, and droplet volume $V^{1/3}/R_f$ at which a change of conformation of a drop occurs. The symbol □ and ○ denote clam-shell and barrel drop determined from LB simulation. ♦ denotes the critical n and volume for barrel-to-clamshell transition determined in fiber coating experiments. ● denotes the critical n and volume for clamshell-to-barrel transition determined in droplet deposition experiments. The dashed line is inflection condition and the dotted line shows the condition when a barrel drop becomes spherical. (e) and (f) The adhesion energy of equilibrium shape using a initial state of pierced spherical drop and deposited spherical drop.

We next focused on the critical condition for clamshell-to-barrel transition in Fig. 6.13 (b) and (d). We placed spherical droplets on a fiber and varied the drop volume incrementally at a given contact angle, until the drop transforms into a barrel-shaped drop. As shown in Fig. 6.13 (b) and (d), the phase boundary above which no clam-shell can be found is determined from polynomial curve fitting. We noticed that the phase boundary does not follow the inflection condition as in Fig. 6.13 (a), which can be explained by the different mechanism between clamshell-to-barrel and barrel-to-clamshell transition. The critical n increases significantly with contact angle, so that no barrel drop can be observed for contact angle larger than 40°. Droplet deposition experiment in Fig. 6.11 shows a similar transition behavior from clam-shell to barrel drop. The experimental results also give a dramatic increase of critical n at $\theta = 43.8°$, and no barrel drop can exist beyond this contact angle. However, the critical value of n is much lower than that determined from simulation for smaller contact angle ($\theta < 40°$). One possible reason for this deviation is that viscosity ratio of the two phases are chosen to be 1 in the LB simulation, significantly different from that of experiments. The speed of contact line motion is affected by the viscosity ratio of the two fluids, and might have an influence on the coalescence of interface at the bottom of fiber, as illustrated in the previous section. The effect of viscosity ratio on the dynamics of morphological transition will be investigated in the future work.

Optimizing the collection efficiency of aerosol droplets by fibers has been the objective for many researchers and engineers. The morphology adopted by droplets in the fibrous mats is a key factor for capturing the droplets. The three-phase contact line and contact area of the droplet is enhanced for the barrel shape configuration and so as the adhesion between hanging droplets and the fiber, whereas the clam-shell configuration is undesirable due to the smaller adhesion. The adhesion energy of the droplet-fiber system can be expressed as

$$W = (\gamma_{sl} - \gamma_{sg} - \gamma_{lg})A_{sl}, \tag{6.22}$$

where γ_{sl}, γ_{sg} and γ_{lg} are the interfacial tension of solid-liquid, solid-gas and liquid-gas interface, and A_{sl} is the interfacial area between solid and liquid. The above expression can be rewritten in the dimensionless form as

$$\frac{W}{\gamma R_f^2} = \frac{A_{sl}}{R_f^2}(1+\cos\theta). \tag{6.23}$$

Here, we calculated the interfacial area A_{sl} for both barrel drop and clam-shell morphology by extracting the $\phi = 0$ isosurface, and then integrating the lattice data over a cylindrical clip plane. Fig. 6.13 (e) and (f) show the dependency of adhesion energy on contact angle using the two initial configurations. The critical value that separates barrel and clam-shell region is specified by the dashed line. As expected, the adhesion energy of barrel drop is higher than that of clam-shell, and increases with drop volume. For the initial configuration of deposited spherical drop, we can observe a gap between clam-shell and barrel drop region. The gap expands for larger fiber contact angle, implying that higher external energy is required to transform from clam-shell into the barrel shaped drop. From this point, a high magnitude of adhesion energy is preferred since it indicates a better resistance of droplet detachment from fiber surface. This measurement provides new insights into the design of fibrous filter in terms of the collection efficiency of a single fiber. During the filtration of aerosol droplets, the liquid volume increases due to the coalescence and accumulation of small droplets on fiber surface, therefore we can expect the clamshell-to-barrel transition. And higher contact angle is favored because the adhesion energy of barrel drop is much larger once the clamshell-to-barrel transition happens. Since this transition cannot be observed for larger contact angle ($\theta > 45°$) without external forces, a contact angle $\theta \approx 40°$ would be the optimal choice.

As shown in Fig. 6.13 (c) and (d), the droplet morphology changes monotonically with volume, so we combined the simulation results from these two plots in the morphology

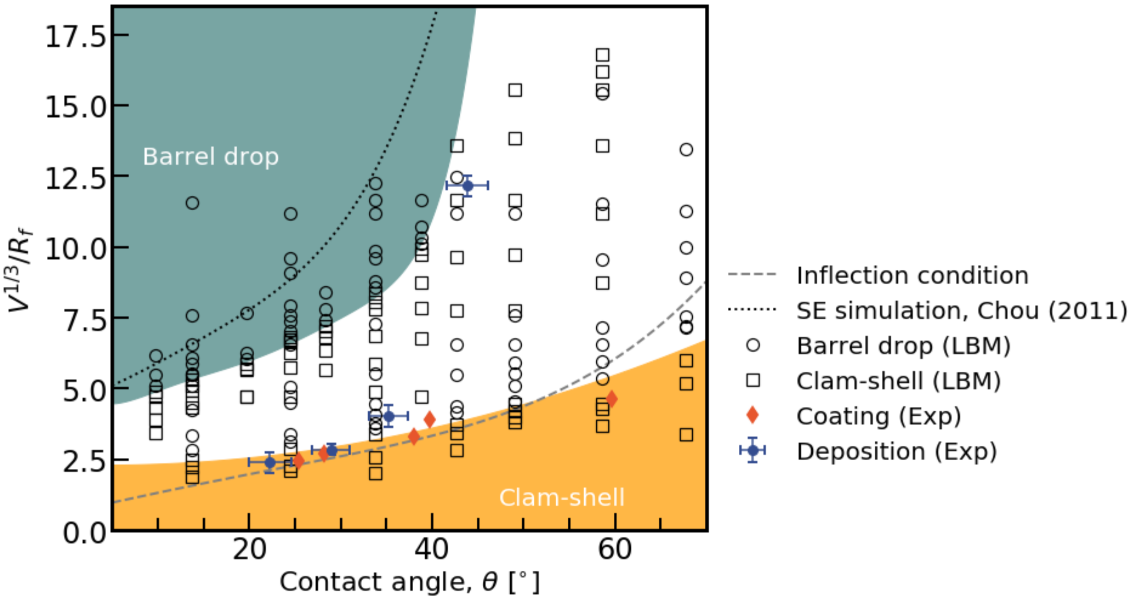

Figure 6.14: Morphology diagram of drop on a fiber in the parameter space of drop volume and contact angle.

diagram in Fig. 6.14, using the dimensionless droplet volume and contact angle as the parameters. The droplet volume is a parameter that can be easily determined in experiments, and allows us to predict the equilibrium configuration on a fiber. The final equilibrium shapes observed through the simulations are indicated by symbols (□ for clam-shell, ○ for barrel drop). The morphology diagram can be divided into three regions: clam-shell only, barrel drop only and the coexistence region between clam-shell and barrel drop. In the clam-shell only region (yellow shaded region), only clam-shell droplets can exist. In the barrel only region (green shaded region), only barrel drop can be found. In the coexistence region, both barrel drop and clam-shell can exist, depending on the initial configuration. The results from coating experiments are presented and show agreement with LB simulation in terms of the phase boundary of clam-shell only region. The sharp increase in the boundary of barrel drop region indicates that the clam-shell drop on a fiber with large contact angle tends to remain in its original shape when its volume is gradually increasing.

The boundary between clam-shell only and coexistence region determined by Chou et al. [212] follows the inflection condition, and is very close to our LB simulation and experimental results. Surface Evolver (SE) is usually used for solving the static equilibrium fluid interface. While the MCMP lattice Boltzmann model solves the multi-phase fluid dynamics equations, and the fluid interface reaches a steady state. The agreement in the phase boundary determined using these two approaches suggests that the barrel-to-clamshell transition is not time-dependent and only driven by energy minimization. However, the boundary between barrel only and coexistence region determined using SE simulation (dotted line) is higher than that of LB simulation and deposition experiment. As we described in the previous section, the three-phase contact line motion is critical for clamshell-to-barrel transition, which is not taken into account in SE simulations.

6.4 Conclusions

In this chapter, we performed the numerical simulation of droplets interaction with a fiber using multi-component lattice Boltzmann methods and compared the results to analytical model and experimental study. We have mainly focused on the morphological transition of droplets in the absence of gravity. Droplets on a fiber can take the axisymmetric barrel shape for the case of larger volume and small contact angle. In contrast to this case, non-axisymmetric clam-shell shape is preferred when the droplet volume is small or contact angle is large.

To understand the criterion of transition between the two morphologies, we probed two different initial drop conformations: a spherical drop pierced by a fiber and a spherical drop deposited on a fiber. In the first case, the barrel-to-clamshell transition is found by decreasing the drop volume gradually. The roll-up process observed in simulations is analogous to the formation of clam-shell drop from liquid film in the fiber coating experiments. On the other hand, the clamshell-to-barrel transition is simulated by placing a spherical drop on a fiber.

Although contact angle hysteresis is not considered in the simulations, the profile of the barrel-shaped drop obtained from simulations shows agreement with experiments for the given advancing contact angle, thus validate the accuracy of LB simulations. The agreement of critical condition for morphological transitions supports the physical model of inflection condition. Herein, we developed an integrated experimental, analytical and numerical protocol to probe wetting behavior on fibers. Through the analysis of adhesion energy and construction of morphological diagram, the stable region of barrel and clamshell droplet is determined and can provide guidance to the fibrous filter design in terms of the fiber surface wettability.

CHAPTER 7

CONCLUSION REMARKS AND FUTURE WORK

This thesis sought to contribute to the design of fibrous materials in engineering applications. A computational framework to characterize the transport and wetting properties of fibrous media is presented.

This study starts with random fiber network reconstruction, characterization of pore network. We utilized an efficient algorithm to extract the pore network from both ordered and disordered fibrous media to investigate the relation between the structure properties and flow behavior. The selected REV size for the inhomogeneous fibrous media is justified by statistical analysis of pore network properties. We have investigated the reliability of predicting pore size distribution of nonwovens from analytical model. The effect of mean pore size on effective pore space properties has been systematically studied.

Next, we present the lattice Boltzmann simulations of pressure driven flow in the generated fiber mats, where the permeability and tortuosity are measured based on the steady-state flow field in the porous media. The simulation data are fitted to semi-empirical relations for permeability and tortuosity as a function of porosity. This allows us to obtain the values of several empirical coefficients and scaling factors. The workflow employed in the current work is promising to obtain macroscopic transport properties when dealing with more complex porous media with polydisperse fiber diameter.

In Chapter 6, we have investigated the morphology transition of droplet deposited on a fiber using a pseudopotential lattice Boltzmann model. Quantitative comparison between simulated drop profile with experimental results and analytical description validates the accuracy of LBM simulation and demonstrates that LBM simulations can reproduce the morphological bistability reported by the Surface Evolver simulation. We constructed the complete morphology diagram in the parameter space of drop volume and fiber contact angle.

This dissertation sets up the fundamentals for further study of fibrous materials composed by complex-shaped fibers, including theoretical methodology and numerical simulation protocols. The framework developed in this study provides the design principles of fiber-based filters with controlled transport properties and wettability.

Future work

- The pseudopotential Shan-Chen model used in this work is limited to a viscosity ratio of about 5, preventing us from comparing the dynamics of wetting/dewetting phenomena with experiments for water/air system. A few strategies are available to achieve the large viscosity ratio. For example, using different equation of state to increase the density contrast, or using MRT for fluid mixtures with large viscosity ratio.

- The interface width in the Shan-Chen model sets the limitation of minimum droplet radius that can be simulated. We recommend the implementation of phase-field-based or free energy lattice Boltzmann method to overcome this drawback.

- The comparison between numerical simulation and experiments could be improved by introducing the contact angle hysteresis into the multiphase model.

- The Cassie state of droplet deposited on the topographically structured surface consisted of fiber arrays is of interest in the future.

REFERENCES

1. Schiller, U. D. & Wang, F. Multiscale simulation of transport phenomena in porous media: from toy models to materials models. *MRS Commun.* **8,** 358–371 (2018).
2. Wang, F. & Schiller, U. D. Computational characterization of nonwoven fibrous media: I. Pore-network extraction and morphological analysis. *Phys. Rev. Mater.* **4,** 083803 (2020).
3. Wang, F., Kumari, S. & Schiller, U. D. Computational characterization of nonwoven fibrous media. II. Analysis of microstructure effects on permeability and tortuosity. *Phys. Rev. Mater.* **4,** 083804 (2020).
4. Hao, L. & Cheng, P. Lattice Boltzmann simulations of water transport in gas diffusion layer of a polymer electrolyte membrane fuel cell. *J. Power Sources* **195,** 3870–3881 (2010).
5. Sinha, P. K., Mukherjee, P. P. & Wang, C.-Y. Impact of GDL structure and wettability on water management in polymer electrolyte fuel cells. *J. Mater. Chem.* **17,** 3089–3103 (2007).
6. Zhang, J. & Kwok, D. Y. A mean-field free energy lattice Boltzmann model for multicomponent fluids. *Eur. Phys. J. Spec. Top.* **171,** 45–53 (2009).
7. Bear, J. *Dynamics of Fluids in Porous Media* (Courier Corporation, 2013).
8. Blunt, M. J. *et al.* Pore-scale imaging and modelling. *Adv. Water Resour. 35th Year Anniversary Issue* **51,** 197–216 (2013).
9. Saha, P. K., Borgefors, G. & Sanniti di Baja, G. A survey on skeletonization algorithms and their applications. *Pattern Recognition Letters. Special Issue on Skeletonization and its Application* **76,** 3–12 (1, 2016).
10. Silin, D. & Patzek, T. Pore space morphology analysis using maximal inscribed spheres. *Physica A* **371,** 336–360 (2006).
11. Darcy, H. P. G. *Les Fontaines publiques de la ville de Dijon. Exposition et application des principes à suivre et des formules à employer dans les questions de distribution d'eau, etc* (V. Dalamont, 1856).
12. Bird, R. B., Stewart, W. E. & Lightfoot, E. N. *Transport Phenomena* (John Wiley & Sons, 11, 2006).
13. Kozeny, J. Ueber kapillare Leitung des Wassers im Boden. *Sitzungsber. Akad. Wiss. Wien* **136,** 271–306 (1927).

14. Carman, P. C. Fluid Flow through Granular Beds. *Trans. Inst. Chem. Eng.* **15,** 150–166 (1937).
15. Carman, P. C. Permeability of saturated sands, soils and clays. *The Journal of Agricultural Science* **29,** 262–273 (1939).
16. Lin, C. L. & Miller, J. Network analysis of filter cake pore structure by high resolution X-ray microtomography. *Chem. Eng. J.* **77,** 79–86 (2000).
17. Mchale, G., Newton, M. I. & Carroll, B. J. The Shape and Stability of Small Liquid Drops on Fibers. *Oil & Gas Science and Technology - Rev. IFP* **56,** 47–54 (2001).
18. Fukai, J. *et al.* Wetting effects on the spreading of a liquid droplet colliding with a flat surface: Experiment and modeling. *Phys. Fluids* **7,** 236–247 (1995).
19. Mao, T., Kuhn, D. C. S. & Tran, H. Spread and rebound of liquid droplets upon impact on flat surfaces. *AIChE Journal* **43,** 2169–2179 (1997).
20. Pasandideh-Fard, M., Qiao, Y. M., Chandra, S. & Mostaghimi, J. Capillary effects during droplet impact on a solid surface. *Phys. Fluids* **8,** 650–659 (1996).
21. Marengo, M., Antonini, C., Roisman, I. V. & Tropea, C. Drop collisions with simple and complex surfaces. *Current Opinion in Colloid & Interface Science* **16,** 292–302 (2011).
22. Gac, J. M. & Gradoń, L. Analytical investigation and numerical modeling of collisions between a droplet and a fiber. *J. Colloid Interface Sci.* **369,** 419–425 (2012).
23. Shi, Y., Tang, G. H. & Xia, H. H. Investigation of coalescence-induced droplet jumping on superhydrophobic surfaces and liquid condensate adhesion on slit and plain fins. *Int. J. Heat Mass Transfer* **88,** 445–455 (2015).
24. Kim, S.-G. & Kim, W. Drop impact on a fiber. *Phys. Fluids* **28,** 042001 (2016).
25. Banitabaei, S. A. & Amirfazli, A. Droplet impact onto a solid sphere: Effect of wettability and impact velocity. *Phys. Fluids* **29,** 062111 (2017).
26. Shan, X. & Chen, H. Simulation of nonideal gases and liquid-gas phase transitions by the lattice Boltzmann equation. *Phys. Rev. E* **49,** 2941–2948 (1994).
27. Yazdchi, K, Srivastava, S & Luding, S. *On the validity of the Carman-Kozeny equation in random fibrous media* in *PARTICLES II: proceedings of the II International Conference on Particle-Based Methods: fundamentals and applications* (2011), 264–273.
28. Adler, P. *Porous media: geometry and transports* (Elsevier, 2013).
29. Qayum, A. *et al.* Efficient decontamination of multi-component wastewater by hydrophilic electrospun PAN/AgBr/Ag fibrous membrane. *Chem. Eng. J.* **361,** 1255–1263 (1, 2019).
30. Kaur, S., Gopal, R., Ng, W. J., Ramakrishna, S. & Matsuura, T. Next-Generation Fibrous Media for Water Treatment. *MRS Bulletin* **33,** 21–26 (2008).

31. Kanawung, K. *et al.* Preparation and Characterization of Polycaprolactone/Diclofenac Sodium and Poly(vinyl alcohol)/Tetracycline Hydrochloride Fiber Mats and Their Release of the Model Drugs. *Polym. J.* **39,** 369–378 (2007).

32. Djilali, N. Computational modelling of polymer electrolyte membrane (PEM) fuel cells: Challenges and opportunities. *Energy. ECOS 05. 18th International Conference on Efficiency, Cost, Optimization, Simulation, and Environmental Impact of Energy Systems* **32,** 269–280 (2007).

33. Chapuis, O. *et al.* Two-phase flow and evaporation in model fibrous media: Application to the gas diffusion layer of PEM fuel cells. *J. Power Sources* **178,** 258–268 (15, 2008).

34. Ajmeri, J. R. & Ajmeri, C. J. in *Advances in Technical Nonwovens* (ed Kellie, G.) 227–256 (Woodhead Publishing, 1, 2016).

35. Stevens, M. M. & George, J. H. Exploring and Engineering the Cell Surface Interface. *Science* (18, 2005).

36. Yoon, K., Hsiao, B. S. & Chu, B. Functional nanofibers for environmental applications. *J. Mater. Chem.* **18,** 5326–5334 (2008).

37. Rajgarhia, S. S., Jana, S. C. & Chase, G. G. Separation of Water from Ultralow Sulfur Diesel Using Novel Polymer Nanofiber-Coated Glass Fiber Media. *ACS Appl. Mater. Interfaces* **8,** 21683–21690 (2016).

38. Chen, Z. *et al.* Permeation and optical properties of YAG:Er+ fiber membrane scintillators prepared by novel sol–gel/electrospinning method. *J. Sol-Gel Sci Technol* **83,** 35–43 (2017).

39. Ju, J. T. J., Boisvert, L. N. & Zuo, Y. Y. Face masks against COVID-19: Standards, efficacy, testing and decontamination methods. *Adv. Colloid Interface Sci.* **292,** 102435 (1, 2021).

40. Dbouk, T. & Drikakis, D. On respiratory droplets and face masks. *Phys. Fluids* **32,** 063303 (2020).

41. Smith, J. S. *et al.* Effect of various decontamination procedures on disposable N95 mask integrity and SARS-CoV-2 infectivity. *J. Clin. Transl. Sci.* **5** (2021).

42. Viscusi, D. J., Bergman, M. S., Eimer, B. C. & Shaffer, R. E. Evaluation of Five Decontamination Methods for Filtering Facepiece Respirators. *The Annals of Occupational Hygiene* **53,** 815–827 (1, 2009).

43. Farsi, D., Mofidi, M., Mahshidfar, B. & Hafezimoghadam, P. Consider the options; can decontamination and reuse be the answer to N95 respirator shortage in COVID-19 pandemic? *Frontiers in Emergency Medicine* **4,** e41–e41 (2020).

44. Saini, V., Sikri, K., Batra, S. D., Kalra, P. & Gautam, K. Development of a highly effective low-cost vaporized hydrogen peroxide-based method for disinfection of personal protective equipment for their selective reuse during pandemics. *Gut Pathog* **12,** 29 (19, 2020).

45. Aydin, O. *et al.* Performance of fabrics for home-made masks against the spread of COVID-19 through droplets: A quantitative mechanistic study. *Extreme Mech. Lett.* **40,** 100924 (2020).

46. Li, H.-J. *et al.* Development and characterization of anti-fouling cellulose hollow fiber UF membranes for oil–water separation. *J. Membr. Sci.* **279,** 328–335 (2006).

47. Shirazi, M. J. A., Bazgir, S., Shirazi, M. M. A. & Ramakrishna, S. Coalescing filtration of oily wastewaters: characterization and application of thermal treated, electrospun polystyrene filters. *Desalin. Water Treat.* **51,** 5974–5986 (2013).

48. Hao, L. & Cheng, P. Lattice Boltzmann simulations of liquid droplet dynamic behavior on a hydrophobic surface of a gas flow channel. *J. Power Sources* **190,** 435–446 (2009).

49. Okabe, H. & Blunt, M. J. Prediction of permeability for porous media reconstructed using multiple-point statistics. *Phys. Rev. E* **70,** 066135 (2004).

50. Boek, E. S. & Venturoli, M. Lattice-Boltzmann studies of fluid flow in porous media with realistic rock geometries. *Computers & Mathematics with Applications. Mesoscopic Methods in Engineering and Science* **59,** 2305–2314 (2010).

51. Zhao, T., Zhao, H., Ning, Z., Li, X. & Wang, Q. Permeability prediction of numerical reconstructed multiscale tight porous media using the representative elementary volume scale lattice Boltzmann method. *Int. J. Heat Mass Transfer* **118,** 368–377 (2018).

52. Nokken, M. R. & Hooton, R. D. Using pore parameters to estimate permeability or conductivity of concrete. *Mater. Struct.* **41,** 1 (2007).

53. Yazdchi, K., Srivastava, S. & Luding, S. Microstructural effects on the permeability of periodic fibrous porous media. *Int. J. Multiphase Flow* **37,** 956–966 (2011).

54. Huang, X. *et al.* Morphology and transport properties of fibrous porous media. *Powder Technol.* **283,** 618–626 (2015).

55. Liu, Y., Li, J., Sun, S. & Yu, B. Advances in Gaussian random field generation: a review. *Comput. Geosci.* **23,** 1011–1047 (2019).

56. Koponen, A., Ekman, A., Mattila, K., Al-Qararah, A. M. & Timonen, J. The Effect of Void Structure on the Permeability of Fibrous Networks. *Transp. Porous Media* **117,** 247–259 (2017).

57. Eshghinejadfard, A., Daróczy, L., Janiga, G. & Thévenin, D. Calculation of the permeability in porous media using the lattice Boltzmann method. *Int. J. Heat Fluid Flow* **62, Part A,** 93–103 (2016).

58. Schiller, U. D. & Kuksenok, O. in *Reviews in Computational Chemistry, Volume 31* 1–61 (John Wiley & Sons, Ltd, 2018).

59. Costa, A. Permeability-porosity relationship: A reexamination of the Kozeny-Carman equation based on a fractal pore-space geometry assumption. *Geophys. Res. Lett.* **33** (2006).

60. Nabovati, A., Llewellin, E. W. & Sousa, A. C. M. A general model for the permeability of fibrous porous media based on fluid flow simulations using the lattice Boltzmann method. *Composites, Part A* **40,** 860–869 (2009).

61. Berg, C. F. Permeability Description by Characteristic Length, Tortuosity, Constriction and Porosity. *Transp. Porous Media* **103,** 381–400 (2014).

62. Fatt, I. The Network Model of Porous Media. *Transactions of the AIME* **207,** 144–181 (1956).

63. Biswal, B., Held, R. J., Khanna, V., Wang, J. & Hilfer, R. Towards precise prediction of transport properties from synthetic computer tomography of reconstructed porous media. *Phys. Rev. E* **80,** 041301 (2009).

64. Roberts, S. A. *et al.* Insights Into Lithium-Ion Battery Degradation and Safety Mechanisms From Mesoscale Simulations Using Experimentally Reconstructed Mesostructures. *J. Electrochem. En. Conv. Stor.* **13,** 031005–031005–10 (2016).

65. Gueven, I., Frijters, S., Harting, J., Luding, S. & Steeb, H. Hydraulic properties of porous sintered glass bead systems. *Granular Matter* **19,** 28 (2017).

66. Ghaddar, C. K. On the permeability of unidirectional fibrous media: A parallel computational approach. *Phys. Fluids* **7,** 2563–2586 (1995).

67. Claeys, I. L. & Brady, J. F. Suspensions of prolate spheroids in Stokes flow. Part 2. Statistically homogeneous dispersions. *J. Fluid Mech.* **251,** 443–477 (1993).

68. Higdon, J. J. L. & Ford, G. D. Permeability of three-dimensional models of fibrous porous media. *J. Fluid Mech.* **308,** 341–361 (1996).

69. Rawal, A. Structural analysis of pore size distribution of nonwovens. *The Journal of The Textile Institute* **101,** 350–359 (2010).

70. Xu, B. Measurement of pore characteristics in nonwoven fabrics using image analysis. *Clothing Text. Res. J.* **14,** 81–88 (1996).

71. Jena, A. & Gupta, K. Liquid Extrusion Techniques for Pore Structure Evaluation of Nonwovens. *Int. Nonwovens J.* **os-12,** 1558925003os–1200313 (2003).

72. Hutten, I. M. *Handbook of nonwoven filter media* (Elsevier, 2007).

73. Faure, Y., Gourc, J. & Gendrin, P. in *Geosynthetics: Microstructure and Performance* (ed Peggs, I.) 102–102–18 (ASTM International, 1990).

74. Lombard, G., Rollin, A. & Wolff, C. Theoretical and Experimental Opening Sizes of Heat-Bonded Geotextiles. *Text. Res. J.* **59,** 208–217 (1989).

75. Dong, H. & Blunt, M. J. Pore-network extraction from micro-computerized-tomography images. *Phys. Rev. E* **80,** 036307 (2009).

76. Al-Kharusi, A. S. & Blunt, M. J. Network extraction from sandstone and carbonate pore space images. *Journal of Petroleum Science and Engineering* **56,** 219–231 (2007).

77. Thompson, K. E. *et al. Application of a New Grain-Based Reconstruction Algorithm to Microtomography Images for Quantitative Characterization and Flow Modeling* tech. rep. NRL/JA/7430-07-13 (NAVAL RESEARCH LAB STENNIS SPACE CENTER MS MARINE GEOACOUSTICS DIV, 2008).

78. Sheppard, A., Sok, R., Averdunk, H, Robins, V. & Ghous, A. *Analysis of rock microstructure using high-resolution X-ray tomography* in *Proceedings of the International Symposium of the Society of Core Analysts* (Society of Core Analysts, Trondheim, Norway, 2006), 1–12.

79. Virmani, D., Jain, N., Parikh, K. & Upadhyaya, S. Boundary Outlier Centroid Based Reduced Overlapping Image Segmentation. *Journal of Engineering Science & Technology Review* **11** (2018).

80. Zheng, T. *et al.* Research on distance transform and neural network lidar information sampling classification-based semantic segmentation of 2d indoor room maps. *Sensors* **21,** 1365 (2021).

81. Gostick, J. T. Versatile and efficient pore network extraction method using marker-based watershed segmentation. *Phys. Rev. E* **96,** 023307 (2017).

82. Aziz, H. & V. Tafreshi, H. Competing forces on a liquid bridge between parallel and orthogonal dissimilar fibers. *Soft Matter* **15,** 6967–6977 (2019).

83. Chen, X., Kornev, K. G., Kamath, Y. K. & Neimark, A. V. The Wicking Kinetics of Liquid Droplets into Yarns. *Text. Res. J.* **71,** 862–869 (2001).

84. Lukas, D. & Pan, N. Wetting of a fiber bundle in fibrous structures. *Polym. Compos.* **24,** 314–322 (2003).

85. Mullins, B. J., Agranovski, I. E., Braddock, R. D. & Ho, C. M. Effect of fiber orientation on fiber wetting processes. *J. Colloid Interface Sci.* **269,** 449–458 (2004).

86. Protiere, S., Duprat, C. & Stone, H. A. Wetting on two parallel fibers: drop to column transitions. *Soft Matter* **9,** 271–276 (2012).

87. Sauret, A., Boulogne, F., Soh, B., Dressaire, E. & Stone, H. A. Wetting morphologies on randomly oriented fibers. *Eur. Phys. J. E* **38,** 62 (2015).

88. Wu, X.-F., Bedarkar, A. & Vaynberg, K. A. Droplets wetting on filament rails: Surface energy and morphology transition. *J. Colloid Interface Sci.* **341,** 326–332 (2010).

89. Wu, X. F. & Dzenis, Y. A. Droplet on a fiber: geometrical shape and contact angle. *Acta Mech.* **185,** 215–225 (2006).

90. Eral, H. B., Manukyan, G. & Oh, J. M. Wetting of a Drop on a Sphere. *Langmuir* **27,** 5340–5346 (3, 2011).
91. Brinkmann, M. & Lipowsky, R. Wetting morphologies on substrates with striped surface domains. *J. Appl. Phys.* **92,** 4296–4306 (2002).
92. Zhang, C. & Kornev, K. G. Morphological transitions of drop configurations on ribbon-like fibers. *Surf. Innovations* **5,** 194–202 (2017).
93. Soulié, F., El Youssoufi, M. S., Cherblanc, F. & Saix, C. Capillary cohesion and mechanical strength of polydisperse granular materials. *Eur. Phys. J. E* **21,** 349–357 (1, 2006).
94. Farmer, T. P. & Bird, J. C. Asymmetric capillary bridges between contacting spheres. *J. Colloid Interface Sci.* **454,** 192–199 (2015).
95. Scheel, M. *et al.* Liquid distribution and cohesion in wet granular assemblies beyond the capillary bridge regime. *J. Phys.: Condens. Matter* **20,** 494236 (2008).
96. Scheel, M. *et al.* Morphological clues to wet granular pile stability. *Nat Mater* **7,** 189–193 (2008).
97. Semprebon, C., Scheel, M., Herminghaus, S., Seemann, R. & Brinkmann, M. Liquid morphologies and capillary forces between three spherical beads. *Phys. Rev. E* **94,** 012907 (2016).
98. Zhu, Y. *et al.* Dynamics of drop impact onto a solid sphere: spreading and retraction. *J. Fluid Mech.* **824** (2017).
99. Mitra, S. *et al.* On wetting characteristics of droplet on a spherical particle in film boiling regime. *Chem. Eng. Sci.* **149,** 181–203 (31, 2016).
100. Duprat, C., Protière, S., Beebe, A. Y. & Stone, H. A. Wetting of flexible fibre arrays. *Nature* **482,** 510–513 (2012).
101. Rukosuyev, M. V., Barannyk, O., Oshkai, P. & Jun, M. B. G. Design and application of nanoparticle coating system with decoupled spray generation and deposition control. *J. Coat Technol. Res.* **13,** 769–779 (1, 2016).
102. Kampa, D., Wurster, S., Buzengeiger, J., Meyer, J. & Kasper, G. Pressure drop and liquid transport through coalescence filter media used for oil mist filtration. *Int. J. Multiphase Flow* **58,** 313–324 (2014).
103. Princen, H. M. Capillary phenomena in assemblies of parallel cylinders: III. Liquid Columns between Horizontal Parallel Cylinders. *J. Colloid Interface Sci.* **34,** 171–184 (1970).
104. Carroll, B. J. The accurate measurement of contact angle, phase contact areas, drop volume, and Laplace excess pressure in drop-on-fiber systems. *J. Colloid Interface Sci.* **57,** 488–495 (1976).
105. Bedarkar, A., Wu, X.-F. & Vaynberg, A. Wetting of liquid droplets on two parallel filaments. *Appl. Surf. Sci.* **256,** 7260–7264 (2010).

106. McHale, G & Newton, M. I. Global geometry and the equilibrium shapes of liquid drops on fibers. *Colloids Surf., A* **206,** 79–86 (2002).

107. Lenz, P. Wetting Phenomena on Structured Surfaces. *Adv. Mater.* **11,** 1531–1534 (1999).

108. Gau, H., Herminghaus, S., Lenz, P. & Lipowsky, R. Liquid Morphologies on Structured Surfaces: From Microchannels to Microchips. *Science* (1, 1999).

109. Extrand, C. W., Moon, S. I., Hall, P. & Schmidt, D. Superwetting of Structured Surfaces. *Langmuir* **23,** 8882–8890 (1, 2007).

110. Pendyala, P., Kim, H. N., Ryu, Y.-S. & Yoon, E.-S. Time-Dependent Wetting Scenarios of a Water Droplet on Surface-Energy-Controlled Microcavity Structures with Functional Nanocoatings. *ACS Appl. Mater. Interfaces* **12,** 39881–39891 (2, 2020).

111. Lipowsky, R. Structured Surfaces and Morphological Wetting Transitions. *Interface Sci.* **9,** 105–115 (1, 2001).

112. Cai, T.-m., Jia, Z.-h., Yang, H.-n. & Wang, G. Investigation of Cassie-Wenzel Wetting transitions on microstructured surfaces. *Colloid Polym Sci* **294,** 833–840 (1, 2016).

113. Rahman, M. M., Lee, W., Iyer, A. & Williams, S. J. Viscous resistance in drop coalescence. *Phys. Fluids* **31,** 012104 (2019).

114. Ruiz-Gutiérrez, & Ledesma-Aguilar, R. Lattice-Boltzmann simulations of the dynamics of liquid barrels. *J. Phys.: Condens. Matter* **32,** 214007 (2020).

115. Ruiz-Gutiérrez, Semprebon, C., McHale, G. & Ledesma-Aguilar, R. Statics and dynamics of liquid barrels in wedge geometries. *J. Fluid Mech.* **842,** 26–57 (2018).

116. Dokowicz, M. & Nowicki, W. Morphological Transitions of Droplets Wetting a Series of Triangular Grooves. *Langmuir* **32,** 7259–7264 (2016).

117. Dokowicz, M. & Nowicki, W. Morphological hysteresis of droplets wetting a series of triangular grooves. *Int. J. Heat Mass Transfer* **115,** 131–137 (2017).

118. Ferraro, D. *et al.* Morphological Transitions of Droplets Wetting Rectangular Domains. *Langmuir* **28,** 13919–13923 (2012).

119. Sartori, P. *et al.* Morphological Transitions of Water Channels Induced by Vertical Vibrations. *Langmuir* **34,** 12882–12888 (2018).

120. Yu, D. I. *et al.* Wetting state on hydrophilic and hydrophobic micro-textured surfaces: Thermodynamic analysis and X-ray visualization. *Appl. Phys. Lett.* **106,** 171602 (27, 2015).

121. Zheng, Q.-S., Yu, Y. & Zhao, Z.-H. Effects of Hydraulic Pressure on the Stability and Transition of Wetting Modes of Superhydrophobic Surfaces. *Langmuir* **21,** 12207–12212 (1, 2005).

122. Han, Z., Tay, B., Tan, C., Shakerzadeh, M. & Ostrikov, K. K. Electrowetting Control of Cassie-to-Wenzel Transitions in Superhydrophobic Carbon Nanotube-Based Nanocomposites. *ACS Nano* **3,** 3031–3036 (27, 2009).

123. Ren, W. Wetting Transition on Patterned Surfaces: Transition States and Energy Barriers. *Langmuir* **30,** 2879–2885 (2014).

124. Fang, W., Guo, H.-Y., Li, B., Li, Q. & Feng, X.-Q. Revisiting the Critical Condition for the Cassie–Wenzel Transition on Micropillar-Structured Surfaces. *Langmuir* **34,** 3838–3844 (3, 2018).

125. Lundgren, M., Allan, N. L. & Cosgrove, T. Modeling of Wetting:. A Study of Nanowetting at Rough and Heterogeneous Surfaces. *Langmuir* **23,** 1187–1194 (1, 2007).

126. Koishi, T., Yasuoka, K., Fujikawa, S., Ebisuzaki, T. & Zeng, X. C. Coexistence and transition between Cassie and Wenzel state on pillared hydrophobic surface. *PNAS* **106,** 8435–8440 (26, 2009).

127. Luo, K., Kuittu, M.-P., Tong, C., Majaniemi, S. & Ala-Nissila, T. Phase-field modeling of wetting on structured surfaces. *J. Chem. Phys.* **123,** 194702 (15, 2005).

128. Chamakos, N. T., Sema, D. G. & Papathanasiou, A. G. Progress in Modeling Wetting Phenomena on Structured Substrates. *Arch Computat Methods Eng* **28,** 1647–1666 (1, 2021).

129. Wolf, F. G., Santos, L. O. E. d. & Philippi, P. C. Modeling and simulation of the fluid–solid interaction in wetting. *J. Stat. Mech.* **2009,** P06008 (2009).

130. Hyväluoma, J., Koponen, A., Raiskinmäki, P. & Timonen, J. Droplets on inclined rough surfaces. *Eur. Phys. J. E* **23,** 289–293 (2007).

131. Virozub, A., Haimovich, N. & Brandon, S. Three-Dimensional Simulations of Liquid Bridges between Two Cylinders: Forces, Energies, and Torques. *Langmuir* **25,** 12837–12842 (2009).

132. Keis, K., Kornev, K. G., Kamath, Y. K. & Neimark, A. V. Towards fiber-based micro- and nanofluidics. *Nanoengineered nanofibrous materials* **169,** 175 (2004).

133. McNamara, G. R. & Zanetti, G. Use of the Boltzmann Equation to Simulate Lattice-Gas Automata. *Phys. Rev. Lett.* **61,** 2332–2335 (14, 1988).

134. Bhatnagar, P. L., Gross, E. P. & Krook, M. A Model for Collision Processes in Gases. I. Small Amplitude Processes in Charged and Neutral One-Component Systems. *Phys. Rev.* **94,** 511–525 (1, 1954).

135. Hardy, J., Pomeau, Y. & de Pazzis, O. Time evolution of a two-dimensional model system. I. Invariant states and time correlation functions. *J. Math. Phys.* **14,** 1746–1759 (1, 1973).

136. Krüger, T. *et al.* The lattice Boltzmann method. *Springer International Publishing* **10** (2017).

137. Qian, Y. H., D'Humières, D. & Lallemand, P. Lattice BGK Models for Navier-Stokes Equation. *Europhys. Lett.* **17,** 479 (1992).

138. Ubertini, S, Asinari, P & Succi, S. Three ways to lattice Boltzmann: a unified time-marching picture. *Phys. Rev. E* **81,** 016311 (2010).

139. Dominique d'Humières. Multiple–relaxation–time lattice Boltzmann models in three dimensions. *Philos. Trans. R. Soc. London,* **360,** 437–451 (2002).

140. He, X., Zou, Q., Luo, L.-S. & Dembo, M. Analytic solutions of simple flows and analysis of nonslip boundary conditions for the lattice Boltzmann BGK model. *J. Stat. Phys.* **87,** 115–136 (1997).

141. Kim, I. C. Second order bounce back boundary condition for the Latice Boltzmann fluid simulation. *KSME international journal* **14,** 84–92 (2000).

142. Zou, Q. & He, X. On pressure and velocity boundary conditions for the lattice Boltzmann BGK model. *Phys. Fluids* **9,** 1591–1598 (1997).

143. Hecht, M. & Harting, J. Implementation of on-site velocity boundary conditions for D3Q19 lattice Boltzmann. *J. Stat. Mech: Theory Exp.* **2010,** P01018 (2010).

144. Sukop, M. C. & Thorne, D. T. in *Lattice Boltzmann Modeling: An Introduction for Geoscientists and Engineers* (Springer Berlin Heidelberg, 2006).

145. Pan, C., Prins, J. F. & Miller, C. T. A high-performance lattice Boltzmann implementation to model flow in porous media. *Comput. Phys. Commun.* **158,** 89–105 (2004).

146. Mukherjee, P. P., Wang, C.-Y. & Kang, Q. Mesoscopic modeling of two-phase behavior and flooding phenomena in polymer electrolyte fuel cells. *Electrochimica Acta* **54,** 6861–6875 (2009).

147. Lee, S. G., Jeon, D. H., Kim, B. M., Kang, J. H. & Kim, C.-J. Lattice Boltzmann Simulation for Electrolyte Transport in Porous Electrode of Lithium Ion Batteries. *J. Electrochem. Soc.* **160,** H258–H265 (2013).

148. Liu, H. *et al.* Multiphase lattice Boltzmann simulations for porous media applications – a review. *arXiv:1404.7523 [physics]* (2014).

149. Jinuntuya, F., Whiteley, M., Chen, R. & Fly, A. The effects of gas diffusion layers structure on water transportation using X-ray computed tomography based Lattice Boltzmann method. *J. Power Sources* **378,** 53–65 (2018).

150. Kamp, J., Villwock, J. & Kraume, M. Drop coalescence in technical liquid/liquid applications: a review on experimental techniques and modeling approaches. *Rev. Chem. Eng.* **33,** 1–47 (2016).

151. Shan, X. & Chen, H. Lattice Boltzmann model for simulating flows with multiple phases and components. *Phys. Rev. E* **47,** 1815–1819 (1993).

152. Swift, M. R., Osborn, W. R. & Yeomans, J. M. Lattice Boltzmann Simulation of Nonideal Fluids. *Phys. Rev. Lett.* **75,** 830–833 (1995).

153. He, X., Chen, S. & Zhang, R. A Lattice Boltzmann Scheme for Incompressible Multiphase Flow and Its Application in Simulation of Rayleigh–Taylor Instability. *J. Comput. Phys.* **152,** 642–663 (1999).

154. Lee, T. & Fischer, P. F. Eliminating parasitic currents in the lattice Boltzmann equation method for nonideal gases. *Phys. Rev. E* **74,** 046709 (2006).

155. Gunstensen, A. K., Rothman, D. H., Zaleski, S. & Zanetti, G. Lattice Boltzmann model of immiscible fluids. *Phys. Rev. A* **43,** 4320–4327 (1991).

156. Dupin, M. M., Halliday, I. & Care, C. M. Multi-component lattice Boltzmann equation for mesoscale blood flow. *J. Phys. A: Math. Gen.* **36,** 8517–8534 (2003).

157. Rothman, D. H. & Keller, J. M. Immiscible cellular-automaton fluids. *J. Stat. Phys.* **52,** 1119–1127 (1988).

158. Ahrenholz, B. *et al.* Prediction of capillary hysteresis in a porous material using lattice-Boltzmann methods and comparison to experimental data and a morphological pore network model. *Advances in Water Resources. Quantitative links between porous media structures and flow behavior across scales* **31,** 1151–1173 (1, 2008).

159. Huang, H., Sukop, M. & Lu, X. Multiphase lattice Boltzmann methods: Theory and application (2015).

160. Sbragaglia, M. *et al.* Generalized lattice Boltzmann method with multirange pseudopotential. *Phys. Rev. E* **75,** 026702 (2007).

161. Benzi, R., Biferale, L., Sbragaglia, M., Succi, S. & Toschi, F. Mesoscopic modeling of a two-phase flow in the presence of boundaries: The contact angle. *Phys. Rev. E* **74,** 021509 (2006).

162. González-Segredo, N., Nekovee, M. & Coveney, P. V. Three-dimensional lattice-Boltzmann simulations of critical spinodal decomposition in binary immiscible fluids. *Phys. Rev. E* **67,** 046304 (2003).

163. Schmieschek, S. & Harting, J. Contact angle determination in multicomponent lattice Boltzmann simulations. *Communications in Computational Physics* **9,** 1165–1178 (2011).

164. Huang, H., Thorne, D. T., Schaap, M. G. & Sukop, M. C. Proposed approximation for contact angles in Shan-and-Chen-type multicomponent multiphase lattice Boltzmann models. *Phys. Rev. E* **76,** 066701 (2007).

165. Chen, L., Kang, Q., Mu, Y., He, Y.-L. & Tao, W.-Q. A critical review of the pseudopotential multiphase lattice Boltzmann model: Methods and applications. *Int. J. Heat Mass Transfer* **76,** 210–236 (2014).

166. Pan, C., Hilpert, M. & Miller, C. T. Lattice-Boltzmann simulation of two-phase flow in porous media. *Water Resour. Res.* **40,** W01501 (2004).

167. Snoeijer, J. H. & Andreotti, B. Moving contact lines: scales, regimes, and dynamical transitions. *Annu. Rev. Fluid Mech.* **45,** 269–292 (2013).

168. Cho, H., Jeong, N. & Sung, H. J. Permeability of microscale fibrous porous media using the lattice Boltzmann method. *Int. J. Heat Fluid Flow* **44,** 435–443 (2013).

169. Markicevic, B. & Papathanasiou, T. D. On the apparent permeability of regular arrays of nonuniform fibers. *Phys. Fluids* **14,** 3347–3349 (2002).

170. Math2Market. *GeoDict* `https://www.math2market.com/Solutions/aboutGD.php`.

171. Gostick, J. *et al.* OpenPNM: A Pore Network Modeling Package. *Computing in Science Engineering* **18,** 60–74 (2016).

172. Weissberg, H. L. Effective Diffusion Coefficient in Porous Media. *J. Appl. Phys.* **34,** 2636–2639 (1963).

173. Mauret, E. & Renaud, M. Transport phenomena in multi-particle systems–l. Limits of applicability of capillary model in high voidage beds- application to fixed beds of fibers and fluidized beds of spheres. *Chem. Eng. Sci.* **52,** 1807–1817 (1997).

174. Bognitzki, M. *et al.* Nanostructured Fibers via Electrospinning. *Adv. Mater.* **13,** 70–72 (2001).

175. Megelski, S., Stephens, J. S., Chase, D. B. & Rabolt, J. F. Micro- and Nanostructured Surface Morphology on Electrospun Polymer Fibers. *Macromolecules* **35,** 8456–8466 (2002).

176. Li, D., Ouyang, G., McCann, J. T. & Xia, Y. Collecting Electrospun Nanofibers with Patterned Electrodes. *Nano Lett.* **5,** 913–916 (2005).

177. Shin, C. & Chase, G. G. The effect of wettability on drop attachment to glass rods. *J. Colloid Interface Sci.* **272,** 186–190 (2004).

178. Panatdasirisuk, W., Liao, Z., Vongsetskul, T. & Yang, S. Separation of Oil-in-Water Emulsions Using Hydrophilic Electrospun Membranes with Anisotropic Pores. *Langmuir* **33,** 5872–5878 (2017).

179. Chattopadhyay, S., Hatton, T. A. & Rutledge, G. C. Aerosol filtration using electrospun cellulose acetate fibers. *J Mater Sci* **51,** 204–217 (2016).

180. Agarwal, S., Wendorff, J. H. & Greiner, A. Use of electrospinning technique for biomedical applications. *Polymer* **49,** 5603–5621 (2008).

181. Koponen, A. *et al.* Permeability of Three-Dimensional Random Fiber Webs. *Phys. Rev. Lett.* **80,** 716–719 (1998).

182. Silberstein, M. N., Pai, C.-L., Rutledge, G. C. & Boyce, M. C. Elastic–plastic behavior of non-woven fibrous mats. *J. Mech. Phys. Solids* **60,** 295–318 (2012).

183. Pourdeyhimi, B., Mazé, B. & Tafreshi, H. V. Simulation and Analysis of Unbonded Nonwoven Fibrous Structures. *J. Eng. Fibers Fabr.* **1,** 155892500600100204 (2006).

184. Brun, E., Vicente, J., Topin, F., Occelli, R. & Clifton, M. J. Microstructure and Transport Properties of Cellular Materials: Representative Volume Element. *Adv. Eng. Mater.* **11,** 805–810 (2009).

185. `https://dx.doi.org/10.24433/CO.6709443.v1`.

186. Schmieschek, S. *et al.* LB3D: A parallel implementation of the Lattice-Boltzmann method for simulation of interacting amphiphilic fluids. *Comput. Phys. Commun.* **217,** 149–161 (2017).

187. Narváez, A., Zauner, T., Raischel, F., Hilfer, R. & Harting, J. Quantitative analysis of numerical estimates for the permeability of porous media from lattice-Boltzmann simulations. *J. Stat. Mech.* **2010,** P11026 (2010).

188. Narváez, A. & Harting, J. Evaluation of pressure boundary conditions for permeability calculations using the lattice-Boltzmann method. *Adv. Appl. Math. Mech.* **2,** 685–700 (2010).

189. Van der Graaf, S., Nisisako, T., Schroën, C. G. P. H., van der Sman, R. G. M. & Boom, R. M. Lattice Boltzmann Simulations of Droplet Formation in a T-Shaped Microchannel. *Langmuir* **22,** 4144–4152 (2006).

190. Patzek, T. W. & Silin, D. B. Shape factor and hydraulic conductance in noncircular capillaries. I. One-Phase Creeping Flow. *J. Colloid Interface Sci.* **236** (2000).

191. Pan, C., Luo, L.-S. & Miller, C. T. An evaluation of lattice Boltzmann schemes for porous medium flow simulation. *Computers & Fluids. Proceedings of the First International Conference for Mesoscopic Methods in Engineering and Science* **35,** 898–909 (2006).

192. Toschi, F. & Succi, S. Lattice Boltzmann method at finite Knudsen numbers. *EPL* **69,** 549 (2005).

193. Basak, P. Non-Darcy Flow and its Implications to Seepage Problems. *Journal of the Irrigation and Drainage Division* **103,** 459–473 (1977).

194. Gavin, L. *Pre-Darcy Flow: A Missing Piece of the Improved Oil Recovery Puzzle?* in (Society of Petroleum Engineers, 2004).

195. Matyka, M., Khalili, A. & Koza, Z. Tortuosity-porosity relation in porous media flow. *Phys. Rev. E* **78,** 026306 (2008).

196. Duda, A., Koza, Z. & Matyka, M. Hydraulic tortuosity in arbitrary porous media flow. *Phys. Rev. E* **84,** 036319 (2011).

197. Koponen, A., Kataja, M. & Timonen, J. Tortuous flow in porous media. *Phys. Rev. E* **54,** 406–410 (1996).

198. Archie, G. E. The Electrical Resistivity Log as an Aid in Determining Some Reservoir Characteristics. *Transactions of the AIME* **146,** 54–62 (1942).

199. Ho, F.-g. & Striender, W. A variational calculation of the effective surface diffusion coefficient and tortuosity. *Chem. Eng. Sci.* **36,** 253–258 (1981).

200. Tsai, D. S. & Strieder, W. Effective conductivities of random fiber beds. *Chem. Eng. Commun.* **40,** 207–218 (1986).

201. Gebart, B. Permeability of Unidirectional Reinforcements for RTM. *J. Compos. Mater.* **26,** 1100–1133 (1992).

202. Clague, D. S., Kandhai, B. D., Zhang, R. & Sloot, P. M. A. Hydraulic permeability of (un)bounded fibrous media using the lattice Boltzmann method. *Phys. Rev. E* **61,** 616–625 (2000).

203. Ghanbarian, B., Hunt, A., P. Ewing, R. & Sahimi, M. Tortuosity in Porous Media: A Critical Review. *Soil Sci. Soc. Am. J.* **77,** 1461 (2013).

204. Adler, P. Fractal porous media III: Transversal Stokes flow through random and Sierpinski carpets. *Transp. Porous Media* **3,** 185–198 (1988).

205. Happel, J. & Brenner, H. *Low Reynolds number hydrodynamics: with special applications to particulate media* (Springer, 2012).

206. Tomadakis, M. M. & Robertson, T. J. Viscous Permeability of Random Fiber Structures: Comparison of Electrical and Diffusional Estimates with Experimental and Analytical Results. *J. Compos. Mater.* **39,** 163–188 (2005).

207. Vallabh, R., Banks-Lee, P. & Seyam, A.-F. New Approach for Determining Tortuosity in Fibrous Porous Media. *Journal of Engineered Fabrics & Fibers (JEFF)* **5,** 7–15 (2010).

208. Sousa, A. C. M. & Nabovati, A. *LBM mesoscale modelling of porous media* in *Advanced Computational Methods in Heat Transfer X* **I** (WIT Press, Maribor, Slovenia, 2008), 59–68.

209. Carroll, B. J. Equilibrium conformations of liquid drops on thin cylinders under forces of capillarity. A theory for the roll-up process. *Langmuir* **2,** 248–250 (1986).

210. Brakke, K. A. The surface evolver. *Exp. Math.* **1,** 141–165 (1992).

211. McHale, G., Käb, N., Newton, M. & Rowan, S. M. Wetting of a high-energy fiber surface. *J. Colloid Interface Sci.* **186,** 453–461 (1997).

212. Chou, T.-H., Hong, S.-J., Liang, Y.-E., Tsao, H.-K. & Sheng, Y.-J. Equilibrium Phase Diagram of Drop-on-Fiber: Coexistent States and Gravity Effect. *Langmuir* **27,** 3685–3692 (2011).

213. Wang, F. & Schiller, U. D. Hysteresis in spreading and retraction of liquid droplets on parallel fiber rails. *Soft Matter* (2021).

214. `https://dx.doi.org/10.24433/CO.4630860.v2`.

215. Perlin, K. An image synthesizer. *ACM Siggraph Computer Graphics* **19,** 287–296 (1985).

216. Sullivan, C & Kaszynski, A. PyVista: 3D plotting and mesh analysis through a streamlined interface for the Visualization Toolkit (VTK). *Journal of Open Source Software* **4,** 1450 (2019).

Appendix A

Supporting Information for Chapter 4

This appendix describes the statistical analysis of pore network properties. To investigate the role of random disorder in fibrous porous media, we characterize the morphology of nonwoven fiber membranes in terms of the statistical distribution of pore and throat sizes and their connectivity.

To ensure that the generated geometries are large enough to represent the properties of macroscopic random porous media, it is important to determine the size of the representative volume element (RVE) from the selected geometrical and physical properties. In previous work, Huang et al. [54] and Brun et al. [184] have determined the RVE size by setting a threshold of 5% on the relative standard deviation of the local porosity and specific surface area of fixed-size samples. Here we randomly choose 27 sub-samples with identical porosity and fiber diameter to calculate the standard deviation of the pore diameter D_p, throat diameter D_t, throat length L_t, and coordination number n_c. As seen in Table A.1, there is a small difference in the mean pore and throat sizes for the different sample sizes $L = 200a$ and $L = 400a$. The standard deviation of the mean values between samples is around 5% for the smaller samples and decreases to about 2% for the larger samples. In view of the cubic increase of computational demands with system size, we assume that an RVE of $L = 200a$ is sufficient to reduce the impact of system size on the pore space properties. This is also supported by the histograms of the pore and throat size distribution shown

Table A.1: Statistical properties of pore networks extracted from random fibrous media using the SNOW algorithm. The table lists the mean number of pores $\langle N_p \rangle$, throats $\langle N_t \rangle$, connectivity $\langle n_c \rangle$, mean pore diameter $\langle D_p \rangle$, throat diameter $\langle D_t \rangle$ and throat length $\langle L_t \rangle$, along with the respective standard deviation. Each column shows mean values and standard deviation over 27 randomly generated samples. Based on the standard deviation, a domain size of $(200\,a)^3$ is considered sufficient as a representative volume element.

	$\phi = 0.60$		$\phi = 0.70$		$\phi = 0.80$	
	$L = 200a$	$L = 400a$	$L = 200a$	$L = 400a$	$L = 200a$	$L = 400a$
$\langle N_p \rangle$	138.52	874.85	98.30	595.30	60.52	346.15
$\langle N_t \rangle$	355.30	2,652.07	271.52	1,999.85	175.44	1,262.81
$\langle n_c \rangle$	5.15	6.07	5.54	6.72	5.81	7.30
Throat-to-Pore ratio $\langle N_t / N_p \rangle$	2.56	3.03	2.76	3.36	2.88	3.64
$\langle D_p \rangle / a$	16.12	17.64	18.53	20.99	23.28	25.70
$\langle D_t \rangle / a$	15.34	15.22	19.15	19.20	25.77	25.93
$\langle L_t \rangle / a$	31.86	33.46	36.64	39.23	44.18	49.52
Standard deviation of $\langle n_c \rangle$ [%]	4.02	1.41	3.67	1.82	5.33	3.21
Standard deviation of $\langle D_p \rangle$ [%]	5.02	2.49	4.96	2.27	4.10	3.16
Standard deviation of $\langle D_t \rangle$ [%]	4.55	1.79	4.87	2.81	4.68	2.90
Standard deviation of $\langle L_t \rangle$ [%]	5.67	1.75	4.74	2.18	6.05	2.81

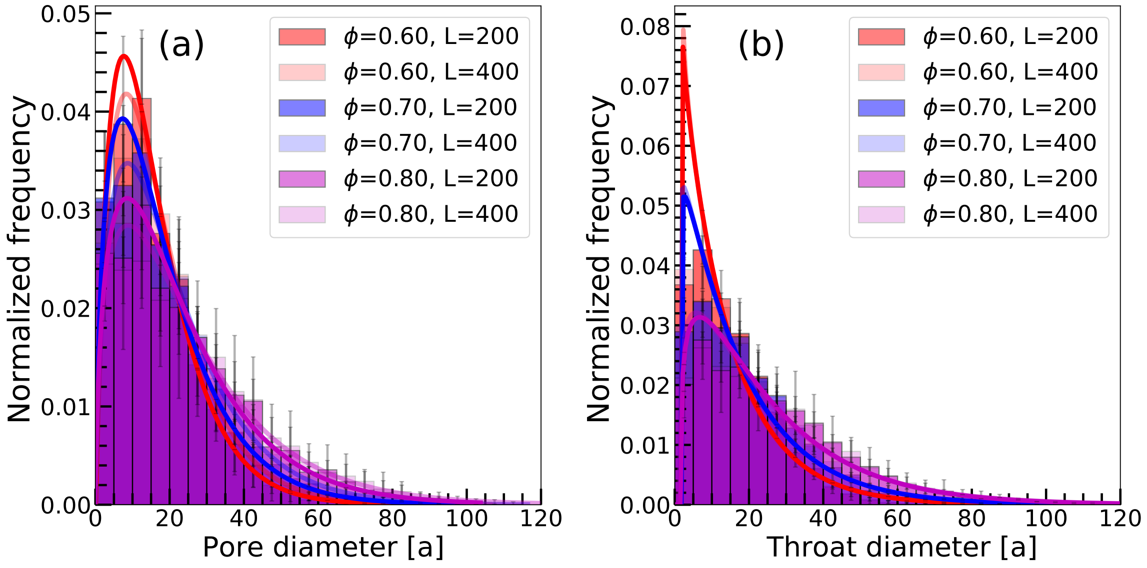

Figure A.1: Pore size distribution (a) and throat size distribution (b) obtained from the pore networks of random fibrous media with porosity 0.60, 0.70 and 0.80. Solid lines represent a gamma distribution fitted to the histograms. The distribution shows a similar shape for system sizes of 200 a and 400 a.

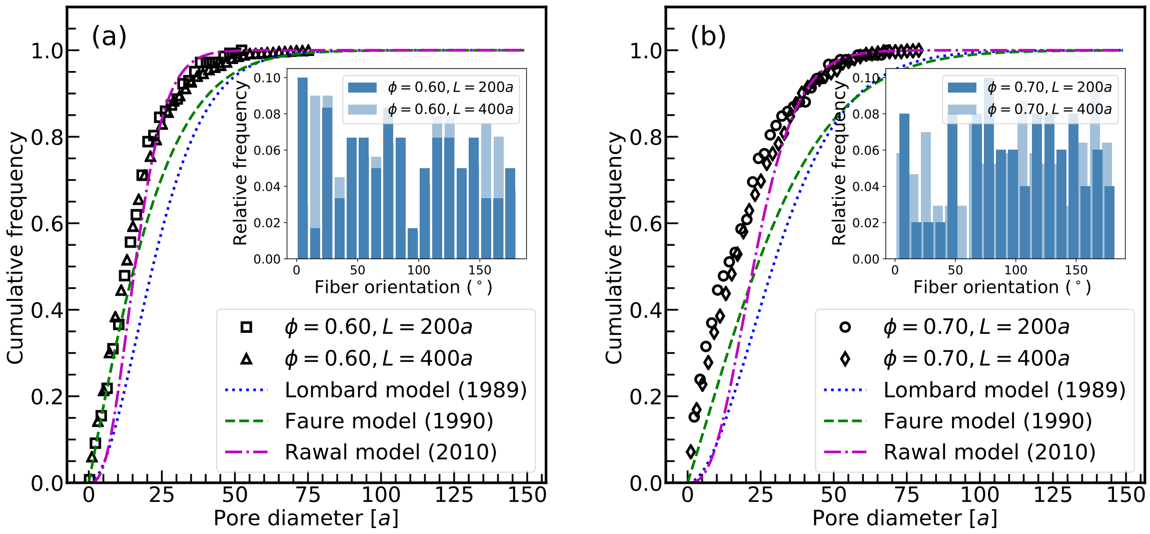

Figure A.2: Cumulative pore size distribution in random fibrous media with porosity ϕ = 0.60 (a) and ϕ = 0.70 (b). The cumulative distribution shows good agreement with theoretical predictions provided the nonuniform distribution of fiber angles (shown in the insets) is taken into account.

in Fig. A.1, where the system size shows little effect on the measured size distribution.

The statistical properties of the pore-networks extracted using the SNOW algorithm for the randomly generated fibrous membranes are given in Table A.1. Each column shows the mean values over 27 different samples and the standard deviation between samples. The pore-networks comprise about three times as many throats as they have pores, with a slight increase of the ratio towards higher porosity along with a higher coordination number. In the SNOW algorithm, throats are found by identifying overlapping regions after dilating neighboring pores. The similar values of pore and throat diameters indicate that the local thickness of the pore size does not vary considerably and there are no significant constrictions between pores. Indeed, the throat length calculated as the mean distance between pore centers is approximately twice the mean pore diameter. This suggests that in the fibrous porous media considered here, most pores are directly connected to each other and the distinction between pores and throats is less pronounced compared to other types of porous media.

The histograms and the fitted gamma distribution in Fig. A.1 show that increasing the porosity leads to a broadened distribution of pore and throat sizes. While the most probable pore size does not vary much, the increased porosity has an effect on the heterogeneity of the pore space and leads to a larger mean pore size. The gamma distribution fits the pore size distribution well but overpredicts the frequency of small throats, which is another indication of the absence of significant restrictions between pores.

Fig. A.2 shows the cumulative distribution of pore sizes for selected porosity and sample size. The histograms of the fiber orientation angles are shown in the insets. Comparison with the theoretical curves calculated from Eq. (2.1) and Eq. (2.2), respectively, show that the Faure and Lombard model predict a slower increase of the cumulative distribution, which indicates that in the samples generated by GeoDict, the frequency of smaller pores is higher than predicted by the models. This can be explained by the non-uniform distribution of fiber orientation angles. According to Rawal's model, the specific length increases with the fiber orientation parameter K_j. Using Eq. (2.3), we obtain a more accurate prediction of the increase of the cumulative frequency of pore sizes. At higher porosities, however, the model still underpredicts the frequency of small pores in the generated samples which may affect predictions of macroscopic properties that are sensitive to the actual pore size distribution in fibrous porous media.